NiN_2S_2 METALLODITHIOLATO LIGANDS IN BIOINSPIRED PROTON REDUCTION CATALYSTS: SYNTHETIC AND KINETIC STUDIES

A Dissertation

by

KAVINDU DILSHAN KARIYAWASAM PATHIRANA

Submitted to the Graduate and Professional School of
Texas A&M University
in partial fulfillment of the requirements for the degree of

DOCTOR OF PHILOSOPHY

Chair of Committee,	Marcetta Y. Darensbourg
Committee Members,	James Batteas
	Sarbajit Banerjee
	Perla B. Balbuena
Head of Department,	Simon W. North

August 2021

Major Subject: Chemistry

ABSTRACT

Hydrogenases are a diverse group of metalloenzymes widespread in nature; they occur in archaea, bacteria and some eukarya and can be classified according to the metal ion composition of the active site in [NiFe], [FeFe] and [Fe] hydrogenases. Hydrogenase (H_2ase) enzymes catalyze one of the simplest molecular reactions, the conversion of dihydrogen into protons and electrons and the reverse reaction, the generation of dihydrogen. The cleavage of dihydrogen occurs at the metal active site that has the capability to increase the acidity of the H_2 molecule and include heterolytic splitting. This process is strongly accelerated by the presence of a nearby base. In these cases, the generation of dihydrogen involves the coupling of a proton and a hydride; the heterolytic nature of this process has been proven by H/D isotope exchange experiments. The [NiFe]- and [FeFe]-H_2ase active sites are composed of sulfur-bridged bimetallic centers. The iron atoms are ligated by small inorganic ligands such as CO and CN^- and an open coordination site exists on one metal center.

Over the past two decades DuBois and co-workers, have made several functional mimics of H_2ase active sites that are mononuclear using abundant and inexpensive first row transition metals such as nickel, iron and cobalt. These mononuclear complexes use diphosphine ligands and emphasize the role of the first and second coordination spheres about the metal. The design criteria for catalysts that are able to produce and oxidize dihydrogen are based on properties of H_2ase enzymes. These properties include the presence of an open coordination site at the metal center, placement of a base in close proximity to the metal center, and the proton acceptor capability of the base to avoid high energy intermediates that can be generated in the catalytic process. These properties also maintain the reversibility of the catalyst.

The efforts highlighted in this dissertation have been prominent in development of catalytic systems that engage NiN_2S_2 as a synthon for the H_2ase active site mimics. The versatility of the metallodithiolates ligands, as surrogates of conventional phosphines and carbenes, was shown in their monodentate binding capabilities with $[Fe^{I}Fe^{I}]$, $[Fe^{I}[Fe(NO)]^{II}]$ and $[(\mu\text{-}H)Fe^{II}Fe^{II}]$ systems, as [FeFe]-H_2ase bioinspired trimetallics. Furthermore, kinetic studies have been conducted to understand the nature of the Fe-S bond strength and the possible ligand substitution mechanism fundamental to catalyst development. The final chapter mainly focuses on the NO ligand exchange phenomena in hemi-labile bridging thiolates that are capable of hydrogen production. Preliminary studies in [NiFe]-H_2ase biomimetics that contain $Fe(NO)N_2S_2$ ligand have demonstrated the possibility of a potential NO scrambling scheme. Kinetic studies are focused on inter/intra-molecular NO scrambling processes.

DEDICATION

To my parents and my brother, whose unconditional love, support and countless sacrifices helped me every step of the way.

ACKNOWLEDGEMENTS

It's an honor and privilege to work under the supervision of one of the pioneers in the field of bioinorganic and organometallic chemistry, Dr. Marcetta Y. Darensbourg, an accomplished scientist, a great advisor, and an exceptional mentor for more than fifty graduate students over the years. I greatly admire your hard work and dedication towards research to unravel the mysteries of nature and I sincerely thank you for being my guide to grow as a research scientist. I would like to thank my committee members, Dr. James Batteas, Dr. Sarbajit Banerjee and Dr. Perla Balbuena for serving on my committee and giving me valuable advices. I would also like to thank Dr. Donald Darensbourg, the kinetics studies presented in this dissertation would not have been possible without your valuable guidance.

Graduate school is a tough and demanding place and it is not easy to be successful without the help and support from your friends and colleagues. I would like to thank Dr. Pokhraj Ghosh for training me when I joined the Darensbourg labs, your friendship precious and I am greatful to have you as a mentor. Also, thank you Manuel Quiroz for helping me with my research and Chase Pectol for always helping me to find and understand literature and all the MYD group members for supporting me in countless different ways. Texas A&M chemistry department is an amazing place with lots of cutting-edge facilities to conduct high quality research. I would like to thank all the facility managers, especially Dr. Yohannes Rezenom at TAMU mass spectrometry facility, Dr. Gregory Wylie and Dr. Douglas Elliott at TAMU NMR facility and Dr. Nattamai Bhuvanesh at TAMU X-Ray facility for helping

me at various stages of my research. I would also like to thank Abbey Kunkle and Sandra Horton for assisting me in various official and administrative work.

As an undergraduate student at University of Colombo, I had the privilege to work with Dr. Dhammike P. Dissanayake who taught me the advanced concepts of chemical kinetics which was invaluable for my graduate research, thank you for being a great teacher to me and inspiring me to join the graduate school at Texas A&M university. Nalanda college, the place where I learned to dream big, the place where I got the inspiration to go into STEM field, I strongly believe that one the reasons I'm here today is because of my wonderful school and I will forever identify myself a proud Nalandian. All my teachers at Nalanda college, especially Mrs. Subashinie Rathnayake, thank you for giving me the basic knowledge in chemistry, physics and biology, it would have been impossible to get a graduate degree without your help and guidance.

Life outside of school has been exciting thanks to my wonderful friends, and I am thankful to all of them for their support, fun times and the memories. I have been truly blessed to be a part of a loving and supportive family. My grandmother, thank you for taking care of me since the day I was born and for being my emotional support. My parents, the two most loving and inspiring people that I have ever met in my entire life, nothing would have been possible if I didn't have you two in my life. Last but not least, my brother Tharindu, words cannot express how thankful I am for your love and support, thank you so much for being my best friend.

NOMENCLATURE

H_2ase	Hydrogenase
DNIC	Dinitrosyl iron complex
NHC	N-heterocyclic carbene
IMes	1,3-Dimesitylimidazole-2-ylidene
Ime	1,3-Dimethylimidazole-2-ylidene
pdt	1,3-Propanedithiolate
adt	2-Aza-1,3-propanedithiolate
bme-dach	bis(N,N'-2-mercapto-2-methylpropyl)-1,5-diazocycloheptane
BArF	Tetrakis(3,5-bis(trifluoromethyl)phenyl)borate
Fc	Ferrocene
Fc^+	Ferrocenium
Cp	Cyclopentadienyl
Cp*	Pentamethylcyclopentadienyl
HER	Hydrogen evolution reaction
TOF	Turnover frequency
TON	Turnover number
CV	Cyclic voltammetry
IR	Infrared spectroscopy
NMR	Nuclear magnetic resonance
EPR	Electron paramagnetic resonance
ESI-MS	Electrospray ionization mass spectroscopy

XRD	X-ray diffraction
GC	Gas chromatography
TFA	Trifluoroacetic acid
DCM	Dichloromethane
THF	Tetrahydrofuran
MeCN	Acetonitrile
SI	Supporting information

CONTRIBUTORS AND FUNDING SOURCES

Contributors

This work was supervised by a dissertation committee consisting of Dr. Marcetta Y. Darensbourg (Advisor), Dr. James Batteas, Dr. Sarbajit Banerjee of the Department of Chemistry and Dr. Perla B. Balbuena of the Department of Chemical Engineering. The experimental work in this dissertation was completed by the student, in collaboration with Dr. Pokhraj Ghosh, Dr. Nattamai Bhuvanesh and Manuel Quiroz.

Funding sources

This work was financially supported by the National Science Foundation (CHE-1665258) and the Robert A. Welch Foundation (A-0924 to Marcetta.Y.Darensbourg and A-0923 to Donald J.Darensbourg)

TABLE OF CONTENTS

Page

LIST OF FIGURES

LIST OF TABLES

CHAPTER I

INTRODUCTION AND LITERATURE REVIEW

Introduction

In 1930, Marjory Jane Stephenson and her coworker L. H. Stickland have discovered that microbes that lives on sugar-beets did not produce alcohols unlike yeasts but produces gaseous products like hydrogen, carbon dioxide and methane.[2] Stephenson and Stickland were also able to demonstrate that in a Thunberg tube, in the presence of hydrogen, these microbes are capable of chemically reducing methylene blue.[3-4] Such observations have led to the conclusion that these microbes contain an enzyme so-called 'Hydrogenase' which is capable of activating hydrogen that initiated a 90 years old and ongoing quest to study, understand and synthesize different types of hydrogenase active sites that contain different bimetallic cores and different catalytic mechanisms.[5]

In 1934, Green and Stickland demonstrated the reversibility of hydrogenase.[3] They made the important discovery that the equilibrium point of the reduction of methyl viologen under the influence of hydrogen is same in both colloidal palladium and in a microbe sample that contains hydrogenase active sites. The first example of the hydrogenase enzyme active site of *Proteus vulgaris* in a cell-free environment was demonstrated by Rittenberg in 1953.[6] In 1960, the isolation and purification of *Desulfovibrio desulfuricans* paved the way to isolating the active site of the [FeFe]-H_2ase four decades later.[7] Seminal work by Haschke and Campbell in 1970's with isolated *Desulfovibrio vulgaris* identified the presence of Fe^{II} in the enzyme active site and an enzyme molecular weight of 41000.[8]

The new era of hydrogenase began with the involvement of organometallic chemists to synthetically manufacture hydrogenase active sites.[9-12] The first reported efforts of synthesizing bio-inspired model complexes of Fe-S clusters by Richard Holm in 1970's has inspired a generation of inorganic chemists to explore novel synthetic pathways to create active site mimics of [FeFe] and [NiFe]-H_2ase.[13-15]

In 1980's Albracht, Graf and Thauer were able to demonstrate the presence of Ni in some hydrogenase active sites via a series of EPR studies.[16-17] These observations were further confirmed by the work of H. J. Kruger, J. J. Moura and G. Unden and reported in seminal papers like "The presence of redox-sensitive nickel in the periplasmic hydrogenase from *Desulfovibrio gigas*".[18]

After six decades later of the initial discovery of hydrogenase by Stephenson and Stickland, in 1995, Fontecilla-Camps were able to deduce the structure of the [NiFe]-H_2ase active site in Desulfovibrio gigas by a series of X-ray crystallographic studies.[19-20] These studies confirmed the IR stretching frequencies reported by Bagley, Albracht and Woodruff in 1994 to be the result of two CN's and two CO's.[21] The crystal structure of [FeFe]H_2ase from *Clostridium pasteurianum* was reported by Peters and Seefeldt in 1998 (Figure I-1).[22] This showed that the active site of [FeFe]-H_2ase contains a bridging ditholate and set of COs, CN^- ligands.

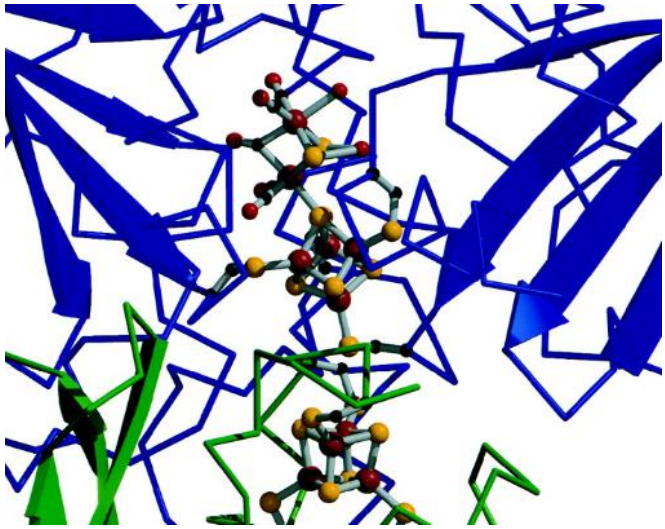

Figure I-1. The first reported structure of the H-cluster of *Clostridium pasteurianum* by Peters and Seefeldt in 1998.[22] The locations of the β sheetsof each lobe of the active site domain is also shown within the polypeptide environment. (Reprinted with permission from (Peters, J. W.; Lanzilotta, W. N.; Lemon, B. J.; Seefeldt, L. C., *Science* **1998**, 282 (5395), 1853-1858). Copyright **1998** The American Association for the Advancement of Science)

The organometallic similarity of the [FeFe]-H_2ase active site was demonstrated by Marcetta and Donald Darensbourg by comparing the small organometallic complex [η^5 -$(C_5H_5)Fe(CN)_2CO]^-$ to the reported values of CO and CN^- stretching frequencies in active sites.[10] These observations have inspired the development of hundreds of organometallic small molecular mimics of the hydrogenase active sites over the past two decades. To this date, over a 1900 research articles have been published by groups worldwide that explore the frontiers in organometallic synthesis and functionality of the active sites of [FeFe] and [NiFe]-H_2ase.[5]

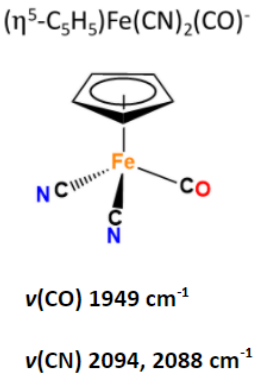

Figure I-2. Structure of $[\eta^5\text{-}(C_5H_5)Fe(CN)_2CO]^-$ and its FTIR *ν*(CO) and *ν*(CN) stretching frequencies.

The chemistry of hydrogen

The simple unimolecular hydrogen plays an extremely important role in both biology and in chemistry. One interesting example is the mid-Indian ocean hydrothermal vents that contains entire ecosystem that uses non-photosynthetic carbon sources that are capable of producing hydrogen using hydrogenase-containing microbes as the energy source.[23-24] For decades, industry is focusing on developing homogeneous/heterogeneous proton reduction and hydrogen oxidation catalysts that are based on heavier noble metals such as platinum, rhodium, palladium and iridium. These metals are capable of performing chemistry that involves two-electron redox state changes.

While [FeFe]-H_2ase is designed specifically for the reduction of protons, [NiFe]-H_2ase is uniquely suitable for the uptake of hydrogen. In industry, reduction of protons is mainly achieved by noble metal catalysts such as platinum in electrolyzers to generate hydrogen to be used in fuel cells as an energy source. In contrast, the extraction of electrons from hydrogen can be seen in many inorganic processes such as reduction of sulfate to hydrogen sulfide or iron(III) to iron(II). Since the active site of the [FeFe]-H_2ase is uniquely

capable of generating hydrogen in aqueous solutions, designing synthetic model complexes to mimic this active site is an ongoing challenge in organometallic chemistry. Furthermore, such systems based on cheap first row transition metals can be a cost-effective alternative for the platinum-based catalysts that we use in both electrolyzers and fuel cells today.

The equations listed below (Equations I-1, I-2, I-3, I-4 and I-5) highlights some of the simple but significant facilitated by hydrogenase in nature. Equations I-1 and I-2 demonstrates the use of hydrogen as an electron source, specifically in biological conditions to manage excess reducing equivalents. Equations I-3 and I- describes the important H/D exchange mechanism while the cleavage or formation of hydrogen. Equation I-5 provides an example of a rhodium(I) based Wilkinson's catalyst, a synthetic organometallic compound that is capable of reducing organic substrates such as olefins.[25]

$$H_2 \rightleftharpoons 2H^+ + 2e^- \quad (1)$$

$$H_2 \rightleftharpoons H^+ + H^- \quad (2)$$

$$H_2 + D_2O \longrightarrow HD + DHO \quad (3)$$

$$H_2 + D_2O \longrightarrow D_2 + H_2O \quad (4)$$

$$Rh^{1+} + H_2 + Sub^{ox} \longrightarrow (Sub)Rh^{3+}(H)_2$$

$$(Sub)Rh^{3+}(H)_2 \longrightarrow Rh^{1+} + H_2Sub^{red} \quad (5)$$

The active site of [FeFe]-H_2ase

The active site of [FeFe]-H_2ase is collectively known as the H cluster is composed with a diiron core that has five CO/CN^- diatomic ligands.[26-28] The diiron core is bridged by an aza-dithiolate type ligand ($S\text{-}CH_2\text{-}NH\text{-}CH_2\text{-}S$).[5] Chemists have isolated the diiron core in a mixed valent $Fe^{I}Fe^{II}$ oxidation state and each iron contains a diatomic CO and a CN^- ligand and one CO between both irons in a semi-bridge position.[29-35] The 2[Fe] subunit is bound to a Fe_4S_4 cluster via a cysteine sulfur that plays a significant role in shuttling electrons necessary for hydrogen production.[36] Based on the proximity to the Fe_4S_4 cluster, the two irons in the 2[Fe] subunit can be divided as proximal and distal Fe and the distal Fe adopts a 'rotated' square pyramidal geometry (Figure I-3).

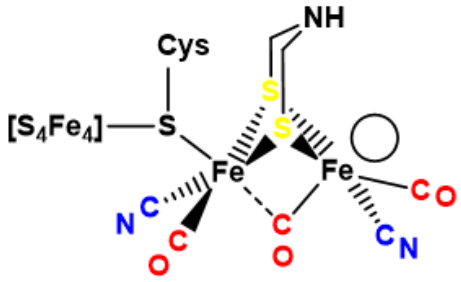

Figure I-3. The H-cluster of the [FeFe]-H_2ase active site Open site on the distal iron is depicted with a circle.

The rotated structure plays a critical role in the activity of the [FeFe]-H_2ase active site by creating an open site on the distal Fe.[37] With the assistance of bridging pendant base, the open site on distal Fe is capable of efficient H^+ reduction and H_2 oxidation in catalytic environments. The surrounding protein matrix of [FeFe]-H_2ase active site is also well equipped to provide a favorable environment to hydrogen production and oxidation.[5] Several

additional FeS clusters can be seen adjacent to the attached Fe_4S_4 cluster to promote efficient electron transfer to the working 2[Fe] subunit.[38-39] Additionally, several hydrophobic tunnels can also be seen that directs hydrogen to and away from the working 2[Fe] subunit.[40-42] All these features play an important task in the activity of the [FeFe]-H_2ase active site, making them a nature's solution to potential hydrogen-based energy economies.

The function of the aza-dithiolate pendant base that bridge the diiron core has been a point of debate since the publishing of its first crystallographic structure by Peters and coworkers.[22, 43] Due to the low crystallographic resolution in early published structures, it was unclear whether the central atom is a N, C or O. However, it is now established that the central atom in the dithiolate bridge is a nitrogen and believed to be playing a crucial role in shuttling protons to the open site of distal Fe site to generate a terminal iron-hydride. It has been theorized that the one of the reasons for the extraordinary turnover rates in [FeFe]-H_2ase is possibly due to this well positioned pendant base.[44-47] One example that highlights the importance of a well-positioned pendant base comes from the square plane DuBois catalysts that can achieves turnovers over 100,000 s^{-1}.[48-51] The importance of the pendent base has also been highlighted in a [FeFe]-H_2ase active site mimic (μ-$SCH_2N(H)CH_2S$)$[Fe(CO)(dppv)]_2$, (dppv = diphenylphosphino ethylene), where diphosphine ligands creates rotated Fe environment with an open site with a bridging CO ligand. Comparison studies have demonstrated that when a pendant base feature is present, the electrocatalytic proton reduction is much significant compared to (μ-pdt)$[Fe(CO)(dppv)]_2$ analogue that does not contain a pendant base unit.[32]

Catalytic mechanism of [FeFe]-H_2ase

The catalytic mechanism of [FeFe]-H_2ase has been a point of debate over the last two decades.[33, 43, 52-61] The widely accepted catalytic mechanism for hydrogen evolution from [FeFe]-H_2ase describes a mixed valent $Fe^{I}Fe^{II}$ state as the starting point with a fully oxidized $[Fe_4S_4]^{2+}$ cluster (H_{ox}).[33] Then a proton coupled electron reduce the diiron core to $Fe^{I}Fe^{I}$ and positioned a proton in the bridgehead amine (H_{red}). Recent FTIR studies by Berggren and coworkers on HydA1 have identified a stable reduced state which is one electron reduced from H_{red} where an electron moves to the $[Fe_4S_4]^{2+}$, thereby generating a super reduced $Fe^{I}Fe^{I}$-$[Fe_4S_4]^{1+}$ intermediate state (H_{sred}).[62] The next step of the catalytic cycle is the formation of a terminal hydride and the reoxidation of the $[Fe_4S_4]$ cluster. DFT and experimental studies have indicated that the formation of a bridging hydride is more thermodynamically stable compared to a terminal hydride.[62] However, the formation of a bridging hydride will decrease the hydrides potential to combine with a bridgehead proton to generate hydrogen compared to a terminal hydride.

In the final step, the terminal hydride is combined with a bridgehead proton to produce hydrogen and regenerates the H_{ox} state that contains a η_2 -H_2 on the distal iron (Fe_d). This η_2 -H_2 has a short lifetime and gets detached from the Fe_d releasing hydrogen and generating a free H_{ox} that is capable of reentering the catalytic cycle (Figure I-4).

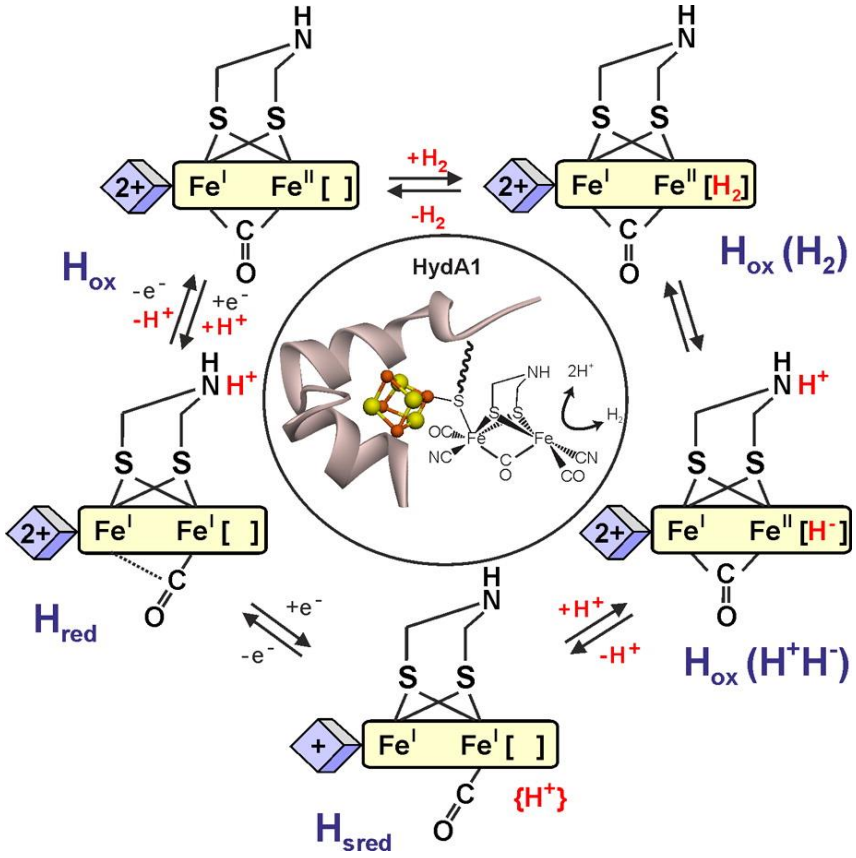

Figure I-4. Proposed catalytic mechanism of [FeFe]-H_2ase with the confirmed H_{ox},H_{red} and H_{sred} intermediate states.[5, 33] (Reprinted with permission from (Lubitz, W.; Ogata, H.; Rüdiger, O.; Reijerse, E., *Chem. Rev.* **2014**, 114 (8), 4081-4148). Copyright **2014** American Chemical Society)

Synthetic mimics of [FeFe]-H_2ase

Plethora of small molecular mimics of [FeFe]-H_2ase have been developed over the last two decades where the works of prominent chemists like Marcetta Y. Darensbourg, Tom Rauchfuss and Chris Pickett have helped to create more faithful, functional biomimetics.[63-67] The first reported biomimetic of [FeFe]-H_2ase, $(\mu\text{-SR})_2(Fe(CO_3)_2)$ by Reihlen in late 1920's contains a simple disulfide bridge and three terminal CO ligands in each iron.[68] Developed from this, the synthetic mimic $(\mu\text{-pdt})(Fe(CO_3)_2)$, pdt = propane dithiolate, has gained a significant attention of synthetic chemists due to its highly stable nature, well defined IR spectroscopic handles provided by its terminal CO ligands and also because of its ability to demonstrate efficient ligand substitution properties via CO/L exchange. One of the most important modifications of simple $(\mu\text{-pdt})(Fe(CO_3)_2)$ was to introduce $(S\text{-}CH_2\text{-}NH\text{-}CH_2\text{-}S)$ to its bridgehead, thereby creating a $(\mu\text{-adt})(Fe(CO_3)_2)$, adt = aza-dithiolate, that contains the important pendant base feature.[69] Nevertheless, studies have shown that due to the lack of an open site, these molecules fail to demonstrate efficient electrocatalytic hydrogen production. Following the development of $(\mu\text{-adt})(Fe(CO_3)_2)$, several groups have attempted to synthesize similar compounds with different bridgehead functional groups.[70-76] Among them, diiron hexacarbonyl units containing oxadithiolate and thiadithiolate bridgehead units are significant and shown in Figure I-5.

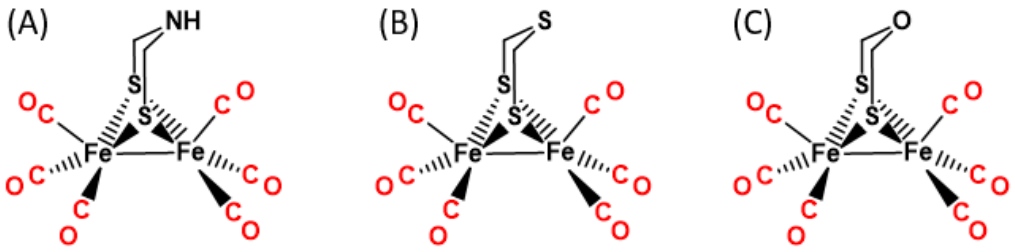

Figure I-5. Depictions of (A) (μ-adt)$[Fe(CO)_3]_2$, adt = azadithiolate; (B) (μ-tdt)$[Fe(CO)_3]_2$, tdt = thiadithiolate (C) (μ-odt)$[Fe(CO)_3]_2$, odt = oxadithiolate.

The two main techniques to synthesize diiron hexacarbonyl is either to react a dithiolate like 1,3-propanedithiolate with triiron dodecacarbony ($Fe_3(CO)_{12}$) or functionalization of bridging persulfide iron carbonyl ((μ-S_2)$[Fe(CO)_3]_2$) synthesized in 1958 by Hieber and Gruber.[77] The remarkable stability and feasible ligand substitution properties of resulting diiron hexacarbonyl compounds has be exploited for decades in order to create efficient electrocatalysts for hydrogen production and the simple ((μ-SRS)$[Fe(CO)_3]_2$ model has become one of the standards for developing applications. Recent developments includes synthesizing complete models of H-cluster that includes redox active ligands, open site and a pendant base, embedding (μ-dcbdt)$[Fe(CO)_3]_2$ dcbdt = dicarboxyl benzenedithiolate, into a Zr(IV) based metal-organic frameworks, immobilizing ((μ-S_2)$[Fe(CO)_3]_2$) units on CdSe quantum dots and embedding diiron hexacabonyl units into polymeric backbones using techniques such as atom transfer radical polymerization (ATRP) (Figure I-6).[78-81]

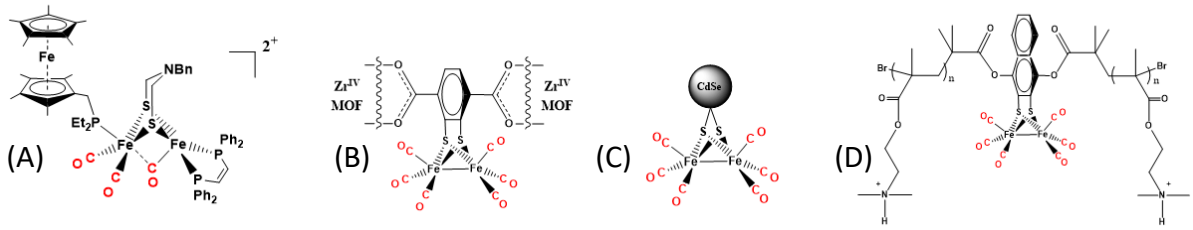

Figure I-6. (A) [FeFe]-H_2ase H cluster mimic that contains a redox active ligand, a pendant base and an open site developed by Rauchfuss et al.[78] (B) [FeFe]-H_2ase active site mimic loaded on to a Zr^{IV} based metal organic framework.[80] (C) [FeFe]-H_2ase active site mimic embedded on to a CdSe quantum dot.[79] (D) [FeFe]-H_2ase mimic installed into a metallopolymer designed by ATRP technique.[81]

The work by Lichtenberger et al. to embed a diiron unit into a polymer backbone can be considered as one of the most significant recent development in synthesizing efficient hydrogen producing catalysts.[81-85] Despite the tremendous progress made over the years to synthesize [FeFe]-H_2ase biomimetics, several important challenges still remain in this area, such as;

1. Increasing the activity and chemical stability of the catalysts.
2. Lowering their overpotential.
3. Using water as the solvent and proton source.
4. Inhibit aggregation while maintaining rapid electron transfer to the active site.
5. Increasing aerobic stability.

By taking a novel metallopolymer approach, Lichtenberger et al. were able to overcome problems such as lower solubility in aqueous solutions and inhibit the aggregation while maintaining efficient electron transfer to the active site. In order to construct the metallopolymer that includes the [FeFe]-H_2ase mimic, a method known as Atom Transfer Radical Polymerization (ATRP), a technique developed by Krzysztof Matyjaszewski at

Carnegie Mellon university was applied.[81] A [FeFe]-H2ase mimic that contains a tertiary bromide was successful as a metalloinitiator to create a tertiary radical using a Cu catalyst. This radical in turn undergoes a living polymerization with methacrylate monomers to give a polymethacrylate polymer extending from both sides of the diiron unit, essentially creating an embedded active site in the polymer backbone (Figure I-7). It has been reported that the resulting metallopolymer has an enhanced catalytic activity for the production of hydrogen near neutral pH values.[81-85] However, one of the major problems in this process is that ATRP is a harsh radical polymerization technique and will not be suitable to use with many existing H2ase mimics that are not stable as the [Fe2S2(CO)6] subunit.

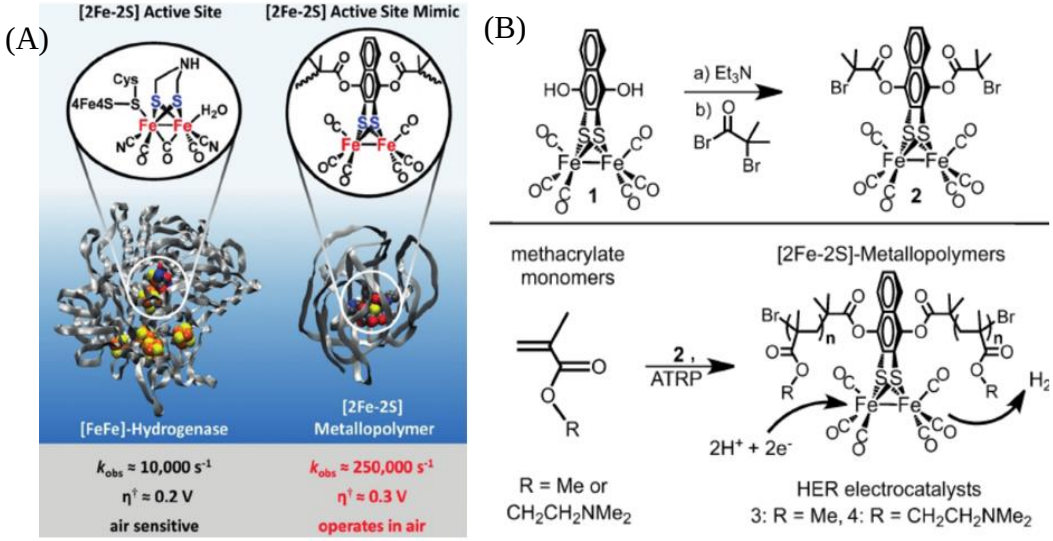

Figure I-7. (A) Comparison of a new class of [2Fe-2S]-metallopolymer HER catalysts vs. [FeFe]-H2ase catalysts at the same scale, where the metallopolymer HER catalyst is remarkably faster than the enzyme and is air stable at neutral pH. In addition, current densities greater than 300 mAcm^2 are achieved with 75 mm catalyst loading. η†is the overpotential requirement to achieve an operating cell current density of 0.1 mAcm^2. (B) Synthetic scheme for the metallopolymer by ATRP that enables facile modulation of catalyst solubility.[81] (Reprinted with permission from (Brezinski, W. P.; Karayilan, M.; Kayla, C. E.; Pavlopoulos, N.G.; Li, S.; Fu, S.; Matyjaszewski, K.; Evans, D. H.; Glass, R. S.; Lichtenberger, D. L., *Angew. Chem. Int. Ed.* **2018**, 57 (37), 11898-11902). Copyright **2018** John Wiley and Sons)

In 2016 Rauchfuss and cowerkers published a comprehensive review on diiron dithiolato carbonyl complexes that highlights the major developments in synthesis of [FeFe]-H_2ase active site mimics.[86] Among the many topics discussed, the review pays special attention to some of the unusual diiron hexacabonyl systems such as macrocyclic bis(diiron) dithiolates, synthesis of asymmetrical diiron dithiolates, peri-naphthalenedithiolatodiiron complexes and unusual diiron hexacarbonyl structures obtained from the reactions between $Fe_3(CO)_{12}$ and CS_2.

Fluxional properties of [FeFe]-H_2ase active site mimics

An important property of thiolate bridged diiron hexacarbonyls is their flexibility at both bridgehead and at $Fe(CO)_3$ centers. Variable temperature ^1H and ^{13}C NMR studies on (μ-pdt)$[Fe(CO)_3]_2$ systems by Darensbourg et. al has demonstrated the inversion motion of the bridgehead as well as the apical/basal CO site exchange at $Fe(CO)_3$ center.[30, 87-88] Furthermore, these studies have concluded that when increasing the size of the substituent on bridgehead can alter the fluxional motion, thereby providing insights about the steric factors. Similarly, the studies on $Fe(CO)_3$ rotor has concluded that the rotation around a single Fe center does not result in CO ligand transfer between two irons.

At room temperature the simple (μ-pdt)$[Fe(CO)_3]_2$ system is in constant motion. The bridging -$SCH_2CH_2CH_2S$- part swings back and forth giving a mixture of boat/chair conformers and the $Fe(CO)_3$ rotor undergoes rapid apical/basal CO site exchange.[30] As a result, the at room temperature you only see a single ^1H peak for the bridgehead and a single ^{13}C peak for the CO ligands. However, when the temperature is decreased to -60C^0, two ^1H NMR peaks corresponding to axial and equatorial H on bridgehead can be observed. At -80C^0 four ^{13}C peaks appears on NMR which distinguished two different $Fe(CO)_3$ sites due

to the freezing of bridgehead as well as apical/basal CO's. When increasing the size of the thiolate linker (e.g. (μ-$SCH_2C_6H_4CH_2$)[$Fe(CO)_3$]$_2$), studies have shown that even at higher temperatures as $75C^0$, the bridgehead remains fixed demonstrating that steric hindrance can attenuate the fluxional properties (Figure I-8).

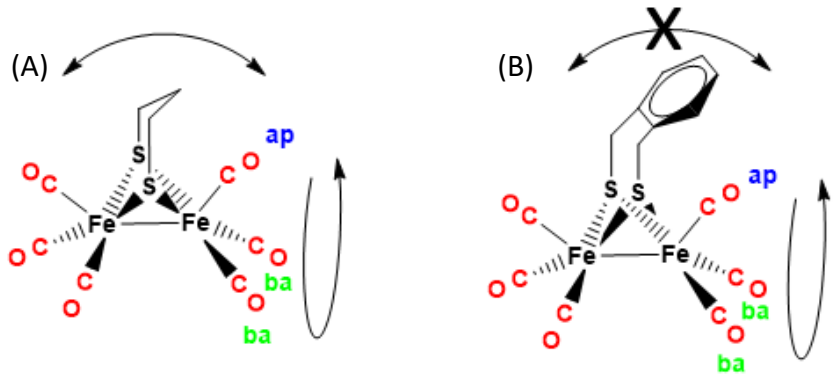

Figure I-8. (A) The simple (μ-pdt)[$Fe(CO)_3$]$_2$ unit that demonstrate fluxional properties in both bridgehead and the $Fe(CO)_3$ rotor where apical/basal CO site exchange occurs. (B) (μ-$SCH_2C_6H_4CH_2$)[$Fe(CO)_3$]$_2$) unit does not demonstrate fluxional properties at bridgehead due to the influence of steric effects.

Hydrogenase active site mimics with hemilabile properties

Evidence from protein crystallography reveals that the active sites of metalloenzymes in nature such as [FeFe]-, [NiFe]-H_2ase and acetyl CoA synthase display polymetallic compositions of at least two first row transition metals bridged by thiolate sulfurs along with Lewis acidic/basic sites.[5] In contrast, many common homogeneous/heterogeneous catalytic systems use precious/resource limited metals such as Pt and other noble metals that can operate as single-site catalysts. Over the past two decades, a plethora of synthetic biomimetics of [NiFe]- and [FeFe]-H_2ase active sites have been studied and analyzed for their potential to serve as efficient catalysts in the Hydrogen

Evolution Reaction (HER). The obvious overarching goal is to construct sustainable H_2-producing small molecule analogues of those abundant metal catalytic sites as catalysts from photovoltaic electrons *via* electrocatalysts.

The structure and function of these natural biocatalytic active sites are well established, as are key features for activity. For example, in [FeFe]-H_2ase, a well-positioned pendant amine base near to the open site is essential in achieving remarkable rates of H_2 production whereas in [NiFe]-H_2ase a terminal cysteinyl thiolate on the Ni appears to serve that purpose. While the understanding of these active sites is now mature, synthetic approaches to highly functional, efficient biomimetics to use in real world applications is still an ongoing challenge to chemists in academia and in industry. Many studies have focused on mimicking the crucial pendant base feature, which facilitates the storage and delivery of protons to the enzyme active site during the final step of catalytic H_2 production. This last step requires to pull out a strong metal bound hydride and the adjacent protonated pendant base serves a kinetic purpose by lowering the final energy barrier. Dubois et al. have outfitted a Ni-based catalyst system with PNP ligands so that a pendant base occupies a nearby site to the Ni center (Figure I-9a.),[51] Wang et al. have demonstrated the ability of terminal thiolates attached to the diiron core to perform H/D exchange reactions (Figure I-9b.)[89], Darensbourg et al. have demonstrated the ability to attach a NiN_2S_2 metallodithiolate ligand to a diiron core in monodentate fashion so it contains an unbound thiolate closer to the metal center to potentially serve as a pendant base(Figure I-9c.).[90] In all these complexes a distinct external pendant base site can be identified in close proximity to the active metal center so it can achieve the task of proton storage/delivery as necessary.

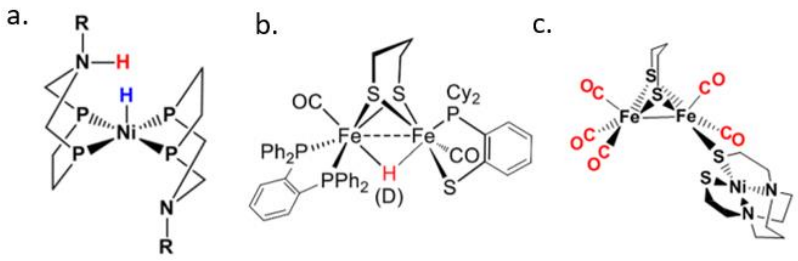

Figure I-9. Synthetic H_2 producing catalytic systems by a.) Dubois et al.[51] b.) Wang et al.[89] and c.) Darensbourg et al.[90] that contains pendant base features.

Due to the metallodithiolate-as-synthon approach inspired by the acetyl CoA synthase active site[91], an extensive array of bi/poly metallic complexes exists containing MN_2S_2 ligands which demonstrates a close structural resemblance to the active site of [NiFe]-H_2ase with a butterfly type core.[92] The metallodithiolate ligand mostly contains a Ni^{II}, Fe(NO), or Co(NO) metal center in a tetradentate $E_2S_2^{2-}$ (E = N, P, S) binding pocket where the cis thiolate sulfurs contain lone pairs to form dative bonds to an external metal center M', usually in a bidentate manner (Figure I-9). Myriad examples exist that use η^5-cyclopentadienide (**η^5-C_5H_5** or η^5-C_5Me_5, i.e., Cp and Cp* respectively) or η^6-arenes bound to d^6 Fe^{II} or Ru^{II} as M' in combination with metallodithiolate ligands to generate sulfur-bridged bimetallic species (Figure I-10). A functional model complex ($[Ni^{II}(X')Fe^{II}(MeCN)\{P(OEt)_3\}_3](BPh_4)_2$ designed by Ogo et al.[93] to activate molecular hydrogen, is an excellent early example for such complexes. It is capable of heterolytically activating H_2 to form a hydride complex that reduces substrates by either hydride ion or electron transfer. Even though this complex does not demonstrate the hemilabile features, the labile MeCN ligand on the receiver Fe^{II} unit is capable of generating the much-needed open site for the hydride.

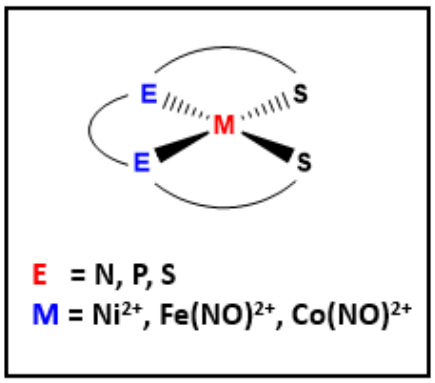

Figure I-10. The ME_2S_2 bidentate ligand. The E-S linkers and E-E linkers are typically $-(CH_2)_n-$ units with n = 2, 3, 4. (M = Ni^{2+}, $Fe(NO)^{2+}$, $Co(NO)^{2+}$; E = N, P, S)

The reported complexes by Darensbourg et al. in their 2017 study "A matrix of heterobimetallic complexes for interrogation of hydrogen evolution reaction electrocatalysts" ([Ni-Fe_{CO}]$^+$, [Fe-Fe_{CO}]$^+$, [Ni-Fe] and [Fe-Fe]$^+$) lack an obvious open site for a hydride at receiver M', as well as an obvious pendant base feature which is proven to be useful in order for such complexes to act as efficient H_2 producing catalysts (Figure I-11).[94] However, it has been observed that the bimetallics using MN_2S_2 (M = Fe(NO), Ni) as a donor and a M' (M' = FeCpCO, FeCp*CO, $Fe(NO)_2$) as an accepter are capable of demonstrating hemi-labile features. Hemilability in such complexes leads to the cleavage of a single S-M' bond in M-**μ**-S_2-M' ring to form the much-needed open site at M' as well as a pendant base temporarily under electrocatalytic environments.[95-97]

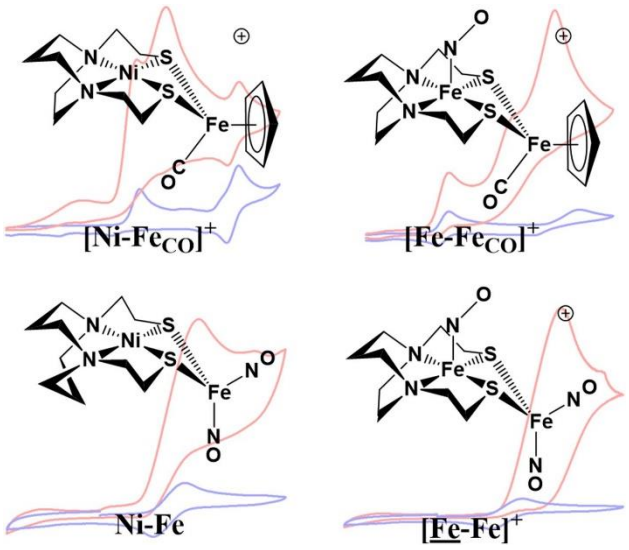

Figure I-11. Structural representations of electrocatalysts for proton reduction: [Ni-Fe$_{CO}$]$^+$, [Fe-Fe$_{CO}$]$^+$ (31), Ni-Fe (38), [Fe-Fe]$^+$. The background of each species shows the cyclic voltammograms (CVs) before (blue) and after (red) the addition of acid.[95] (Reprinted with permission from (Ding, S.; Ghosh, P.; Darensbourg, M. Y., *PNAS* **2017**, 114 (46), E9775-E9782). Copyright **2017** National Academy of Sciences, U.S.A.)

Hemilability is a term originally coined by Rauchfuss for P--O bidentate ligands which are capable of dissociating one arm while maintaining the structural integrity of the complex. Early investigations of Ru bound phosphine-ether bidentate ligands have demonstrated the ability to form stable complexes while allowing the readily dissociation of "hard" ligand part to create vacant sites on the metal center. The six-coordinated complex $RuCl_2(PO)_2$ (P--O = *o*-(diphenylphosphino) anisole) with trans chlorines and cis phosphorus atoms rapidly reacts with CO at room temperature resulting in a fluxional monomeric complex $RuCl_2(PO)_2(CO)$ eventually leading to the *all-trans* $RuCl_2(P\text{--}O)_2(CO)_2$.[98] Nuclear Magnetic Resonance evidence led to the conclusion that the CO monoadduct complex $RuCl_2(P\text{--}O)_2(CO)$ is in a rapid equilibrium with a five-coordinated intermediate state derived from cleavage of the remaining Ru-O bond. This coordinatively unsaturated

complex is expected to be responsible in generating the bis adducts in a kinetically favored trans geometry.

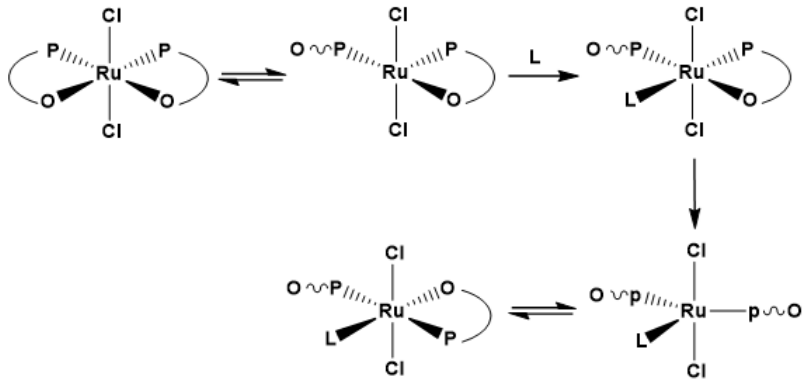

Figure I-12. Hemilabile properties of bidentate PO ligands in Ru complexes.[98] (Adopted with permission from Jeffrey, J. C.; Rauchfuss, T. B., *Inorg. Chem.* **1979** 18, 2658-2666). Copyright **1979** American Chemical Society)

Even though the complex $RuCl_2(P\text{--}O)_2$ is oxygen and heat stable, the two weakly bound ether oxygen atoms make it reactive towards variety of ligands (Figure I-12). Unlikely, the hemilabile properties observed in M'-MN_2S_2 adducts are completely reduction-based phenomena. The electron saturation at the receiver metal center M' leads to the disruption of a single dative S-M' bond in in M-**μ**-S_2-M' core (Figure I-13). Furthermore, this reduction-induced hemilability displayed by aforementioned metallodithiolate complexes can be modulated based on their hard/soft characteristics. By simply changing the metal center of the donor MN_2S_2 unit, the hard/soft nature can be adjusted and together with a hard/soft accepter, an array of $Donor^{hard}$-$Acceptor^{hard}$, $Donor^{soft}$-$Acceptor^{hard}$, $Donor^{hard}$-$Acceptor^{soft}$ and $Donor^{soft}$-$Acceptor^{soft}$ can be constructed with varying hemilabile features.[94-97] Electrochemical studies combined with Computational investigations have led to the elucidation of most probable catalytic pathways explaining the ability of such complexes to generate an open site on acceptor M' metal centers to land electron/proton

leading to hydrides as well as invoking hemilability to temporary generate a pendant bases to land protons.

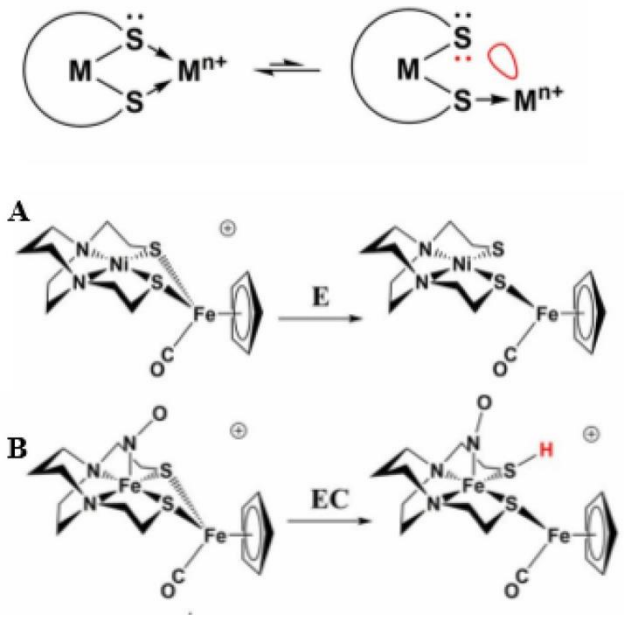

Figure I-13. Hemilability in MN_2S_2 bridging thiolates. (A) Reduction induced hemilability, (B) Reduction followed by protonation to induce hemilability in complexes with soft MN_2S_2 donor units[90] (Reprinted with permission from (Kariyawasam Pathirana, K. D.; Ghosh, P.; Hsieh, C-H.; Elrod, L. C.; Bhuvanesh, N.; Darensbourg, D. J.; Darensbourg, M. Y., *Inorg. Chem*, **2020**, 59 (6), 3753-3763). Copyright **2020** American Chemical Society)

Understanding the (NO)Fe-Fe(NO)$_2$ diiron trinitrosyl unit

Protein crystallographic studies over the last two decades have led to the identification and understanding of the active sites of [NiFe]-H_2ase, acetyl coA synthase (ACS) and CO-dehydrogenase. All these cases demonstrate the harnessing of at least two first row transition metals connected via sulfides or thiolates to conduct their catalytic activity. Darensbourg et al. have conducted extensive studies using ACS active site mimetic MN_2S_2 type metallodithiolato ligands that binds to a receiver metal units such as $Fe(NO)_2$ and η^5-C_5R_5 (R = H, CH_3).[94-96] An example of such a diiron trinitrosyl unit is shown in Figure

I-14. For this system electrochemical studies have found two single electron reversible reductions at -0.78 V and -1.33 V, assigned to $\{Fe(NO)_2\}^{9/10}$ and $\{Fe(NO)\}^{7/8}$ couples respectively. When a strong acid like $HBF_4.Et_2O$ is present, the redox couple at -0.78 V ($\{Fe(NO)_2\}^{9/10}$) has shown a catalytic activity towards production of hydrogen at modest overpotentials. Further computational studies have shown that at -0.78 V a potential hydride bound $\{Fe(NO)_2\}$ intermediate is responsible for facilitating the hydrogen evolution reaction. However, the analysis of more negative $\{Fe(NO)\}^{7/8}$ couple at -1.38 V have demonstrated no catalytic hydrogen evolution and the computational studies have found that the protonation of $\{Fe(NO)\}^{7/8}$ center leads to the termination of catalytic cycle.

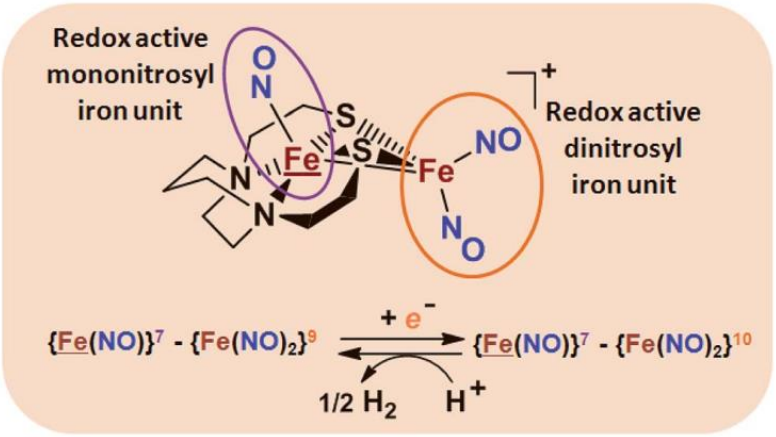

Figure I-14. Structure and redox activity of $[(NO)Fe\text{-}Fe(NO)_2]^+$. Protonation of the one-electron reduced diiron complex yields H_2.[94] (Reprinted with permission from (Ghosh, P.; Ding, S,; Chupik, R. B.; Quiroz, M.; Hsieh, C-H.; Bhuvanesh, N.; Hall, M. B.; Darensbourg, M. Y., *Chem. Sci*., **2017**, 8, 8291-8300). Copyright **2017** Royal Society of Chemistry)

Preliminary studies by Darensbourg et al. on a labeled diiron trinitrosyl complex suggests a possible inter/intra molecular NO ligand mobility within the dinitrosyl and mononitrosyl subunits. Recent studies by Lehnert et al. have shown an interesting dimeric intermediate structure that contains a NO bridged diamond core where two nitrosyls bridge

between two irons indicating possible interactions of NO ligands within adjacent irons.[99] Literature suggests that many {FeNO}^{8} complexes disproportionate by forming dinitrosyl iron complexes (DNICs), however the mechanism of this process is still not fully understood. While studying this process by reducing a {FeNO}^{7} unit [Fe(TPA)(NO)](OTf) (TPA = tris(2-pyridylmethyl)amine, OTf = trifluoromethanesulfonate) Lehnert et al. have discovered an unexpected intermediate without any DNIC or N_2O. This unexpected intermediate has been isolated and shown to have a $Fe_2(NO)_2$ type diamond core ($[Fe_2(TPA)_2(NO)_2]$-$(OTf)_2$) Figure I-15.[99] Such observations raise interesting questions and provides an idea about the potential intermediate structures for the observed inter/intra-molecular NO scrambling reactions.

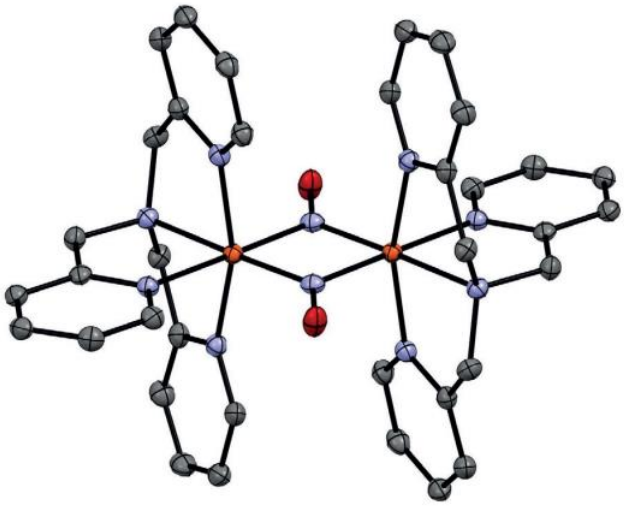

Figure I-15. Crystal structure of ($[Fe_2(TPA)_2(NO)_2]$-$(OTf)_2$) with thermal ellipsoids set at 50% probability. The triflate counter anion, solvent molecules, and hydrogen atoms are omitted for clarity[99] (Reprinted with permission from (Dong, H. T.; Speelman, A. L.; Kozemchak, C. E.; Sil, D.; Lehnert, N., *Angew. Chem. Int. Ed.* **2019**, 58 (49), 17695-17699). Copyright **2019** John Wiley and Sons)

Thus, this dissertation will focus on understanding the essential features of the [FeFe]-H_2ase active site required for catalysis through structural and functional model complexes. Chapter III will mainly focus on synthesizing different [FeFe]-H_2ase biomimetics with different oxidation states and a pendant metallodithiolato ligand that can potentially act as a pendant base mimicking the aza-dithiolate unit in the enzyme active site. X-da crystallography will be used to understand the structural features and the electrochemical studies will be focusing on understanding the redox states as well as the response of the catalyst under the presence of trifluoroacetic acid as the proton source.

Chapter IV will mainly focus on mechanistic studies of the synthesized complexes. Ligand substitution studies will be used to gain a conceptual understanding of the bond strength of the Fe-S bond that exist between the diiron core and the metallodithiolato ligand in all complexes. Variable temperature kinetic studies will be used to deduce bond strengths as well as two different pathways (Associative and Dissociative) for the NiN_2S_2/PMe_3 exchange.

Chapter V will mainly be focused on understanding the (NO) ligand exchange phenomena in diiron trinitrosyl complexes. Temperature dependent kinetic studies will be employed to understand the inter/intra-molecular NO scrambling as well as to deduce the rate constants for scrambling reactions.

Chapter IX, addresses the importance of utilizing synthetic metallodithiolato ligands as potential pendant bases to direct protons towards the active metal site and open questions about the inter/intra-molecular rearrangement processes in diiron trinitrosyl systems.

CHAPTER II

GENERAL EXPERIMENTAL DETAILS FOR CHAPTERS III-V[#]

All synthetic procedures and operations were carried out on a double-manifold Schlenk line under a N_2 atmosphere or in a Ar glovebox with syringe/rubber septa techniques. All solvents (acetonitrile, dichloromethane, benzene, hexane, pentane, toluene, methanol and diethyl ether) were purified using a MBraun manual solvent purification system that uses Alcoa F200 activated alumina desiccant. Hexacarbonyl complexes, (μ-pdt)$[Fe(CO)_3]_2$, (μ-pdt)$[Fe(CO)_3][(Fe(NO))^{II}(IMe)(CO)]^+$ BF_4^-, (μ-pdt)(μ-H)$[Fe^{II}(CO)_2(PMe_3)]_2^+$ PF_6^- and the ligands Ni(bme-dach), (NO)Fe(bme-dach), (^{15}NO)Fe(bme-dach), $Fe(CO)_2(NO)_2$, $Fe(NO)_2(PPh_3)_2$, $[Fe(CO)_3NO]$[18-crown-6] were synthesized according to the literature procedures. Reagents propanedithiol, CF_3COOH, [NO][BF4], $CoCp^*_2$, $CoCp_2$, Fc$[PF_6]$, PMe_3, PPh_3, HPLC-grade acetonitrile CH_3COOH, $(PPh_3)AuCl$, $C_6H_5CH_2Br$, ferrocene, C_2H_5I, KBr, NaBr, KEt_3BH, $[nBu_4N][PF_6]$, $AgBF_4$, were purchased from commercial sources such as Sigma-Aldrich, Alfa-Aesar, Strem, Acros or TCI and used as received. The gases Ar, N_2, CH4, CO, H_2 were purchased from Praxair. Elemental analyses were performed by Atlantic Microlab, inc., Norcross, Georgia, United States. Mass spectrometry (ESI-MS) was performed by the Laboratory for Biological Mass Spectrometry at Texas A&M University. ^{1}H, ^{13}C and ^{31}P NMR spectra were recorded on a superconducting Bruker Avance Neo console with an Ascent magnet and an automated

[#]Parts of this chapter were reproduced with permission from (Kariyawasam Pathirana, K. D.; Ghosh, P.; Hsieh, C-H.; Elrod, L. C.; Bhuvanesh, N.; Darensbourg, D. J.; Darensbourg, M. Y., Synthetic Metallodithiolato Ligands as Pendant Bases in $[Fe^IFe^I]$, $[Fe^I[Fe(NO)]^{II}]$, and $[(\mu\text{-H})Fe^{II}Fe^{II}]$ Complexes. *Inorg. Chem*, **2020**, 59 (6), 3753-3763). Copyright **2020** American Chemical Society)

turning 5mm broadband iProbe with a 60 position SampleXpress sample changer operating at 400 MHz.

Fourier transform IR (FTIR) and UV-Vis measurements

Infrared spectra (IR) were recorded on a Bruker Tensor 37 FTIR spectrometer using a CaF_2 cell with 0.2 mm path lengths. Kinetic parameters were obtained using a reactIR ic10 equipped with a DST series AgX fiber conduit. SiComp sensor was used that has a pH range of 1 to10, temperature range of -80℃ to 180℃ and pressure up to 69 bar. Time resolved UV-Vis measurements were obtained using a Shimadzu UV-2450 UV-Vis double beam spectrometer with a 1cm pathlength.

Kinetic measurements

Pseudo-first-order reaction conditions were employed for determination of the order of the reaction. Reactions were monitored using infrared spectroscopy and UV-Vis. For IR measurements, 2 mL of DCM solution containing 4.7 mmolar diiron complex in a two-neck flask was placed in a Eyela PSL-1400 and VWR polyscience 1162 temperature-controlled bath. Following temperature equilibration, solution of PMe_3 at the same temperature was injected into the two-neck flask. While being magnetically stirred, aliquots for IR spectra were removed and the reaction was monitored through four half-lives. Rates of reactions were measured by following the decrease in absorption of the reactant's most intense non overlapping *ν*(CO) vibration, which centered at ca. 1966 cm^{-1}. The IR data were reproduced using UV-Vis spectroscopy where the reactions were monitored in a cuvette. Three mL of 0.3 mmolar diiron complex in DCM was directly injected with the PMe_3 solution and the decrease of peak at 393 nm which corresponds to the starting material was monitored. Rate constants were calculated from plots of $\ln(A_0/A_t)$ versus time typically using >30 data points

over 4 to 5 half-lives giving correlation constant of 0.99. Reproducibility of a run under identical conditions was 95% or better. Activation parameters $\Delta H^{\ddagger}$ and $\Delta S^{\ddagger}$ were obtained from Eyring plots; activation energies, E_a, were obtained from Arrhenius plots.

X-ray diffraction analysis

The crystal data were determined using a Bruker Apex 2 X-ray (three-circle) diffractometer with a Mo sealed X-ray tube (Kα = 0.70173 Å) at 110 K. Weighted least squares refinement on F^0 was used for refining the structures. At idealized positions, hydrogen atoms were placed and fixed isotropic displacement parameters were used to refine them. Anisotropic displacement parameters were employed for all non-hydrogen atoms. The following programs were used: data collection, APEX3; data reduction, SAINT; absorption correction, SADABS; and cell refinement and structure solutions, SHELXS/XT. The final data presentation and structure plots were generated in Olex2.30 Crystallographic data for the complexes are deposited in the Cambridge Crystallographic Data Centre; their numbers are: CCDC 1965616, CCDC 1965614 and CCDC 1965615.

Electrochemistry

A custom made three-necked conical shaped flask with an outlet port/gas inlet equipped with a three-electrode setup was used to obtain cyclic voltammograms (CVs) using CH1600E electrochemical analyzer (HCH instruments, Inc.). The Working electrode was a 0.071 cm^2 glassy carbon dish electrode, the counter electrode was a platinum wire and the reference electrode was a solution of 1 mM $Ag/AgNO_3(CH_3CN)$ in a Vycor-tipped glass tube. Diamond paste (3 µm) was used to polish the working electrode and a blanket of Ar was maintained over the solution throughout the experiment following an initial Ar purge

for 5 min. All CVs were obtained in CH_3CN at room temperature using 0.1 M [n-Bu_4N][PF_6] as the electrolyte and 2.0 mM in analyte. All potentials were shown relative to the Fc/Fc+ couple at 0.00 V. Bulk electrolysis experiments were conducted using 3 mm glassy carbon working electrode, Ni–Cr-coiled wire counter electrode and 1 mM $Ag/AgNO_3(CH_3CN)$ reference electrode. The electrochemical cell was charged with 10 mL of 0.1 M [n-Bu_4N][PF_6] in CH_3CN and purged with Ar to deplete O_2. To the cell 2 x 10^{-5} mol of the catalyst and 50 equivalents of trifluoracetic acid (TFA) were added. CV was recorded in order to ensure the experiment was under catalytic conditions and the bulk electrolysis was performed at -1.61 V vs. Fc/Fc^+ for 1 hr and the overhead gas was analyzed using gas chromatography (GC) to detect H_2.

Calculation of Overpotential

$$\text{overpotential} = |E_{H+} - E_{cat/2}|$$

E_{H+} is the thermodynamic potential for hydrogen production from trifluoroacetic acid with the effects of homoconjugation taken into account.[100-101] For 0.1 M trifluoroacetic acid in MeCN referenced to Fc/Fc^+, this value equals to -0.65 V. $E_{cat/2}$ is the applied potential at which the catalytic current (i_{cat}) is half of its maximum value. The overpotential for both complexes were measured in the presence of 0.1 M trifluoroacetic acid and was determined as described by Appel and Helm.[102] An example for complex $[Fe(CO)_3][Fe(CO)_2NiN_2S_2]$ (**1**) is shown in Figure II-1.

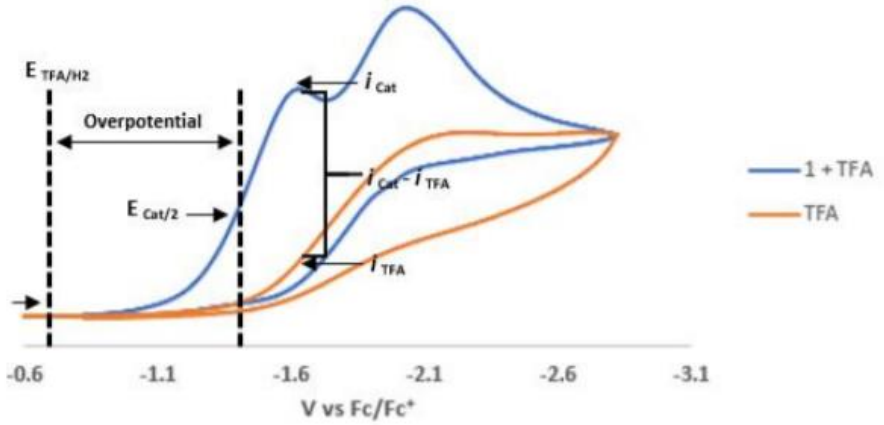

Figure II-1. Cyclic voltammograms of 2 mM 1 in the presence of 0.1 M TFA in MeCN at a scan rate of 200 mV/s (blue trace) and 0.1 M TFA without the catalyst (orange trace). This illustrates how to calculate Ecat/2 for the determination of the overpotential.

Calculation of Turnover Frequency (TOF)

TOF frequency was calculated according to the modified equation as published by the Darensbourg group.[96, 103] The general form of the equation that uses i_{cat} was modified to compensate for the background acid contribution by subtracting the i_{TFA}.

$TOF = 1.94\ V^{-1} \times \nu\ (Vs^{-1}) \times [i_{cat} / i_p]^2$

$TOF = 1.94\ V^{-1} \times \nu\ (Vs^{-1}) \times [i_{cat} - i_{TFA} / i_p]^2$

ν = scan rate

i_{cat} = total current measured upon adding acid (TFA) to the catalyst

i_{TFA} = background current measured from the acid (TFA) at the potential of i_{cat}

i_p = current measured from the catalyst in absence of acid

$i_{cat} - i_{TFA}$ = corrected current response from the catalyst only.

The concentration of the acid was sequentially increased until the TOF was fairly constant as shown in Table II-1 for complex **1**.

Table II-1. Values used for the calculation of TOF for 1 at various TFA concentrations in MeCN at a scan rate of 200 mV/s. Due to the appearance of the catalytic peak at -1.48 V, the value for ip with no added acid was taken from the first reduction at -1.82 V

Acid (µL)	i_{cat} (A)	i_{TFA} (A)	$i_{cat} - i_{TFA}$ (A)	TOF (s^{-1})
0	0.0000271	0.000	0.0000276	0.000
50	0.00246	0.000627	0.00183	12.26
100	0.00421	0.00220	0.00201	14.74
150	0.00591	0.00374	0.00217	17.05
200	0.00634	0.00414	0.00220	17.53

Experimental setup for bulk electrolysis and gas chromatography

Custom made three-neck truncated conical shaped flaks with an outlet port/gas inlet was the apparatus used for bulk electrolysis experiments. A Ni-Cr-coiled wire counter electrode, an $Ag/AgNO_3$ reference electrode, and a 3 mm glassy carbon working electrode were placed in the necks of the cell. The Ni-Crcoiled wire placed in a glass tube with a medium glass frit served as the counter electrode. A glass tube containing a Ag wire immersed in a 1 mM solutions of $AgNO_3$ in CH_3CN separated from the main solution by a Vycor frit was the contents of the reference electrode. To the electrochemical cell 10 ml of 0.1 M $[n\text{-}Bu_4N][PF_6]$ in MeCN was added and then purged with Ar to remove all O_2. To the cell $2x10^{-5}$ mol of complex 1 and 50 equivalents of trifluoroacetic acid (TFA) were added. To ensure that the experiment was under catalytic conditions, a cyclic voltammogram was recorded. After 30 minutes of bulk electrolysis performed at -1.61 V vs Fc/Fc^+, 1 mL of

methane was added as the internal standard. An Agilent Trace 1300 GC attached with a thermal conductivity detector and a custom-made 120 cm stainless steel column packed with Carbosieve-II was used to identify gases. The column was kept at a temperature of 200 ^{o}C and Ar was used to carry the gas during the separation. The detector was set to a temperature of 250 ^{o}C. Approximately 200 µL are withdrawn from the headspace gas after bulk electrolysis to quantify H_2 production. The syringe used was a 0.5 mL Valco Precision Sampling Syringe (Series A-2) equipped with a Valco Precision sampling needle with a 5-point side port. By determining the relative response factor of H_2 and the internal standard, H_2 can be quantified. A calibration curve was used that plotted ($area\ of\ H_2$ / $area\ of\ CH_4$) vs ($mL\ of\ H_2\ mL\ of\ CH_4$). It was calculated previously in our lab by recording the gas chromatograms of different amounts of H_2 vs 1 mL of methane. The calibration curve had the linear equation of y = 2.9757x + 0.0226 with R^2 value of 0.9987.5 Two bulk electrolysis experiments at -1.61 V in CH_3CN were carried out with 100 mmol of TFA, in absence of catalyst. The average charge passed and the average faradic efficiency was 1.58 C and 94.43% respectively. The charge passed vs time plots and gas chromatograms are shown in Figure SII-2 and the results are tabulated in Table II-2. The background H_2 produced from TFA was accounted for by subtracting the former from the total H_2 produced from the bulk electrolysis experiments with 2 mM catalyst and 50 equivalents of TFA. The gas chromatograms from the bulk electrolysis experiments with the catalysts are shown in Figure II-3. We posit that the peak at ca. 2.3 min in the gas chromatograms is due to N_2/O_2 from the atmosphere that contaminated the needle of the gas-tight syringe prior to the insertion of the head space gas into the gas chromatograph. The faradic efficiency and the corrected TON are tabulated in tables II-3.

Table SII-2. Charge passed (C) and Faradaic efficiency from bulk electrolysis experiments of 100 mM TFA in CH_3CN at -1.61 V for 30 min.

Exp.	Coulombs Passed (C)	Area of H_2	Area of CH_4	Ratio: Area H_2 / Area CH_4	Theoretical H_2 (mL)	Observed H_2 (mL)	Faradaic Efficiency (%)
1	1.41	0.181	0.348	0.518	0.179	0.167	93.14
2	1.56	0.1619	0.276	0.587	0.198	0.189	95.71

Average Coulombs passed = 1.58 C

Theoretical H_2 (mL) = (((Coulombs Passed/96500)/2) x 24.5) x 1000

Observed H_2 (mL) = (Ratio – 0.0226)/2.9757

Faradaic Efficiency = [Observed H_2 / Theoretical H_2] x 100

Table SII-3. Charge passed (C) and corrected TON from bulk electrolysis experiments of 2mM 1 and 50 equivalents of TFA in CH_3CN at -1.61 V for 30 min.

Exp.	Coulombs Passed (C)	Corrected Coulombs Passed (C)	Faradaic Efficiency (%)	TON	Corrected TON
1	2.52	1.04	83.22	0.65	0.27
2	2.11	0.66	73.54	0.54	0.17
Average	2.32	0.85	78.38	0.60	0.22

Faradaic Efficiency was calculated in the same was as that of the free acid

TFA TON = (Coulombs passed / (Amount of cat (in mmol) x 0.00001 x 96500 x 2)

Corrected Coulombs (C) = Coulombs passed – Average Coulombs passed for TFA only

Corrected TON = (Corrected Coulombs passed / (Amount of cat (in mmol) x 0.00001 x 96500 x 2)

(A)

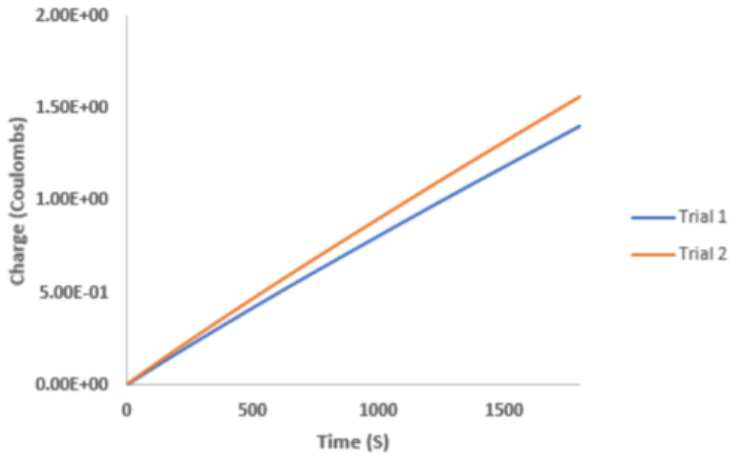

(B)

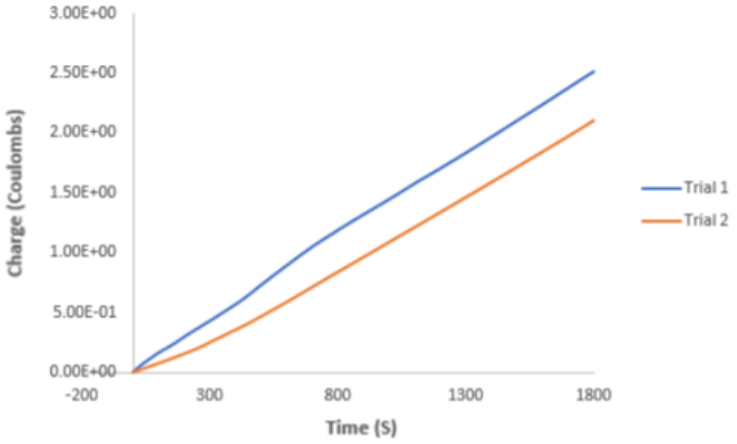

Figure II-2. (A) Coulombs passed vs. time for the bulk electrolysis of 50 equivalents of trifluoroacetic acid in MeCN at -1.61 V for 30 minutes. (B) Coulombs passed vs. time for the bulk electrolysis of 50 equivalents of trifluoroacetic acid in the presence of 1 in MeCN at -1.61 V for 30 minutes.

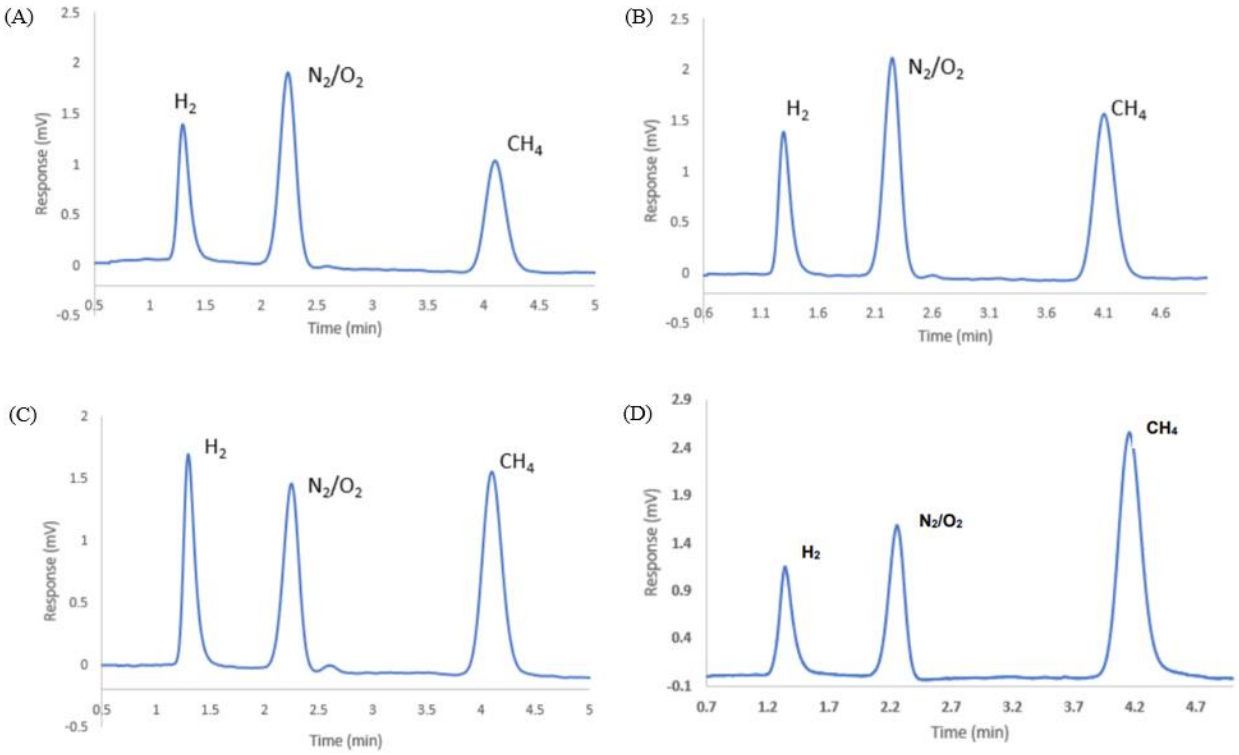

Figure II-3. (A) Gas chromatogram of the 1st run from the bulk electrolysis at -1.61 V of 50 equivalents of trifluoroacetic acid for 30 minutes. (B) Gas chromatogram of the 2nd run from the bulk electrolysis at -1.61 V of 50 equivalents of trifluoroacetic acid for 30 minutes. (C) Gas chromatogram of the 1st run from the bulk electrolysis at -1.61 V of 50 equivalents of trifluoroacetic acid with 2 mM 1 in MeCN for 30 minutes. (D) Gas chromatogram of the 2nd run from the bulk electrolysis at -1.61 V of 50 equivale nts of trifluoroacetic acid with 2 mM 1 in MeCN for 30 minutes.

Synthesis

(μ-pdt)[Fe(IMe)(NO)(CO)][Fe(CO)$_3$]$^+$[BF$_4$]$^-$

A solution of (μ-pdt)[Fe(CO)$_2$IMe][Fe(CO)$_3$], (0.88 g, 1.95 mmol) dissolved in 50 mL of CH_2Cl_2. This red solution was chilled to 0 °C in an ice bath. A second solution of [NO]$^+$[BF$_4$]$^-$ (0.22 g, 1.95 mmol) and 18-crown-6 (0.52 g, 1.95 mmol) was prepared in 40 mL of CH_2Cl_2 in an ice water bath. This pale-yellow solution was magnetically stirred for up to 30 min to allow for complete dissolution of the nitrosonium salt, and then was slowly added to the solution of (μ-pdt)[Fe(CO)$_2$IMe][Fe(CO)$_3$]. The reaction was monitored by solution IR until formation of product for 30 min. The resulting dark red solution was anaerobically filtered through Celite. The product was precipitated by addition of excess hexanes. The final product was washed with hexanes and diethyl ether at 0 °C to remove any unreacted starting materials

IR (CH_2Cl_2) ν(CO): 2085(s), 2058(s), 2018(s); ν(NO): 1809(s)

(μ-pdt)[(CO)$_3$Fe^1][Fe^I(CO)$_2$•NiN$_2$S$_2$] (1)

A solution of (μ-pdt)[Fe(CO)$_3$]$_2$ (386 mg, 1.00 mmol), NiN_2S_2 (277 mg, 1.00 mmol) and trimethylamine N-oxide (TMANO) (75 mg, 1.00 mmol) in CH_2Cl_2 (20 ml) was stirred for 30 mins at ca. 22°C. The resulting solution was dried under vacuum and washed with 20 mL (x3) hexane. The mixture was redissolved in CH_2Cl_2 and filtered through celite to remove any unreacted starting material and X-ray quality crystals for complex **1** were obtained by layering moderately concentrated solutions in CH_2Cl_2 with hexanes at -28 ℃ under N_2 atmosphere (Figure II-4).

IR (CH_2Cl_2, cm^{-1}): *ν*(CO) 2032, 1962, 1900; ESI-MS$^+$: *m/z* 633.85 (Calc. for [M]$^+$, 633.86). Elem. Anal. Calc'd (found) for $C_{17}H_{24}Fe_2N_2NiO_5S_4$ (MW = 635.01 g mol^{-1}): C,

32.15 (32.21); H, 3.81 (3.90); N, 4.41 (4.52). ^{1}H NMR (400 MHz, CD_2Cl_2): δ 2.00 – 4.50 (18H), 1.56 (4H), 1.27 (2H)

.

(μ-pdt)[$(CO)_3Fe^{I}$][{Fe(NO)}^{II}(IMe)•NiN_2S_2]$^{+}$BF_4^- (2)

A solution of (μ-pdt)[$Fe(CO)_3$][(Fe(NO))^{II}(IMe)(CO)]$^{+}$ BF_4^- (543 mg, 1.00 mmol) and NiN_2S_2 (277 mg, 1.00 mmol) in CH_2Cl_2 (20 ml) was stirred for 3 hours at room temperature. The resulting solution was dried under vacuum and washed with 20 ml (x3) diethyl ether. The mixture was redissolved in CH_2Cl_2 and filtered through celite to remove any unreacted starting material and X-ray quality crystals for complex **2** were obtained by layering moderately concentrated solutions in CH_2Cl_2 with hexane and ether (3:1) at -28 ℃ under N_2 (Figure II-4).

IR (CH_2Cl_2, cm^{-1}): *ν*(CO) 2056, 1990; *ν*(NO) 1740; ESI-MS^{+}: *m/z* 703.93 (Calc. for $[M]^{+}$, 703.94). Elem. Anal. Calc'd (found) for $C_{20}H_{32}Fe_2N_5NiO_4S_4BF_4$ (MW = 791.93 g mol^{-1}): C, 30.33 (30.95); H, 4.07 (3.92); N, 8.84 (8.17)

.

(μ-pdt)(μ-H)[(PMe_3)$(CO)_2Fe^{II}$][Fe^{II}(CO)(PMe_3)•NiN_2S_2]$^{+}$BF_4^- (3)

A solution of (μ-pdt)(μ-H)[$Fe^{II}(CO)_2(PMe_3)]_2^{+}$ PF_6^- (570 mg, 1.00 mmol) and NiN_2S_2 (277 mg, 1.00 mmol) in CH_2Cl_2 (20 ml) was stirred for 30 mins at room temperature while irradiated by a sunlamp. The resulting solution was dried under vacuum and washed with 20 mL (x3) hexane. The mixture was redissolved in CH_2Cl_2 and filtered through celite to remove any unreacted starting material. X-ray quality crystals for complex **3** were obtained by layering moderately concentrated solutions in CH_2Cl_2 with hexanes at -28 ℃ under N_2 (Figure II-4).

IR (CH_2Cl_2, cm^{-1}): *ν*(CO) 2023, 1968, 1929; ESI-MS$^+$: *m/z* 730.95 (Calc. for $[M]^+$, 730.97). Elem. Anal. Calc'd (found) for $C_{21}H_{43}Fe_2N_2NiO_3P_2S_4BF_4$ (MW = 818.96 g mol^{-1}): C, 30.80 (31.00); H, 5.29 (5.40); N, 3.42 (3.76). ^{31}P NMR (400 MHz, Dimethyl sulfoxide-d_6): δ 21.13 (PMe_3, $[Fe(CO)_2PMe_3]$), -8.69 (PMe_3, $[Fe(CO)(PMe_3)(NiN_2S_2)]$) ($PF_6^-$, -144.24)

(μ-H)[$(PMe_3)(CO)_2Fe^{II}Fe^{II}(CO)(PMe_3)(NiN_2S_2)$]$^+$BArF$^-$

A 100 mL long-necked Schlenk flask containing a magnetic stir bar was charged with (μ-pdt)$[Fe^{II}{}_2(CO)_4(PMe_3)_2]^+PF_6^-$ (0.0314 g, 0.05 mmol) and NiN_2S_2 (0.0138 g, 0.05 mmol). 15 mL of THF was added and the solution was stirred for 1 h at 25°C under white sunlamp. The completion of the reaction was monitored with IR. The product was washed with hexane (3 x 10 mL) and diethyl ether (2 x 10 mL) to remove unreacted starting materials. NaBarF (0.0443 g, 0.05 mmol) was added to a CH_2Cl_2 solution of the product and was stirred for 2 h. The solution was evaporated in vacuuo and was redissolved in THF. The THF solution was filtered over a bed of celite to remove insoluble $NaPF_6$. Layering the CH_2Cl_2 solution with hexane produced dark brown X-ray quality crystals at -28 ^oC. IR (CH_2Cl_2) ν(CO): 2023, 1968, 1929.

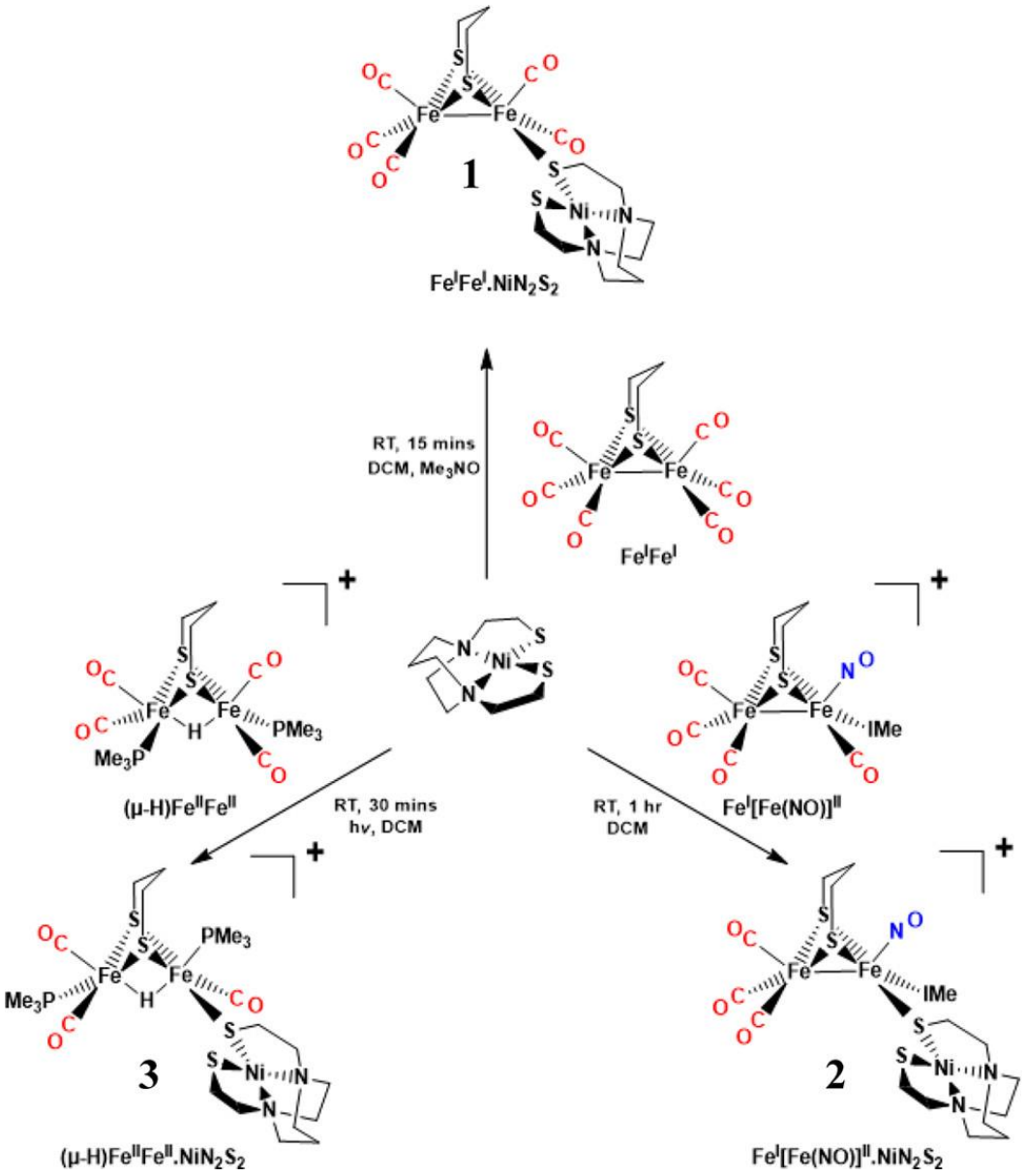

Figure II-4. Synthetic scheme for complexes (**1**), (**2**) and (**3**)

[$FeNO_2(PPh_3)_2$]

A 100 mL Schlenk flask containing a magnetic stir bar was charged with [Fe(CO)3(NO)][NaCE] (0.458 g, 0.001 mol) and [NO][BF_4] (0.097 g, 0.0008 mol). 25 mL of THF was added and the solution was stirred for 30 mins at 25 °C to obtain [$Fe(CO)_2(NO)_2$]. A second 100 mL Schlenk flask containing a magnetic stir bar was charged with PPh_3 (0.437 g, 0.0016 mol) and the contents of first Schlenk flask was evaporated into the second Schlenk flask using vacuum technique. The mixture was stirred for 72 hrs at at 80°C to obtain [$Fe(NO)_2(PPh_3)_2$].

IR (CH_2Cl_2, cm^{-1}): *ν*(NO) 1718(m), 1676(s)

[$FeNO_2(PPh_3)_2$]$^+$[BF_4]$^-$

A 100 mL Schlenk flask containing a magnetic stir bar was charged with [$Fe(NO)_2(PPh_3)_2$] (0.640 g, 0.001 mol) and 50 mL of DCM. A 50 mL round bottom flask was charged with $FcBF_4$ (0.273 g, 0.001 mol) and 25 mL of DCM and was sonicated for 15 mins until all the $FcBF_4$ was fully dissolved. The Schlenk flask was cooled for 0 °C in an ice bath and the $FcBF_4$ was added dropwise using a canula. The precipitated product was cleaned by washing with hexane and ether.

IR (CH_2Cl_2, cm^{-1}): *ν*(NO) 1815(m), 1767(s)

(^{15}NOFe(bme-dach)Fe$(NO)_2)^+B\boldsymbol{F_4^-}$

A 50 mL Schlenk flask containing a magnetic stir bar was charged with [^{15}NOFe(bme-dach)] (0.152 g, 0.0005 mol) and [$FeNO_2(PPh_3)_2$]$^+$[BF_4]$^-$ (0.363 g, 0.0005 mol). 25 mL of DCM was added and the solution was stirred for 30 mins at -10 °C to obtain (^{15}NOFe(bme-dach)Fe$(NO)_2)^+B\boldsymbol{F_4^-}$. The compound was precipitated at low temperature

adding excess amounts of ether and the isolated complex was washed with hexane and ether to remove any unreacted starting materials.

IR (CH_2Cl_2, cm^{-1}): *ν*(NO) 1807(m), 1738(s)

Theoretical Calculations

DFT calculations were performed using the Guassian 09 program using the complex 1 crystal structure as a geometric starting point. All subsequent structures were modified from this optimized structure using the TPSSTPSS functional with the 6-311++G(d,p) basis set for all nonmetal atoms and the 6-311+G basis set for the Ni and Fe atoms and were optimized in solvent using the SMD implicit solvation model with acetonitrile as the solvent.

CHAPTER III

SYNTHETIC METALLODITHIOLATE LIGANDS AS PENDANT BASES IN [$Fe^{I}Fe^{I}$], [$Fe^{I}[Fe(NO)]^{II}$] AND [(μ-H)$Fe^{II}Fe^{II}$] COMPLEXES[#]

Introduction

The search for innovative ligands to meet specific stereo- and electro-chemical requirements in catalyst development is of imminent interest to synthetic chemists. Biomimetics of the hydrogenase active sites have provided particular challenges and opportunities to explore fundamental properties of abiotic ligands that might provide function to the small molecules similar to that of the metalloenzymes that exist with many layers of control via the protein matrix.[5, 86, 104-106] The two most prominent hydrogenases, [FeFe]- and [NiFe]-H_2ase are thiolate-S bridged bimetallics, with diatomics attached to iron, CN^- and CO, in both.[5, 22, 107] Hence, for biomimetic purposes, organometallic chemists have used familiar ligands such as phosphines and **N**-heterocyclic carbenes, of similar donor ability to CN^-, but having the advantage that they avoid the problem of ligand-based, i.e., cyanide-nitrogen, protonation that does not direct the proton towards iron, an ultimate requirement for H^+/H^- coupling.[22, 49, 106-107] Such proton shuttling capability is readily arranged by the proteins, via an azadithiolate in the [FeFe]-H_2ase; a terminal cysteinyl sulfur operates in this function for the [NiFe]-H_2ase.[108]

[#]Major Parts of this chapter were reproduced with permission from (Kariyawasam Pathirana, K. D.; Ghosh, P.; Hsieh, C-H.; Elrod, L. C.; Bhuvanesh, N.; Darensbourg, D. J.; Darensbourg, M. Y., Synthetic Metallodithiolato Ligands as Pendant Bases in [$Fe^{I}Fe^{I}$], [$Fe^{I}[Fe(NO)]^{II}$], and [(μ-H)$Fe^{II}Fe^{II}$] Complexes. *Inorg. Chem*, **2020**, 59 (6), 3753-3763). Copyright **2020** American Chemical Society)

We have long had interest in metallodithiolates as a class of ligands, particularly MN_2S_2.[92] As cis-dithiolates, they are generally found as bidentate ligands creating M(μ-$S)_2$M" butterfly type structures.[92, 109] These ligands are tunable based on the hydrocarbon linkers between S and N, and N and N, as well as the characteristics of the central metal, M.[92] The most common of these are square planar MN_2S_2 with M = Ni^{II}, however square pyramidal systems (M = $(V{\equiv}O)^{2+}$, $[(NO)Fe]^{II}$ or $[(NO)Co]^{II}$) are also known to act as sulfur donor based metallo-ligands to various receivers, particularly low valent metals with additional carbonyl or nitrosyl ligands.[94]

Several of such bimetallic complexes have been developed in various laboratories as electrocatalysts for the hydrogen evolution reaction, HER, despite the absence of a well-positioned pendant base as a proton shuttle.[97, 110-112] Nevertheless, computational studies aimed to explore the mechanism of proton/electron coupling according to the electrochemical events displayed on the acid concentration-dependent cyclic voltammograms, indicated that one of the guiding principles was the actuation of hemi-lability, Figure III-1.[95] As shown in Figure III-1, dissociation of one dative RS→M bond opens up two reactive sites: a base on thiolate sulfur and a hole on the M available for addition of an electron. Specific examples are presented in Figure III-1; pathway **A** indicates addition of an electron, first to the open space on the 16-electron Ni^{II} side of the bimetallic. A fast electron transfer to the more electrophilic iron reduces Fe^{II} to Fe^{I} and opens the Fe-S bond. The **B** route indicates that the first added electron, buffered by the electron-delocalizing NO ligand, is insufficient to induce hemilability, but rather both an electron and proton are needed prior to S-Fe bond cleavage.[94] In this way, the MN_2S_2 ligands may create

a temporary but necessary pendant base, avoiding the synthetic requirement of building a permanently available strategically located Lewis base.[95]

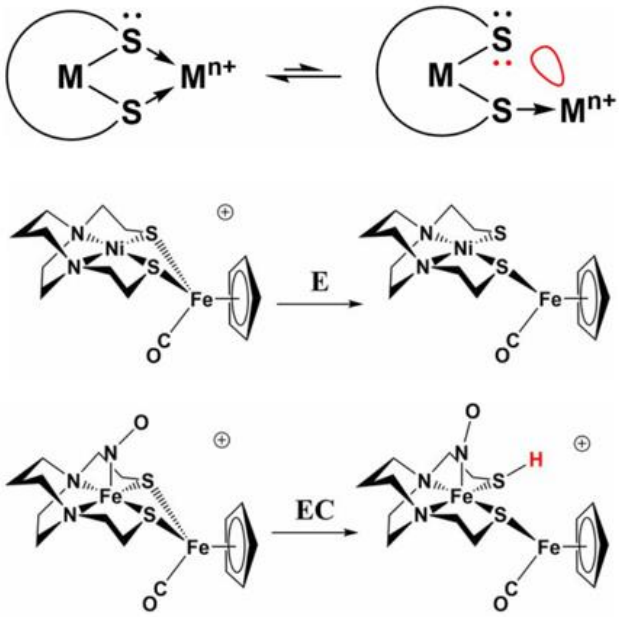

Figure III-1. Hemi-lability in MN_2S_2 bridging thiolates.

Synthetic analogues of the [2Fe2S] active site of [FeFe]-H_2ase provide a unique opportunity to explore the influences of specific changes in binuclear complexes. Previous studies on the ubiquitous (μ-pdt)$[Fe(CO)_3]_2$ concluded that rates of CO/CN^- ligand substitution processes correlate with fluxionality in the $Fe(CO)_3$ rotors, that is, the intramolecular CO_{ap}/CO_{ba} site exchange on individual metals.[30, 87, 113] Such rotation, likely promoted by an incoming ligand, coupled with shifting the electron density in the Fe---Fe bond, leads to an open site readily available to said donor, with concomitant release of a CO.[30] In this way an associative mechanism for ligand substitution on a pseudo 18-electron metal center is made possible, on individual and alternate iron centers. The mono-substituted (μ-pdt)$[Fe(CO)_3][Fe(CO)_2CN]^-$ is followed by the second process, yields the much

appreciated disubstituted, dianion, (μ-pdt)[$Fe(CO)_2CN]_2^{2-}$.[87] Phosphine mimics of this process lead to the analogous (μ-pdt)[$Fe^I(CO)_2PR_3]_2$, which is capable of taking up a proton in a binuclear oxidative addition reaction, yielding the bridging hydride, (μ-pdt)(μ-H)[$Fe^{II}(CO)_2PR_3]_2^+$, with oxidation state conversions of Fe^I to Fe^{II}.[114] While these CO/L substitution reactions are on alternate iron centers, in another study it was found that the nitrosonium ligand, NO^+, isoelectronic with CO but greater engendering electron deficiency on the metal to which it adds, promotes a second CO/L exchange on the same iron.[115] That is, a completely dissymmetric diiron complex is produced: (μ-pdt)[$Fe(CO)_3$][Fe(L')(NO)(L)]$^+$ where L = **N**-heterocyclic carbene, or phosphine. Notably the NO^+ ligand effectively oxidizes one iron in the diiron complex, giving the opportunity to contrast diiron complexes in three redox levels, Fe^IFe^I, $Fe^{II}Fe^{II}$ and Fe^IFe^{II}. We have attempted using the NiN_2S_2 metalloligand as a surrogate for phosphine or NHC in diiron complexes. We are particularly interested in assessing whether the metalloligand binds in bidentate or monodentate fashion, and if the latter, how does the unbound thiolate orient itself when twisted away from the first coordination sphere. Thus the trimetallic complexes were synthesized and characterized by XRD: (μ-pdt)[$Fe^I(CO)_3$][$Fe^I(CO)_2$•NiN_2S_2] (**1**), (μ-pdt)[$Fe^I(CO)_3$][{Fe(NO)}^{II}(IMe)•$NiN_2S_2]^+BF_4^-$ (**2**), and (μ-pdt)(μ-H)[$Fe^{II}(CO)_2(PMe_3)$][$Fe^{II}(CO)(PMe_3)$•$NiN_2S_2]$ $^+PF_6^-$ (**3**). Complex **1** was examined for response of the cyclovoltammogram to added equivalents of acid i.e. for indications of electrocatalytic proton reduction.

Synthesis

Complex (1). Scheme III-1 describes out the synthetic protocol employed to obtain the three complexes of this study. Direct combination of the (μ-pdt)[$Fe^{I}(CO)_3$]$_2$ parent compound with NiN_2S_2 over the course of 1h showed negligible reaction even on heating. However, with addition of the decarbonylating agent Me_3NO the solution color immediately changed from red to dark brown with release of CO_2 and giving the desired complex **1** (**Scheme III-1**).

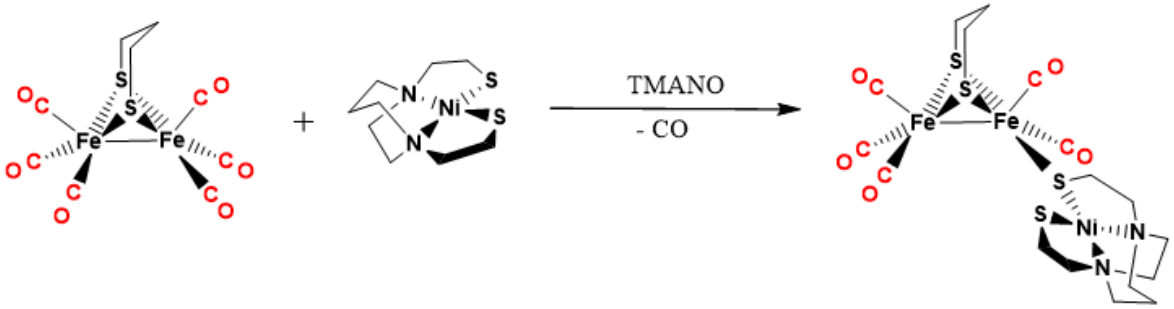

Scheme III-1. Synthesis of complex 1 from (μ-pdt)[$Fe^{I}(CO)_3$]$_2$

Infrared spectroscopy showed a bathochromic shift of *ν*(CO) stretching frequencies to 2032(s), 1962(s), 1900(w) upon binding of the electron-donating NiN_2S_2 ligand (Figure III-2). The pattern of *ν*(CO) stretching frequencies matched that of the (μ-pdt)[$Fe^{I}(CO)_3$][$Fe^{I}(CO)_2PR_3$] species indicative of monodentate binding of the NiN_2S_2 ligand to the diiron core (Table III-1). The slight lowering of *ν*(CO) values indicates that the NiN_2S_2 metallodithiolate ligands are better donor ligands than phosphines.[116-117]

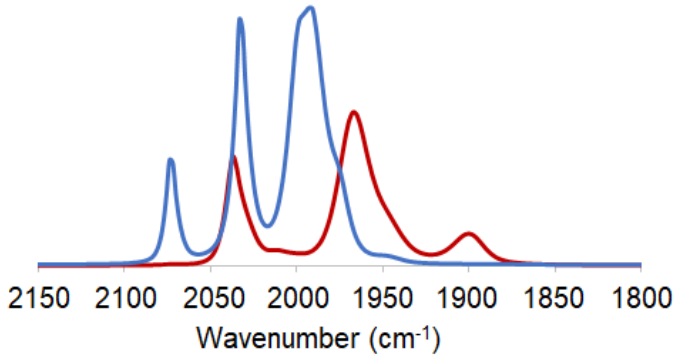

Figure III-2. IR spectrum of **1** in CH_2Cl_2 (Red trace). IR spectrum of the starting material (μ-pdt)[$Fe^{I}_2(CO)_6$] (Blue trace).

Positive-ion ESI mass spectrum of **1** in CH_2Cl_2 matches the calculated isotopic pattern (Figure III-3) and the ^{1}H NMR provides the accurate integration and demonstrate matching features to similar compounds that contains Ni(bme-dach) ligand (Figure III-4).

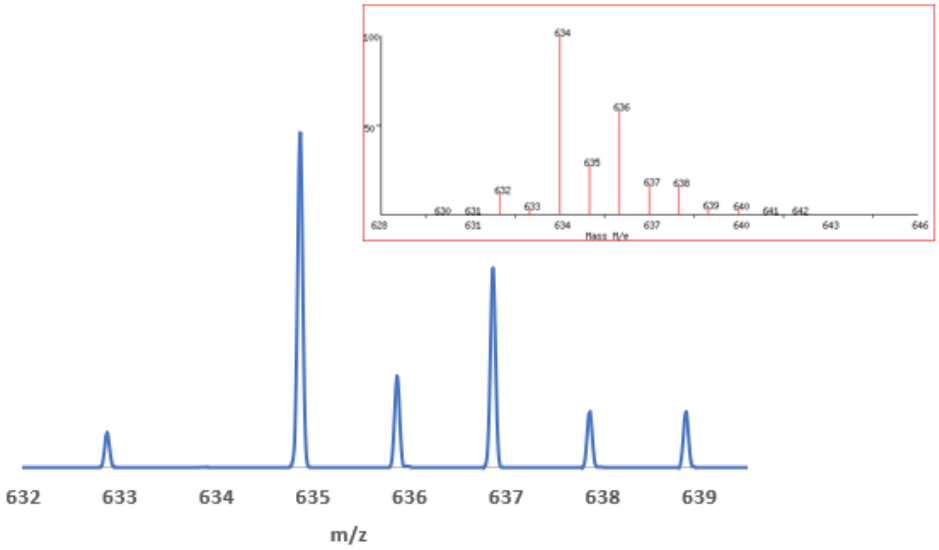

Figure III-3. Positive-ion ESI mass spectrum of **1** in CH_2Cl_2; inset: Calculated isotopic distribution

Nevertheless, addition of PMe_3 to **1** results in displacement of the NiN_2S_2 ligand forming (μ-pdt)[$Fe^I(CO)_3$][$Fe^I(CO)_2PMe_3$], **1-PMe$_3$**. It is interesting to note that, unlike NiN_2S_2, PMe_3 reacts directly with the parent compound (μ-pdt)[$Fe^I(CO)_3$]$_2$ without the need for oxidative assistance in the elimination of CO. As the NiN_2S_2 is a better electron-donating ligand than PMe_3, we postulate that this discrepancy is due to the larger steric hindrance from NiN_2S_2 in the associative substitution process.

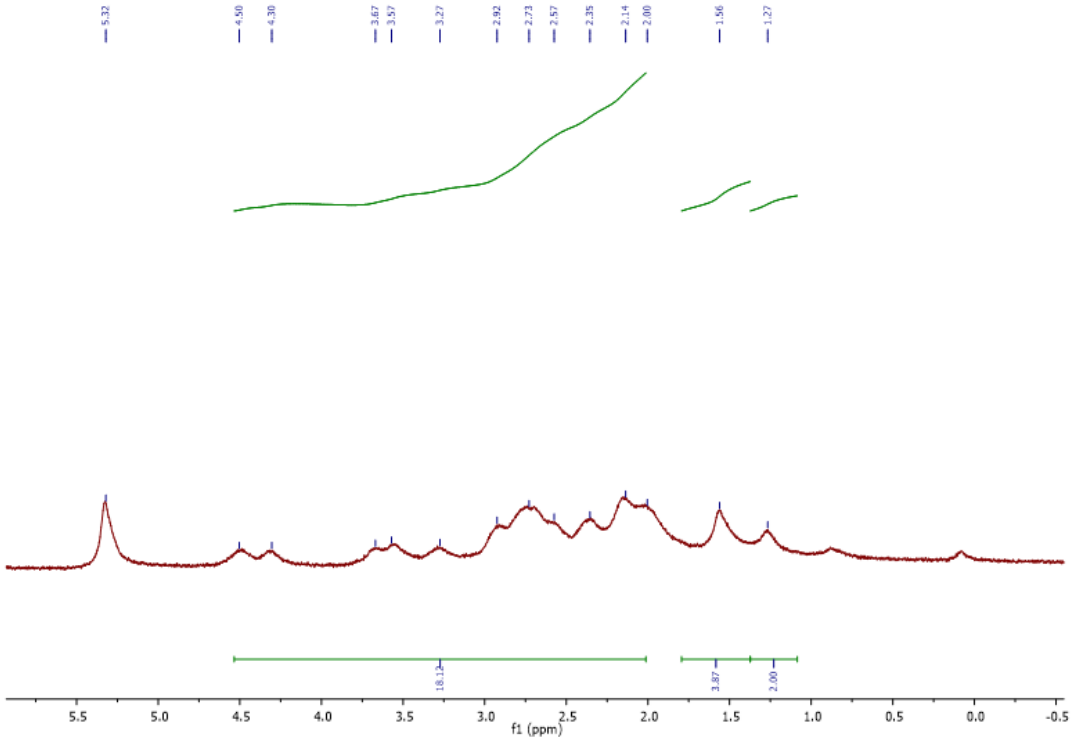

Figure III-4. ^{1}H NMR Spectrum of **1** at 23.2 ^{o}C using a 400 MHz NMR under N_2 referenced to residual CH_2Cl_2

Complex (2). On mixing the parent compound (μ-pdt)[Fe(CO)$_3$][(Fe(NO))^{II}(IMe)(CO)]$^+$ BF_4^- with NiN_2S_2, a clean conversion led to the paramagnetic complex **2** (**Scheme III-2**) that contains a fully substituted iron. Consistent with the better donor ability of NiN_2S_2, similar bathochromic shifts in ν(CO) and ν(NO) stretching frequencies were observed (Figure III-5A).

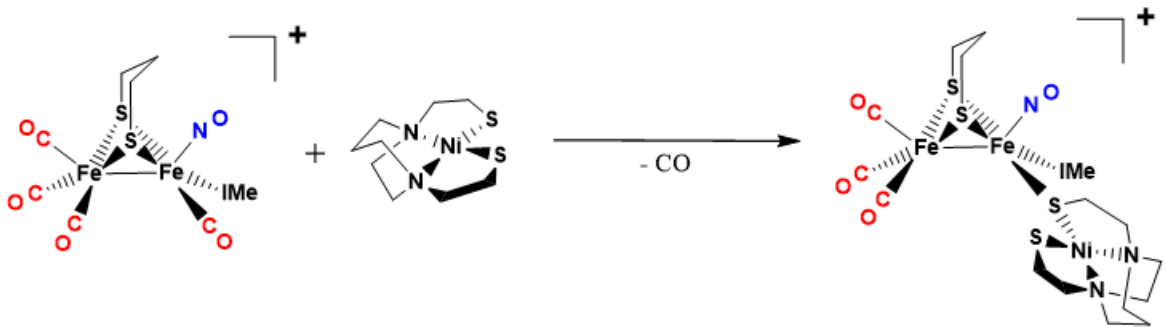

Scheme III-2. Synthesis of complex **2** from (μ-pdt)[Fe(CO)$_3$][(Fe(NO))^{II}(IMe)(CO)]$^+$ BF_4^-

The X-band EPR spectra of complex **2**, collected in perpendicular mode field polarization in CH_2Cl_2 solutions at 298K, showed the presence of an S = 1/2 species with a $g_\perp$ value of 2.09 (Figure III-5B). It is important to note that the NiN_2S_2 ligand substitutes the CO on [{Fe(NO)}^{II}(IMe)(CO)] center without any external assist from a reagent such as Me_3NO unlike in the case of complex **1**. Furthermore, in terms of steric hindrance it seems unlikely that the NiN_2S_2 would react easily with the iron center that already contains a bulky IMe ligand. **N**-heterocyclic carbene (IMes or IMe) stabilized (μ-pdt)[Fe^I(CO)$_3$][{Fe(NO)}^{II}(IMe)L]$^+$ complexes have been previously studied with respect to CO exchange (within the [(Fe(NO))^{II}(CO)L] moiety) using PMe_3 and CN^- which seem to react similarly. The redox non-innocent ligand NO of the parent compound creates a {FeNO}^{7} unit in the [{Fe(NO)}^{II}(IMe)(CO)] center which makes it more oxidized compared

to the adjoining [$Fe(CO)_3$] center. Together with the electron withdrawing capability of NO, the [{Fe(NO)}^{II}(IMe)(CO)] center presents a better electrophile to the incoming NiN_2S_2 ligand which leads to the formation of trisubstituted iron. Positive-ion ESI mass spectrum of complex **2** in CH_2Cl_2 matches with calculated isotopic distribution (Figure III-6).

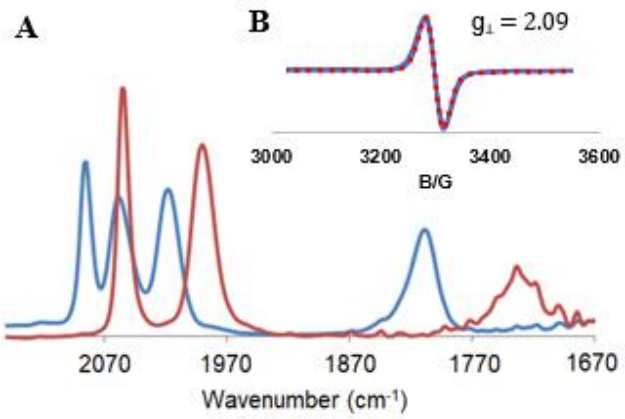

Figure III-5. (**A**). Overlay of IR spectra recorded in CH_2Cl_2 solution of **2** (red) and (μ-pdt)[$Fe^I(CO)_3$][{Fe(NO)}^{II}(IMe)(CO)]$^+$ BF_4^- (blue) starting material. (**B**). CH_2Cl_2 solution EPR spectra of **2** at 298 K The g value reported is from a simulation shown in red trace.

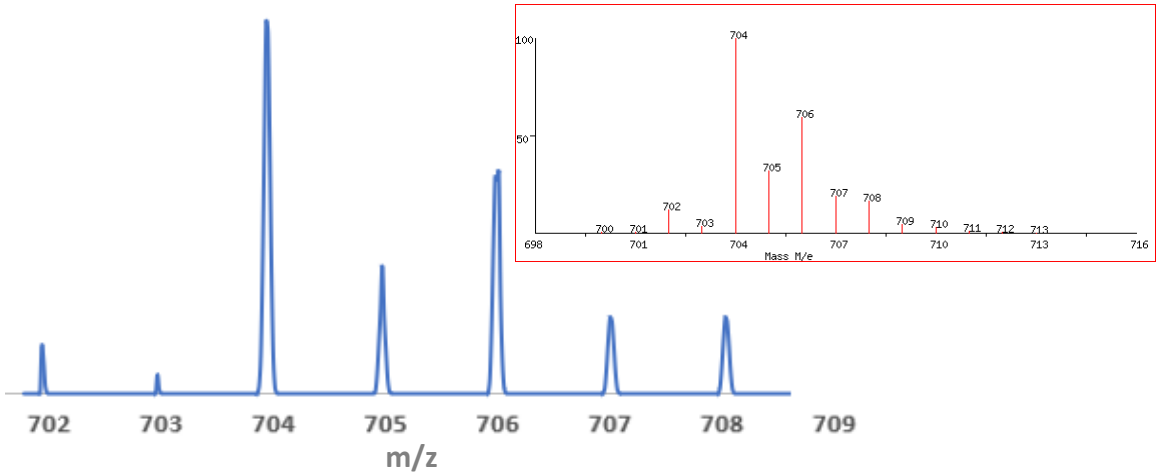

Figure III-6. Positive-ion ESI mass spectrum of **2** in CH_2Cl_2; inset: Calculated isotopic distribution

Complex (3) Photolysis by sunlamp irradiation of (μ-pdt)(μ-H)[$Fe^{II}(CO)_2(PMe_3)]_2^+PF_6^-$ in the presence of NiN_2S_2 formed complex **3**, over a period of 30 mins in CH_2Cl_2. (**Scheme III-3**).

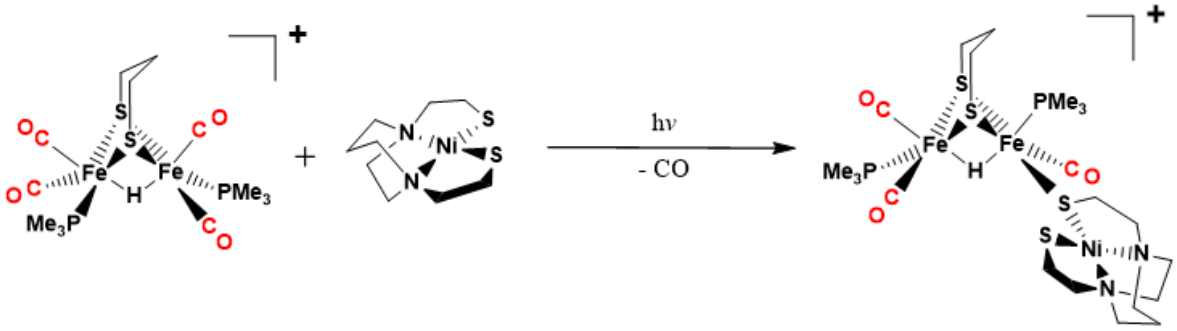

Scheme III-3. Synthesis of complex **3** from (μ-pdt)(μ-H)[$Fe^{II}(CO)_2(PMe_3)]_2^+PF_6^-$

The change in pattern and position of *ν*(CO) values, from 2032, 1990 to 2023, 1968, 1929 cm^{-1} reflects the increase in electron density in the diiron core, upon binding of NiN_2S_2. (Figure III-7) Thus, CO-substitution results in a tricarbonyl species making use of a metallodithiolate ligand, NiN_2S_2, as has been established using neutral or anionic σ-donor ligands.

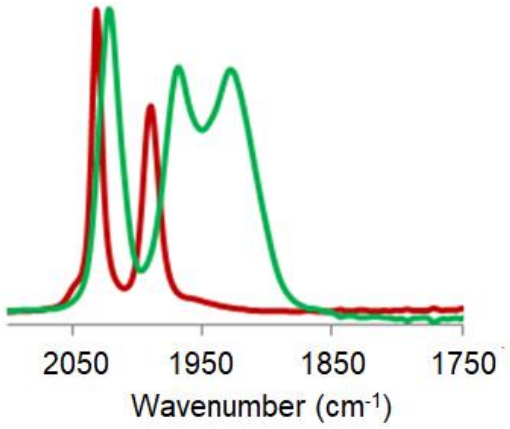

Figure III-7. IR spectrum of **3** in CH_2Cl_2 (Green trace). IR spectrum of the starting material (μ-H)[$(PMe_3)(CO)_2Fe^{II}Fe^{II}(CO)_2(PMe_3)]^+$ (Red trace).

Positive-ion ESI mass spectrum of complex **3** in CH_2Cl_2 matches with calculated isotopic distribution (Figure III-8) and the ^{31}P NMR spectra of complex **3** identifies two different ^{31}P signals that corresponds to $[Fe^{II}(CO)_2(PMe_3)]$ and $[Fe^{II}(CO)(PMe_3)\bullet NiN_2S_2]$ subunits (Figure III-9).

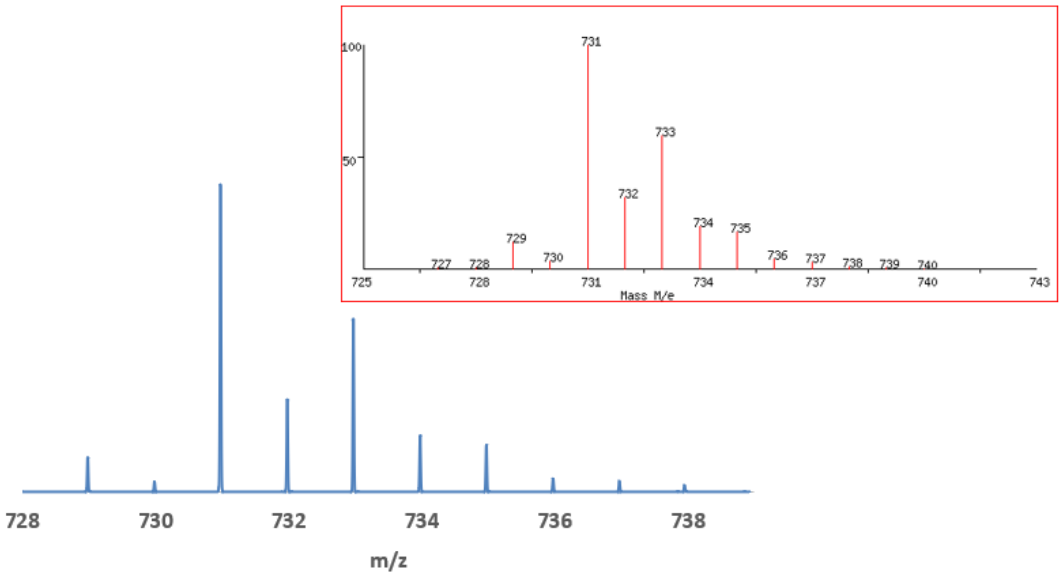

Figure III-8. Positive-ion ESI mass spectrum of **3** in CH_2Cl_2; inset: Calculated isotopic distribution

It is important to note that the visible light irradiation is required to drive the reaction forward. Complexes similar to $(\mu\text{-pdt})(\mu\text{-H})[Fe^{II}(CO)_2(PMe_3)]_2^+PF_6^-$ are known to eject a CO ligand upon photolysis, producing an open site for the incoming ligand. During the formation of complex **2**, NiN_2S_2 readily reacts with the $[\{Fe(NO)\}^{II}(IMe)(CO)]$ center without any chemical / physical assistance to remove one of its CO's to generate fully substituted iron center. However, formally being in the Fe^{II} oxidation state, parent compound $(\mu\text{-pdt})(\mu\text{-H})[Fe^{II}(CO)_2(PMe_3)_2]^+PF_6^-$ requires photolysis in order to create an open site for the incoming NiN_2S_2.

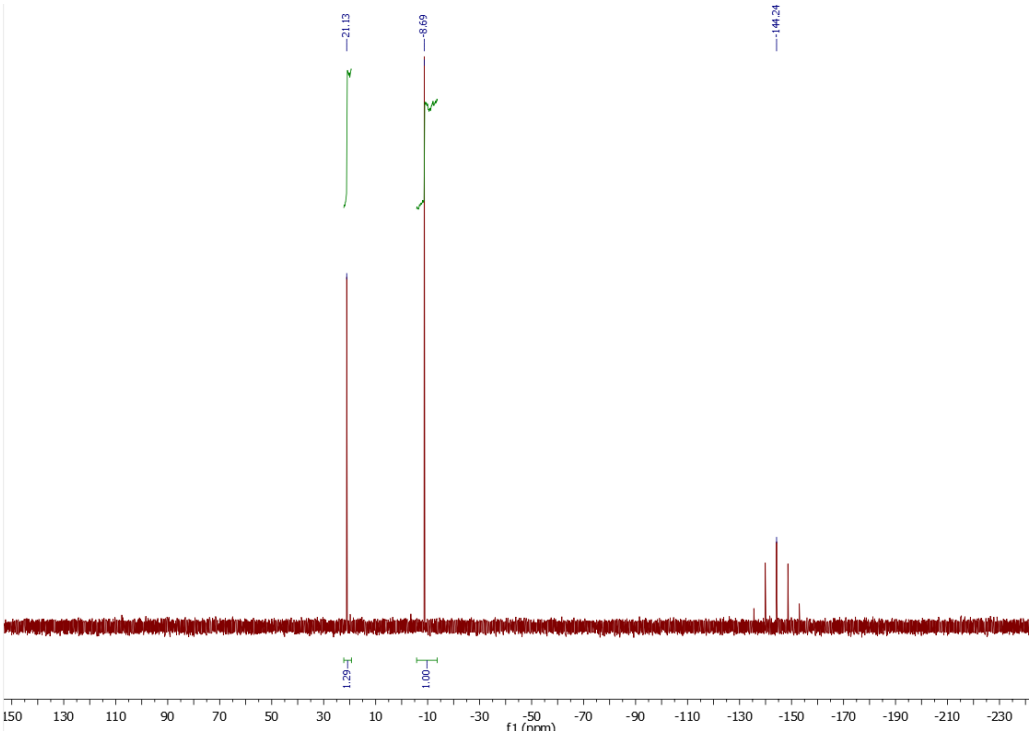

Figure III-9. ^{31}P NMR Spectrum of **3** at 23.2 ^{o}C using a 400 MHz NMR under N_2 referenced to residual DMSO

Table III-1: IR stretching frequencies for complexes 1, 2, 3, starting materials and their corresponding monosubstituted phosphine derivatives.

Complexes	*Diatomic vibrational frequencies* (cm^{-1})[a]
$[Fe^{I}Fe^{I}]$	
(μ-pdt)$[Fe^{I}_2(CO)_6]$	2072(m), 2037(s), 1990(s)[b]
(μ-pdt)$[Fe^{I}(CO)_3][Fe^{I}(CO)_2(PPh_3)]$	2044(s), 1984(s), 1931(m)[b]
(μ-pdt)$[Fe^{I}(CO)_3][Fe^{I}(CO)_2(NiN_2S_2)]$	2032(s), 1962(s), 1900(w)[c, d]
$[Fe^{I}(Fe(NO))^{II}]$	
(μ-pdt)$[Fe^{I}(CO)_3][(Fe(NO))^{II}(IMe)(CO)]^+$	2085(s), 2058(s), 2018(s), <u>1809(s)</u>[c]
(μ-pdt)$[Fe^{I}(CO)_3][(Fe(NO))^{II}(IMe)(PMe_3)]^+$	2061(s), 1996(s), <u>1759(m)</u>[c]
(μ-pdt)$[Fe^{I}(CO)_3][(Fe(NO))^{II}(IMe)(NiN_2S_2)]^+$	2056(s), 1990(s), <u>1740(m)</u>[c, d]
(μ-H)$[Fe^{II}Fe^{II}]$	
(μ-H) (μ-pdt)$[Fe^{II}(CO)_2(PMe_3)]_2^+$	2032(s), 1990(s)[c]
(μ-H) (μ-pdt)$[Fe^{II}(CO)_2(PMe_3)][Fe^{II}(CO)(PMe_3)(NiN_2S_2)]^+$	2023(s), 1968(m), 1929(m)[c, d]

[a]Values underlined are for NO; [b]Spectra measured in CH_3CN; [c]Spectra measured in CH_2Cl_2; [d]This work

X-ray Diffraction Analysis

X-ray quality crystals of complexes **1**, **2** and **3** were obtained by layering concentrated CH_2Cl_2 solutions with hexane at -28℃ under nitrogen. All three complexes show monodentate binding of the NiN_2S_2 ligand to the diiron unit. The distance between the bound sulfur and iron is around 2.3 Å and the distance between non-bound sulfur and the nearest iron within the trimetallic is around 4 Å in all complexes (Figure III-10). The Ni^{II} in the metalloligand is maintained within a square planar geometry and the $Ni{\bullet\bullet\bullet}Fe_{proximal}$ distances are around 3.6 Å. (Table 2)

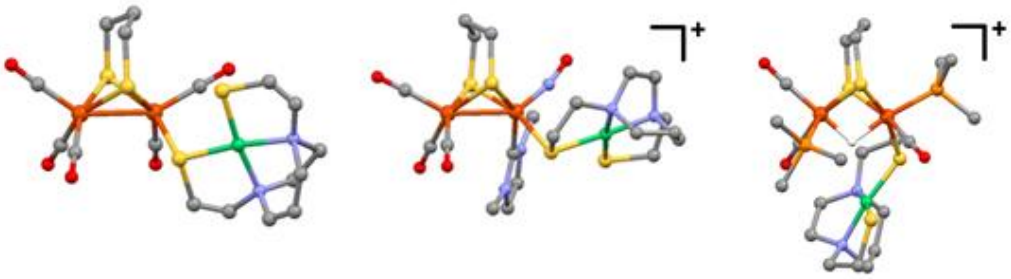

(**1**) (**2**) (**3**)

Figure III-10. Crystal structures of **1** and **2** as its BF_4^- salts and **3** as its PF_6^- salt.

Complex **1** shows that NiN_2S_2 binds to the iron center from a basal position with an $Fe{\bullet\bullet\bullet}S_b$ distance of 2.30 Å. The $FeS_2(C_{CO})_2S_{NiN2S2}$ moiety of **1** is square pyramidal ($\tau = 0.03$) The best plane of NiN_2S_2 is moderately coplanar with the FeS_pFe (where S_p is the S of pdt, proximal to NiN_2S_2) plane for complex **1**.

Complex **2** shows that the NiN_2S_2 binds to the iron center from the basal position of the pseudo-square pyramidal Fe. The Fe-Fe distance is slightly elongated (0.03 Å) compared to the analogous CN^- derivative. Due to the steric hindrance on the substituted iron side, both

the flap of the pdt unit and the Fe-N-O angle are bent towards the unsubstituted iron. The torsion angles, defined by $N_{ap} – Fe – Fe – C_{ap}$, are ~ 7°, for complexes **2** and the reported CN^- derivative, while it is much lower, ~1°, for the reported PMe_3 derivative. Conversely, the τ value for the substituted Fe, shows a discernable square pyramidal geometric distortion for complexes **2** and the reported PMe_3 derivative (0.22 and 0.26, respectively), while the reported CN^- substituted complex maintains a moderately regular square pyramid (τ = 0.1). This can be attributed to the steric interference from the PMe_3 and the metallodithiolate ligand as compared to the linear diatomic cyanide. The Ni^{II}, present in a perfect square plane, is 3.4 Å away from the proximal Fe, negating any bonding interaction. (Table III-2)

Table III-2: Selected metric parameters of 1, 2 and 3

	1	**2**	**3**
Fe-Fe / **Å**	2.551 (2)	2.592 (9)	2.579 (8)
$Fe-S_b$* / **Å** [a]	2.308 (4)	2.369 (9)	2.326 (1)
$Fe-S_{nb}$* / **Å** [b]	3.843 (5)	3.916 (1)	3.995 (2)
S*-S* / **Å** [c]	3.197 (5)	3.206 (1)	3.206 (2)
Ni_{disp} / **Å** [d]	0.020	0.013	0.057
S*-Ni-S* / °	93.6 (1)	95.03 (4)	94.9 (1)

[a] Fe-bonding sulfur distance. [b] Fe-nonbonding sulfur distance. [c] Sulfur-sulfur distance in NiN_2S_2. [d] displacement of Ni from N_2S_2 best plane.

In complex **3**, substitution of CO by NiN_2S_2 in $(\mu\text{-pdt})(\mu\text{-H})[Fe^{II}(CO)_2(PMe_3)]_2^+$ repositions the PMe_3 ligands from trans-basal to apical-basal, minimizing the steric interactions between the NiN_2S_2 and PMe_3. The flap created by the pdt is oriented towards

the di-substituted iron. Unlike other complexes, NiN_2S_2 positions itself in a manner such that the N_2S_2 plane is oriented towards the diiiron scaffold in complex **3**, thereby shortening the free-thiolate to potential bridging-hydride distance to 3.06 Å. (Table III-2) This feature serves as a potential structural platform to the 'free thiolate as a pendant base' thesis, such that the unbound thiolate can hold a proton for a convenient proton/hydride coupling in dihydrogen formation.

Electrochemistry

Complex **1** was selected for electrochemical analysis. Two irreversible reductions at -1.82 V and -2.1 V are assigned for Fe^IFe^I/Fe^IFe^0 and Fe^IFe^0/Fe^0Fe^0 couples respectively that appear to be quasi-reversible at higher scan rates (Figure III-11).[118] The starting material $(\mu\text{-pdt})[Fe(CO)_3]_2$ shows two irreversible reductions similarly at -1.34 V and -1.95 V[119] and it is reasonable to assume that in complex **1** the shift in reduction potentials towards a more negative value is due to the electron-donating capability of the appended NiN_2S_2 ligand which increases the electron density at the diiron core similarly to the $(\mu\text{-pdt})[Fe(CO)_3][Fe(CO)_2PMe_3]$.[118]

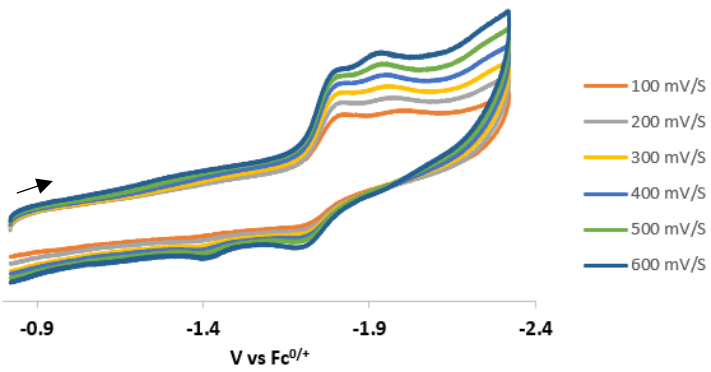

Figure III-11. Scan rate dependence of complex 1. (Scans were initiated in negative direction)

Similar trends have been observed in complexes such as (μ-pdt)$[Fe(CO)_2(PMe_3)]_2$ where a single reduction event corresponding to the Fe^IFe^I/Fe^IFe^0 couple occurs at -1.85 V.[119] A quasi-reversible reduction event is formed at -2.41 V which corresponds to $Ni^{II/I}$ reduction (Figure III-12). Bimetallic complexes that are composed of a metallodithiolate ligand and a Lewis acidic metal center usually show a positive shift in the reduction potential of the metal center in the metallodithiolate ligand due to the decrease in electron density around it.[92] However the reduction potential of Ni in complex **1** shows no significant shift compared to free NiN_2S_2.[120] One possible reason for this might be the initial reduction of the diiron core prior to the Ni reduction. When the diiron center first undergoes reduction, the effect on the reduction of the Ni center is minimized, making its reduction polential closer to the free NiN_2S_2.[120]

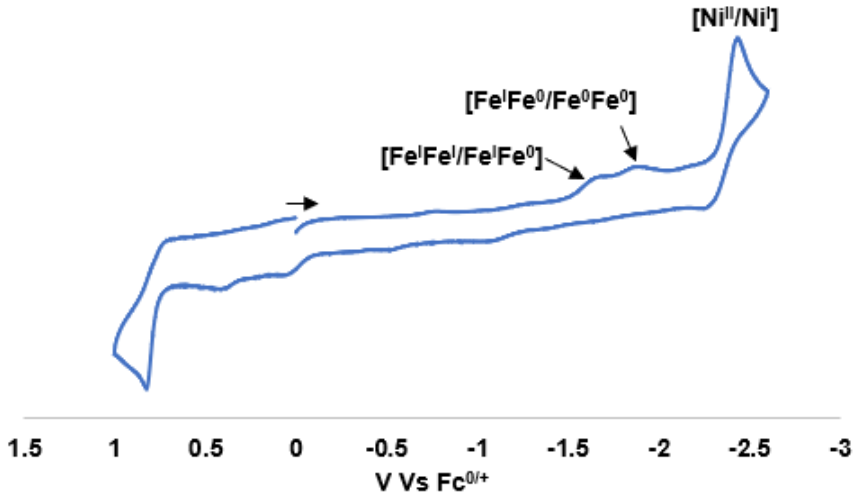

Figure III-12. CV of 2 mM of **1** under Ar in CH_3CN solutions containing 0.1 M $[tBu_4N][PF_6]$ as supporting electrolyte

To test the ability of complex **1** to respond electrochemically to added protons, cyclic voltammogram was recorded in the presence of trifluoroacetic acid (TFA) in CH_3CN. In the presence of 10 equiv. of acid, the IR spectrum shows little change in pattern indicating that complex **1** maintains its structural integrity (Figure III-13). However, a growing shoulder around ~2000 cm^{-1} might be due to a new protonated species, possibly at the unbound thiolate site (Figure III-13).

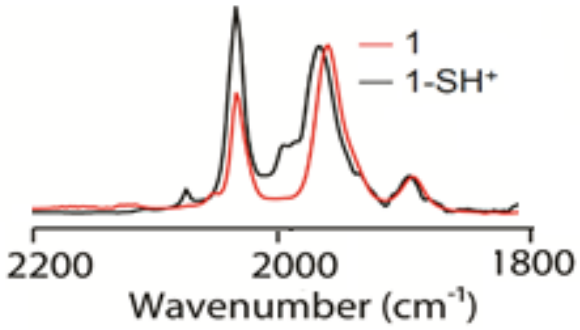

Figure III-13. Overlay of IR spectra of 1 and $1H^+$

Computational, DFT, studies indicated that the HOMO of complex **1** is centered around the unbound thiolate sulfur, further indicating its potential to undergo protonation (Figure III-14).

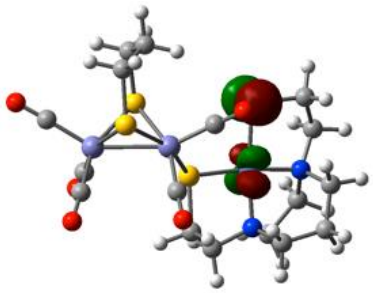

Figure III-14. HOMO of complex 1 according to DFT calculations.

The cyclic voltammogram of complex **1** upon sequential addition of aliquots of acid showed an increase in the cathodic current at the first reduction event at -1.82 V which is presumed to be the $Fe^{I}Fe^{I}/Fe^{I}Fe^{0}$ reduction (Figure III-15). Furthermore, a new, steadily increasing current event at -1.48 V can also be observed when increasing the concentration of acid in the medium (Figure III-15). The attribution of the reduction-induced cathodic current enhancement upon addition of TFA to electrocatalytic H_2 production was verified by gas chromatography and quantified by bulk electrolysis experiments performed at −1.61 V for 1 hr, in a CH_3CN solution containing 2 mM of catalyst and 50 equivalents of TFA.

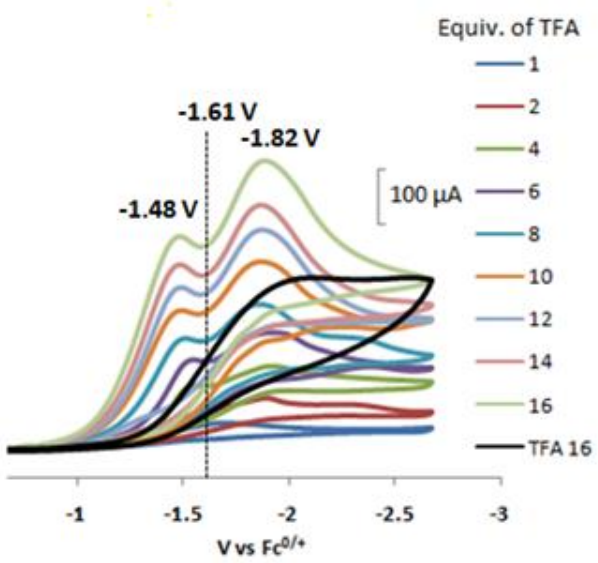

Figure III-15. Cyclic voltammograms of **1** in 2 mM CH_3CN solution with added equivalents of TFA. The black trace shows 16 equivalents of free TFA in absence of catalyst.

The plot of current heights of electrocatalytic waves vs acid concentration indicates steeper slopes for the event at -1.48 V compared to the all-CO starting material as well as (μ-pdt)$[Fe^{I}(CO)_3][Fe^{I}(CO)_2PPh_3]$ (Figure III-16) where the increase of sensitivity is in the order of **1** > (μ-pdt)$[Fe^{I}(CO)_3][Fe^{I}(CO)_2PPh_3]$ > (μ-pdt)$[[Fe(CO)_3]_2$. Many reported mimics of [FeFe]-H_2ase show catalytic properties following reduction of the Fe center which makes

it amenable to oxidatively add a proton converting it to a hydride.[114] Previous studies have shown that the all-CO complex is likely to have a EECC type electrocatalytic mechanism for proton reduction and the disubstituted (μ-pdt)[$Fe^{I}(CO)_2(PMe_3)]_2$ complex is likely to have a ECCE type mechanism for proton reduction, especially at higher scan rates; at lower rates, there is a decomposition.[119, 121] Furthermore, the disubstituted complex showed a greater sensitivity towards the added acid, probably due to the more stable hydride intermediate that formed during the HER. The mono substituted (μ-pdt)[$Fe^{I}(CO)_3$][$Fe^{I}(CO)_3PPh_3$] follows a similar trend as the complex **1** and shows a higher sensitivity towards the added acid compared to the all-CO complex. The greater sensitivity of complex **1** to added acid compared to both the mono phosphine substituted and the all-CO complexes is in agreement with the postulate that the metallodithiolate ligand might act as a pendant base. As a good donor ligand, it has the capability of increasing the electron density in the diiron core and in addition will stabilize the oxidized center following the oxidative addition of a proton to the iron. In the monodentate form, it harbors a nearby site for a proton to promote efficient proton/hydride coupling.

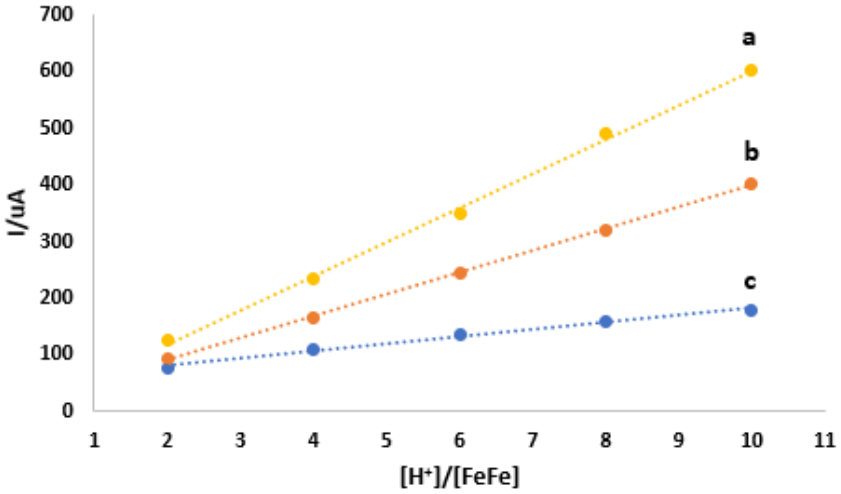

Figure III-16. Dependence of current heights of electrocatalytic waves on acid concentration. (a) 1 (-1.48 V), (b) (μ-pdt)[$Fe(CO)_3$] [$Fe(CO)_2PPh_3$] (-1.73 V) (c) (μ-pdt)[$Fe(CO)_3$]$_2$ (-1.95 V).

It is interesting to note that complex **1** shows an increase of catalytic current at -1.48 V at lower pH values prior to the reduction in diiron core. We postulate that at lower pH values protonation at unbound thiolate leads to the protonated complex **1H** which is capable of accepting an electron at a more positive reduction potential; this is arguably the first step towards the catalytic proton reduction, i.e., the "C" in C[ECEC]. Previous studies have shown that an electron-rich diiron core maybe protonated to yield an Fe^{II}(μ-H)Fe^{II} bridging hydride.[114] Similarly, in complex **1**, the substituted iron has an increased electron density which we expect will take up a proton to yield a hydride-bound diiron core at lower pH values probably via a concerted electron/proton transfer pathway, however a pH dependent study is required to confirm this postulate. Computational studies have shown that complex **1H** has the capability to generate an asymmetric hydride localized on the iron with the bound NiN_2S_2 (**1HH**) where the H^+•••H^- distance of 2.03 Å is favorable for coupling (Figure III-17).

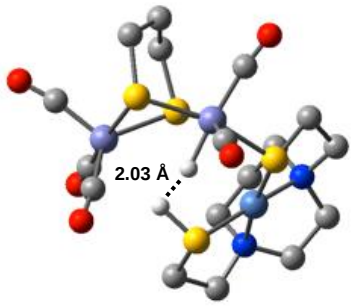

Figure III-17. Modeled structure for complex **1HH**.

Conclusion

The crucial aza-dithiolate linker in the active site of [FeFe]-H_2ase has inspired the development of synthetic analogues that utilize ligands which serve as conventional σ-donors with pendant base features for H^+ binding and delivery. Several MN_2S_2 complexes (M = Ni^{2+}, $[Fe(NO)]^{2+}$, $[Co(NO)]^{2+}$ etc.) utilize these cis-dithiolates to bind low valent metals and also demonstrate the useful property of hemi-lability, i.e., alternate between bi- and mono-dentate ligation. Synthetic efforts have led to the isolation and characterization of three hetero-trimetallics that employ metallodithiolate ligand binding to diiron scaffolds in three redox levels, (μ-pdt)$[Fe(CO)_3]_2$, (μ-pdt)$[Fe(CO)_3][(Fe(NO))^{II}(IMe)(CO)]^+$ and (μ-pdt)(μ-H)$[Fe^{II}(CO)_2(PMe_3)]_2^+$ to generate (μ-pdt)$[(Fe^{I}(CO)_3][Fe^{I}(CO)_2$•$NiN_2S_2]$ (**1**), (μ-pdt)$[\ Fe^{I}(CO)_3][\{Fe(NO)\}^{II}(IMe)$•$NiN_2S_2]^+$ (**2**) and (μ-pdt)(μ-H)$[Fe^{II}(CO)_2(PMe_3)][Fe^{II}(CO)(PMe_3)$•$NiN_2S_2]^+$ (**3**) complexes. These complexes display efficient metallodithiolate binding to the diiron scaffold with one thiolate-S which allows the free unbound thiolate to potentially serve as a built-in pendant base to direct proton binding, promoting a possible Fe-$H^{-\cdots+}$H-S coupling mechanism for the electrocatalytic hydrogen evolution reaction (HER) in the presence of acids.

CHAPTER IV

KINETICS PARAMETERS FOR LIGAND SUBSTITUTION ON (μ-pdt)[Fe(CO)$_3$][Fe(CO)$_2$NiN$_2$S$_2$] UNIT[#]

Introduction

Stereochemical nonrigidity of the sulfur to sulfur linker in the (μ-pdt)[Fe(CO)$_3$]$_2$ unit (pdt = propanedithiolate) has been discussed in the Chapter I and confirmed by Daresnbourg et al. via a series of variable-temperature ^{1}H and ^{13}C NMR studies.[113] In contrast, diiron hexacarbonyl units containing dithiolates that introduces significant bridgehead bulk such as (μ-*o*-xyldt)[Fe(CO)$_3$]$_2$ adopts a fixed geometry at the S-to-S linker even at a room temperature making the two iron atoms nonequivalent.[88] Similarly, the apical/basal site exchange phenomena of the Fe(CO)$_3$ moiety in (μ-SRS)[Fe(CO)$_3$]$_2$ units has also been studied extensively by Darensbourg et al.[30, 122] using variable-temperature ^{13}C NMR techniques. Extensive density functional theory calculations along with ^{13}C NMR evidence has found a lower rotational barrier at the Fe(CO)$_3$ for the (μ-*o*-xyldt)[Fe(CO)$_3$]$_2$ complex compared with the other similar complexes such as (μ-pdt)[Fe(CO)$_3$]$_2$ due to the relief of the excessive repulsive steric interactions between the bridgehead arene group of (μ-*o*-xyldt)[Fe(CO)$_3$]$_2$ and the apical CO ligand.[113]

[#]Major Parts of this chapter were reproduced with permission from (Kariyawasam Pathirana, K. D.; Ghosh, P.; Hsieh, C-H.; Elrod, L. C.; Bhuvanesh, N.; Darensbourg, D. J.; Darensbourg, M. Y., Synthetic Metallodithiolato Ligands as Pendant Bases in [Fe^{I}Fe^{I}], [Fe^{I}[Fe(NO)]^{II}], and [(μ-H)Fe^{II}Fe^{II}] Complexes. *Inorg. Chem*, **2020**, 59 (6), 3753-3763). Copyright **2020** American Chemical Society)

For the complex (μ-pdt)[Fe(CO)$_3$]$_2$, the density functional theory computations and NMR studies agree on an activation barrier of a 57.3 kJ/mol for the apical/basal CO-site exchange process.[30] Computations suggest a change in highest occupied molecular orbitals (HOMO) due to the changes in structural differences of ground state and transition state structures that occur during the CO-site exchange process. The optimized transition state does not contain a 60^o staggered Fe(CO)$_3$ unit as expected from a simple rotation of the eclipsed Fe(CO)$_3$ ground state.[30] Rather, during the rotation the CO unit that comes underneath the Fe–Fe vector adopts a slightly bend geometry along with the flattening of the rotated S$_2$Fe(CO)$_3$ unit (Figure IV-1).[30]

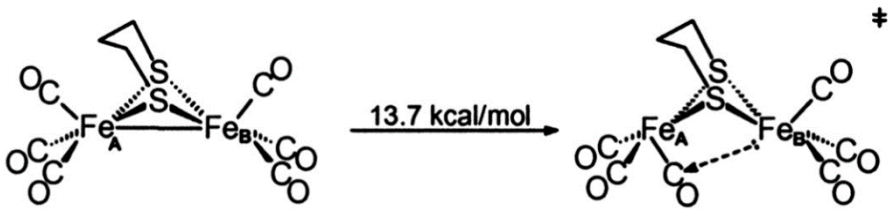

Figure IV-1. Polarization of Fe-Fe bond electron density upon Fe(CO)$_3$ unit rotation in (μ-pdt)[Fe(CO)$_3$]$_2$ (A - rotating Fe center, B - static Fe center)[30] (Reprinted with permission from (Darensbourg, M. Y.; Lyon, E. J.; Zhao, X.; Georgakaki, I, P., *PNAS* **2003**, 100 (7), 3683-3688). Copyright **2003** National Academy of Sciences, U.S.A.)

The transition state of the rotated (μ-pdt)[Fe(CO)$_3$]$_2$ can be viewed as having two square pyramidal Fe(CO)$_3$ units where one is inverted with respect to the other while the ground state contains two symmetrical edge-bridged square pyramids. The main differences of the transition state compared to the ground state can be identified as;

i. The partial disruption and the lengthening of the Fe–Fe bond.

ii. The polarization of bond density towards the unrotated iron.

iii. The polarized bond density being partially dispersed towards the rotated CO unit that lies underneath the Fe–Fe vector.

iv. The development of a charge disparity where the rotated $Fe(CO)_3$ unit is ~0.2 units more positive making it an apparent open site for an incoming ligand.

It has been postulated that the electron-donating ligands that have the potential of occupying the open site trans to the rotated CO unit can enhance the electron donation from the unrotated Fe_B to CO center creating a more stabilized intermediate. Detailed ligand substitution and kinetic studies using a CN^- as an incoming ligand by Darensbourg et al. have provided valuable insight to further understand the reactions of rotated $Fe(CO)_3$ centers.[87]

The CO/CN^- substitution process in $(\mu\text{-pdt})[Fe(CO)_3]_2$ yields the disubstituted $(\mu\text{-pdt})[Fe(CO)_2(CN)]_2^{2-}$ derivative (Figure IV-2) where two CN^- ligands get attached to both Fe centers in consecutive steps. Both steps follow associative (S_N2) type pathways (Eqn. IV-1-2).

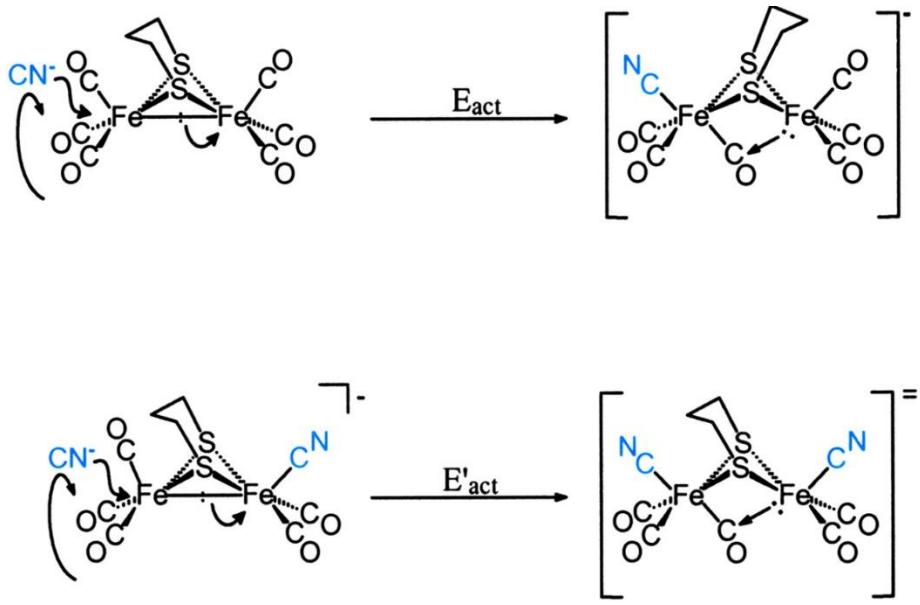

Figure IV-2. Proposed mechanism for the two-step CN^{-}/CO substitution reaction in (μ-pdt)$[Fe(CO)_3]_2$[30] (Reprinted with permission from (Darensbourg, M. Y.; Lyon, E. J.; Zhao, X.; Georgakaki, I, P., *PNAS* **2003**, 100 (7), 3683-3688). Copyright **2003** National Academy of Sciences, U.S.A.)

$$(\mu\text{-pdt})[Fe(CO)_3]_2 + Et_4N^+CN^- \xrightarrow{E_{act}} (\mu\text{-pdt})[Fe(CO)_3][Fe(CO)_2(CN)]^- \quad \textbf{[1]}$$

$$\text{rate} = k_2\{(\mu\text{-pdt})[Fe(CO)_3]_2\}[CN^-]$$

$$(\mu\text{-pdt})[Fe(CO)_3][Fe(CO)_2(CN)]^- + Et_4N^+CN^- \xrightarrow{E'_{act}} (\mu\text{-pdt})[Fe(CO)_2(CN)]_2^{2-} \quad \textbf{[2]}$$

$$\text{rate} = k_2\{(\mu\text{-pdt})[Fe(CO)_3][Fe(CO)_2(CN)]^-\}[CN^-]$$

Kinetic studies found that for complex (μ-pdt)[$Fe(CO)_3$]$_2$ E_{act} > E'_{act} which is unexpected since the nucleophilic attack of an anion on an anion is expected to create a larger activation energy barrier due to electrostatic repulsions. It is postulated that this unexpected result is due to a combination of two different processes (rotation and attack) that affect the overall activation energy. The overall activation energy, E_{act}(overall) can be modulated by both the activation energy required for the attack of the nucleophilic CN^- ligand, E_{act}(CN^- attack), and the activation energy required for the rotation of the $Fe(CO)_3$ unit, E_{act}(rot'n) (Eqn. IV-3).[30, 87]

$$E_{act}(\text{overall}) = E_{act}(CN^- \text{ attack}) + E_{act}(\text{rot'n}) \quad \textbf{[3]}$$

During the first CO/CN^- exchange the nucleophilic CN^- ligand attacks the $Fe(CO)_3$ unit which results in its rotation and placing one of its CO's underneath the Fe–Fe vector. The transition state thus is stabilized by the electron donation from the unrotated $Fe(CO)_3$ unit. During the second step, the CN^- attack experience a higher activation energy barrier, E_{act}(CN^- attack) due to the electrostatic repulsion of an anion attack on an anion. However, the second CN^- finds a significantly lower rotational barrier, E_{act}(rot'n) due to the presence of the already coordinated CN^- ligand, which increases the electron density on the substituted iron to a great extent to stabilize the rotated transition state. It is postulated that in the second step, the significant decrease in term E_{act}(rot'n) dominates the overall activation energy, E_{act}(overall) and leads to the unexpected result where E_{act} > E'_{act}.[30, 87]

For complex (μ-*o*-xyldt)[Fe(CO)$_3$]$_2$, kinetic studies found that $E_{act} < E'_{act}$. Here, there is an assist for rotation even for the first CN^- attack that arises from the repulsive attractions between the bridgehead arene and CO. This repulsive interaction significantly lowers the activation energy barrier for the rotation, E_{act}(rot'n) for both first and second steps. In this case the inherent difficulty for an anion to attack on an anion, the overall activation energy for the second step E'_{act}(overall) increases compared to the first step and a lower reaction rate for the second step is observed for the complex (μ-*o*-xyldt)[Fe(CO)$_3$]$_2$. Based on the density functional theory calculations by Hall et al., the extent of the bridging character of the rotated CO unit increases as the incoming nucleophile inserts into the open coordination position on the rotated iron.[88]

Kinetic studies on S-oxygenated (μ-pst)[Fe(CO)$_3$]$_2$ complex by Darensbourg et al. have demonstrated the effect of the sulfenato group on the fluxionality and reactivity of the diiron complex. The reaction of (μ-pst)[Fe(CO)$_3$]$_2$ with excess PMe_3 in toluene at $80C^0$ yielded (μ-pst)[Fe(CO)$_3$][Fe(CO)$_2$PMe$_3$].[87] However, the plot of k_{obs} vs [PMe_3] produce a linear plot with a non-zero intercept indicating that the reaction does not follow a strict second order rate expression, but rather both associative and dissociative processes are assumed to be involved. In contrast, the complex (μ-pdt)[Fe(CO)$_3$]$_2$ follows a strict second order condition where the plot of k_{obs} vs [PMe_3] shows a good linearity with a zero intercept (Figure IV-3).

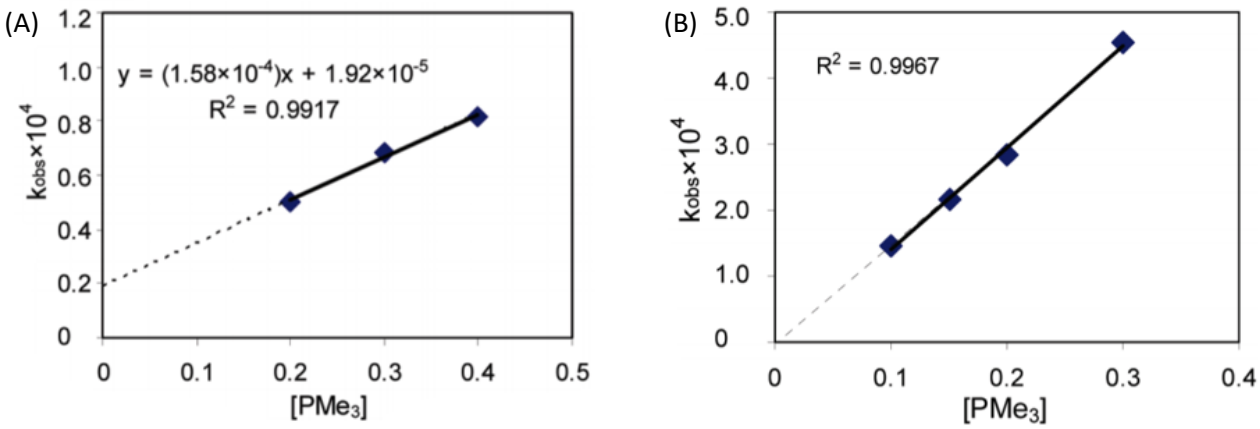

Figure IV-3. The plot of k_{obs} vs [PMe_3] for the reactions between (A) (μ-pst)[$Fe(CO)_3]_2$ and excess PMe_3 and (B) (μ-pdt)[$Fe(CO)_3]_2$ and excess PMe_3[87] (Reprinted with permission from (Bin, L.; Tianbiao, L.; Singleton, M. L.; Darensbourg, M. Y., *Inorg. Chem*, **2009**, 48 (17), 8393-8403). Copyright **2009** American Chemical Society)

For the reaction between (μ-pst)[$Fe(CO)_3]_2$ and PMe_3, a simple rate expression can be written in order to obtain both associative (k_2) and dissociative (k_1) rate constants (Eqn. 4).

$$\text{1-O + xs } PMe_3 \xrightarrow{\text{Toluene}} \text{1-O-}PMe_3 \text{ [4]}$$

$$\text{rate} = k_1[\text{1-O}] + k_2[\text{1-O}][PMe_3]$$

$$\text{rate} = k_{obs}[\text{1-O}];\ k_{obs} = k_1 + k_2[PMe_3]$$

The calculated E_{act}(overall) for the reaction between (μ-pst)[$Fe(CO)_3]_2$ and PMe_3 is 60 kJ/mol and the calculated E_{act}(overall) for the reaction between (μ-pdt)[$Fe(CO)_3]_2$ and PMe_3 is 48 kJ/mol.[87] These experimental results were consistent with the DFT calculations and suggested sluggish reactions of nucleophiles with sulfur oxygenated (μ-pst)[$Fe(CO)_3]_2$

compared to the analogous thiolato complexes. It has been postulated that in (μ-pst)[$Fe(CO)_3$]$_2$ complex, the presence of oxygen makes the Fe center more electrophilic and makes it harder to stabilize the CO unit that lies underneath the Fe–Fe vector in the transition state. Thus, the greater barrier to structural deformation in (μ-pst)[$Fe(CO)_3$]$_2$ inhibits its ability to undergo the CO/PMe_3 substitution compared to the (μ-pdt)[$Fe(CO)_3$]$_2$, resulting slower reaction rates and higher activation energy barriers.[87]

This chapter will mainly focus on the reactions between (μ-pdt)[$Fe(CO)_3$][$Fe(CO)_2$•NiN_2S_2] (**1**). Mechanistic studies will assess the Fe–S bond strength in all three complexes, (μ-pdt)[$Fe^{I}(CO)_3$][$Fe^{I}(CO)_2$•NiN_2S_2] (**1**), (μ-pdt)[$Fe^{I}(CO)_3$][{Fe(NO)}^{II}(IMe)•NiN_2S_2]$^{+}BF_4^{-}$ (**2**) and (μ-pdt)(μ-H)[$Fe^{II}(CO)_2(PMe_3)$][$Fe^{II}(CO)(PMe_3)$•NiN_2S_2] $^{+}PF_6^{-}$ (**3**). Furthermore, based on the experimental data, different ligand substitution pathways (associative vs dissociative) will also be addressed.

Reactivity Studies Directed towards Evaluating FeFe—S_2N_2Ni Bond Strengths

In order to rank the Fe-S bond lability in the three FeFe complexes in different oxidation states of iron and bearing NiN_2S_2 metalloligands, complexes **1**, **2**, and **3** in CH_2Cl_2 solvent and at 25 °C were exposed to a 20-fold excess of PMe_3 (Eqn. IV-5, 6 and 7). Under these conditions, displacement of the NiN_2S_2 metalloligand in complex **1** yielding (μ-pdt)[$Fe(CO)_3$][$Fe(CO)_2PMe_3$], (**1-PMe_3**), was complete within 15 min, complex **2** more slowly converts to the PMe_3 analogue, requiring ≤2 h; and complex **3** shows no reaction whatsoever over the course of 3 h.

Complex **1** + PMe_3 ⟶ (μ-pdt)[($Fe^{I}(CO)_3$][$Fe^{I}(CO)_2PMe_3$] (**5**)

Complex **2** + PMe_3 ⟶ (μ-pdt)[$Fe^{I}(CO)_3$][{Fe(NO)}^{II}(IMe)(PMe_3)]$^{+}BF_4^-$ (**6**)

Complex **3** + PMe_3 ⟶ (μ-pdt)(μ-H)[$Fe^{II}(CO)_2(PMe_3)$][$Fe^{II}(CO)(PMe_3)_2$]$^{+}PF_6^-$ (**7**)

Figure IV-4. demonstrates the IR characterization of the products from reaction (**5**) after initially tracking the reaction using UV-Vis spectroscopy which confirmed the formation of (μ-pdt)[($Fe^{I}(CO)_3$][$Fe^{I}(CO)_2PMe_3$]. Hence, the disappearance of respective absorbances of complexes **1**, **2** and **3** in the UV-Vis spectra were used to monitor the reactions (Figure IV-5) and mass spectrometry was used to identify both initial and final products (Figure IV-6).

Based on the data from Figure IV-5, a simplistic relationship of the qualitative results of NiN_2S_2 ligand displacement is with the expected electrostatic contribution to the Fe—S bonds in the metallodithiolate ligand: $Fe^{I}Fe^{I}$- S_2N_2Ni < $Fe^{I}Fe^{II}$- S_2N_2Ni < < $Fe^{II}Fe^{II}$- S_2N_2Ni. This correlation is assuming positive character of the NO-substituted Fe in complex **2** following addition of NO^+, thus generating the Enemark-Feltham $\{Fe(NO)\}^7$ unit as the NO^+ withdraws sufficient electron density from Fe^{I}, effectively generating $Fe^{II}(NO)^{\bullet}$.

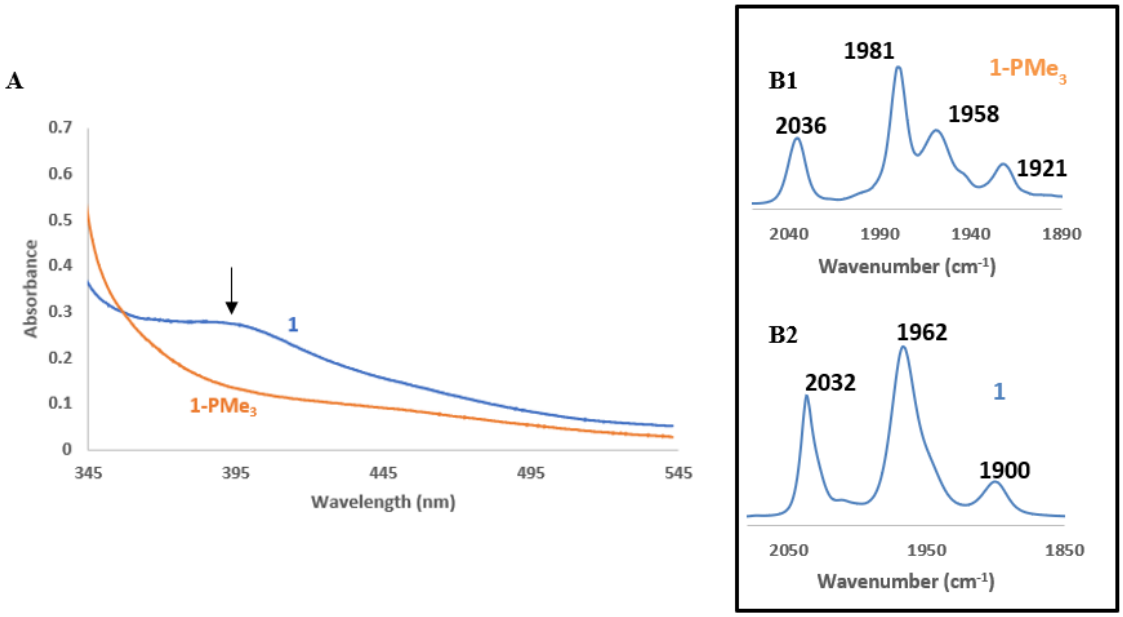

Figure IV-4. IR characterization of products after UV-Vis kinetics for complex **1** in DCM. (**A**) UV-Vis spectrum of reacting **1** with 20-fold excess PMe_3 (**B1**) IR spectrum of products inside the cuvette after reacting **1** with 20-fold excess PMe_3. (**B2**) IR spectrum of the starting material **1** in cuvette before injecting 20-fold excess PMe_3.

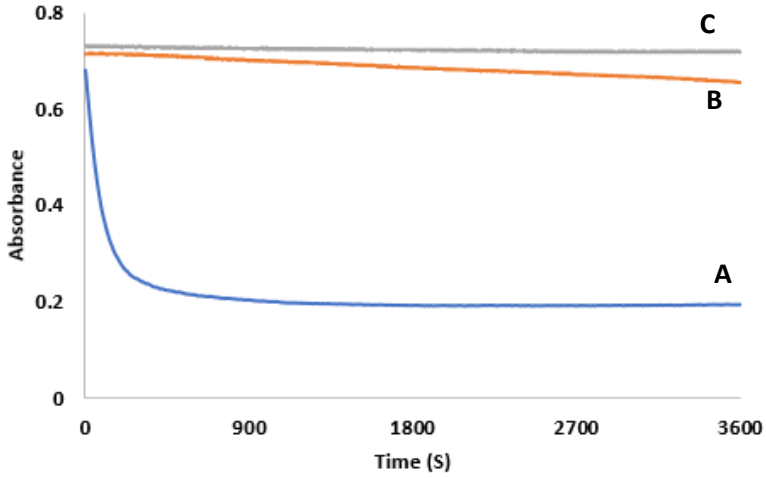

Figure IV-5. (**A**) Disappearance of peak at 393 nm for complex **1**. (**B**) 360 nm for complex **2**. (**C**) 446 nm for complex **3** in DCM.

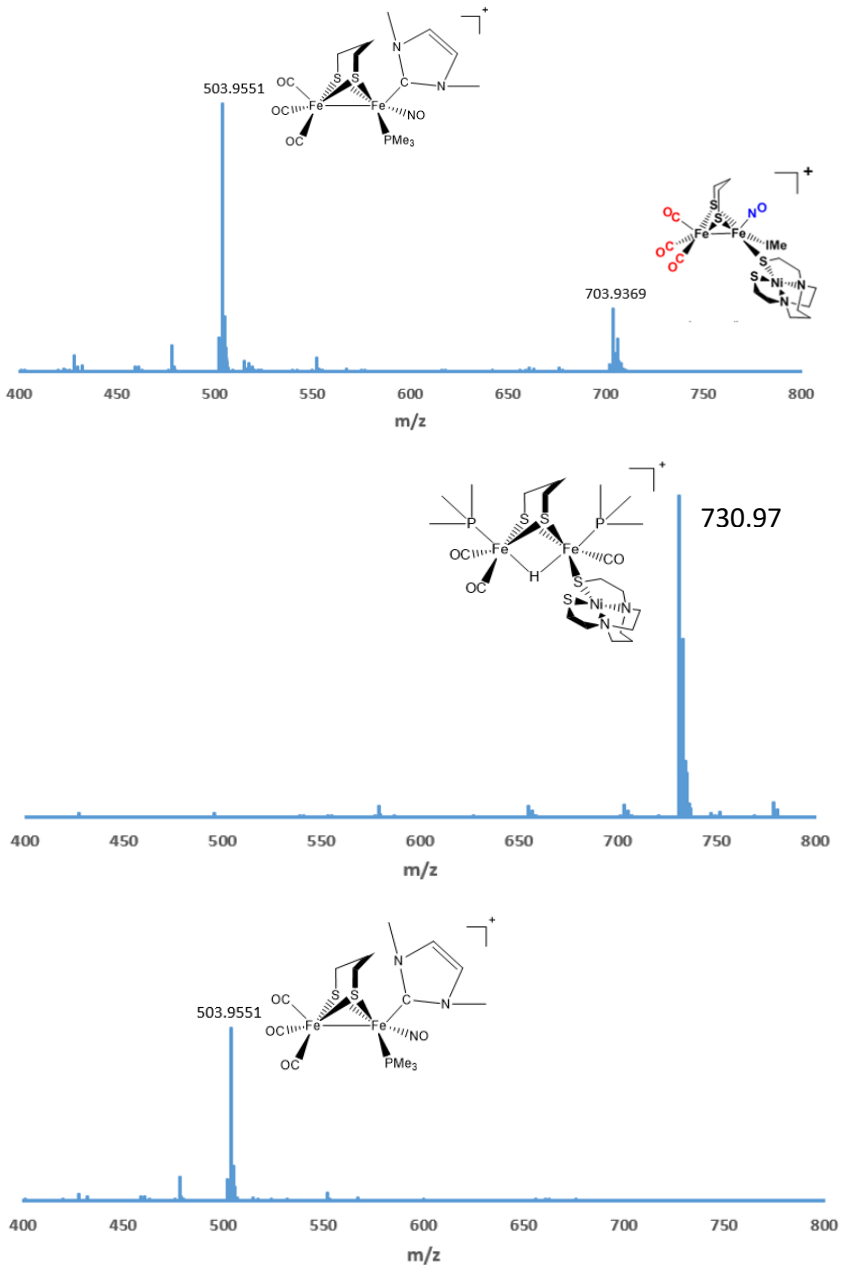

Figure IV-6. **(A)** ESI+ mass spectrum for the reaction between **2** and PMe_3 after 1hr in DCM. **(C)** ESI+ mass spectrum for the reaction between **2** and PMe_3 after 2hrs in DCM. **(C)** ESI+ mass spectrum for the reaction between **3** and PMe_3 after 3hrs in DCM

However, the steric encumbrance from the NHC ligand in complex **2** is also a factor as expressed in the longest Fe-S bond distance found, while the all-CO derivative, complex **1**, generates the shortest distance. The conundrum of steric vs. electronic control thus encouraged further study.

Rates of NiN_2S_2 / PMe_3 ligand exchange in complex 1.

Kinetic parameters for the reactions of 1 with PMe_3 were monitored by IR and UV-Vis spectroscopies. For IR measurements, disappearance of the ν(CO) band at 1962 cm^{-1} with time was monitored and for UV-Vis measurements, disappearance of the absorbance at 393 nm which corresponds to **1** was used, Figure IV-7.

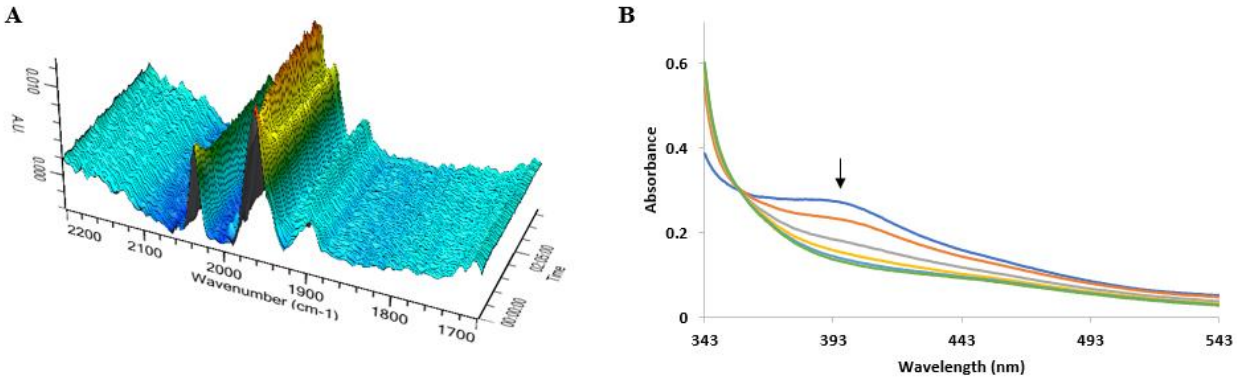

Figure IV-7. (a) Infrared spectra of 5 mM solution of **1** in DCM with 20-fold excess of PMe_3, in the 1800-2100 cm^{-1} region, as NiN_2S_2/PMe_3 exchange takes place to produce the complex **1-PMe_3**. (b) UV-Vis spectra, of converting 0.3 mM solution of complex **1** (initial: blue trace) to **1-PMe_3** (final: green trace) in DCM.

In-situ IR spectroscopy was initially used to identify the reactants and products. Due to the smaller requirement of sample concentration and faster spectral acquisition rates, UV-Vis spectroscopy was used for the determination of rates as a function of temperature. The

plots of $\ln(A_0/A_t)$ versus time showed good linearity as seen in Figure IV-8B. The derived values of k_{obs} at various PMe_3 concentrations and reaction temperatures, as determined by UV-Vis spectroscopy, are given in Table IV-1, entries 1-12. Each k_{obs} was obtained from a single kinetic run, with at least ~100 spectral accumulations per run. The plot of k_{obs} versus [PMe_3], Figure IV-8A, shows linearity; however, a non-zero intercept indicates the reaction does not follow a strict second-order rate expression, but rather both associative (A) and dissociative (D) substitution processes are assumed to be involved, **Eqn. IV-8,9**.

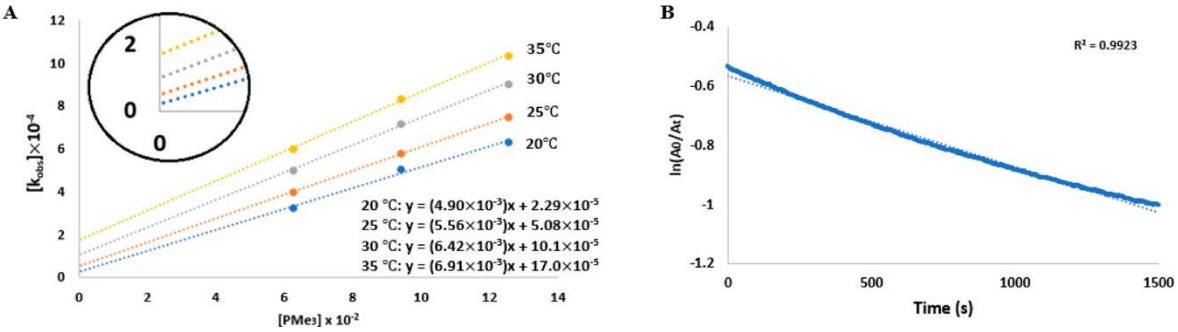

Figure IV-8. (a), Plots of k_{obs} vs [PMe_3] for the formation of **1-PMe3** from **1** measured at 20/25/30/35 ℃ (Conditions: **Table IV-1, Entry 1-12**). (b) Example plot of $\ln(A_0/A_t)$ vs time over four half-lives (Conditions: **Table IV-1, Entry 1**).

Table IV-1. Rate data for the reaction of PMe_3 with 1 at 20/25/30/35 ℃ in DCM using UV-Vis

Entry	Temp (℃)	$[PMe_3]$ x 10^2M	k_{obs} x 10^4	Rate Constant
1	20	6.27	3.213	
2	20	9.41	5.021	k_2 = 4.90 x 10-3 $M^{-1}s^{-1}$ k_1 = 2.29 x 10-5 s^{-1}
3	20	12.54	6.288	
4	25	6.27	3.975	
5	25	9.41	5.770	$k_2 = 5.56 \times 10^{-3}$ $M^{-1}s^{-1}$ $k_1 = 5.08 \times 10^{-5}$ s^{-1}
6	25	12.54	7.461	
7	30	6.27	4.985	
8	30	9.41	7.158	$k_2 = 6.42 \times 10^{-3}$ $M^{-1}s^{-1}$ $k_1 = 1.01 \times 10^{-4}$ s^{-1}
9	30	12.54	9.015	
10	35	6.27	5.992	
11	35	9.41	8.318	$k_2 = 6.91 \times 10^{-3}$ $M^{-1}s^{-1}$ $k_1 = 1.70 \times 10^{-4}$ s^{-1}
12	35	12.54	10.32	

[1] = 3.1 x 10^{-4} M with 20-40-fold excess PMe_3

Hence, the plot of k_{obs} versus $[PMe_3]$ at 20℃, Figure IV-8A and **Eqn. IV-9**, yields the dissociative substitution rate constant, $k_1 = 2.29\times10^{-5}$ sec^{-1}, derived from the intercept and the rate constant for the associative path is obtained from the slope, $k_2 = 4.90\times10^{-3}$ $M^{-1}sec^{-1}$.

$$\text{Rate} = k_1[1] + k_2[1][PMe_3] \qquad (8)$$

$$\text{Rate} = k_{obs}[1];\ k_{obs} = k_1 + k_2[PMe_3] \qquad (9)$$

The same reaction was monitored using in-situ IR spectroscopy at -40 ℃. The plot of k_{obs} vs $[PMe_3]$ obtained from this data also resulted in a linear plot with non-zero intercept

(Table IV-2, entries 1-3, Figure IV-9), confirming that the rate expression contains both associative and dissociative components. It should be noted that the IR and UV-Vis traces represent a stoichiometric reaction and reproducibility is on the order of 95%.

Table IV-2. Rate data for the reaction of PMe3 with **1** at -40°C in DCM using IR

Entry	[PMe_3] x 10^2 M	k_{obs}^{IR} x 10^4 (-40°C), sec^{-1}	Rate Constant (-40°C)
1	9.44	6.50	
2	14.17	8.85	k_2 = 6.61 x 10-3 $M^{-1}s^{-1}$
3	18.89	12.74	k_1 = 2.40 x 10-7 s^{-1}

[1] = 4.72×10-3 M with 20-40-fold excess PMe_3.

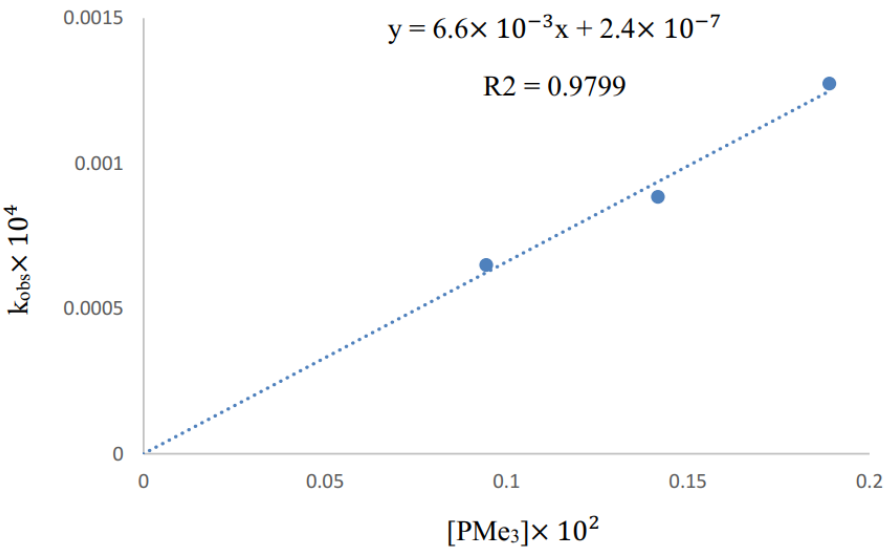

Figure IV-9. Plot of k_{obs} vs [PMe3] for the formation of 1-PMe_3 at -40°C

The temperature dependence of rate constants for both A and D pathways for the formation of complex **1-PMe3** from **1** obtained by UV-Vis are given in Table IV-3 and presented graphically as Eyring plots, Figure IV-10. Extrapolation of Eyring plots led to a calculated value of $k_2 = 7.88\times10^{-3}$ $M^{-1}sec^{-1}$ and $k_1 = 1.31\times10^{-7}$ sec^{-1} at -40 ℃. These calculated values match the experimentally determined values for k_2 and k_1 at -40 ℃ using the in-situ IR spectroscopic monitor within an acceptable margin further confirming the accuracy of the method.

Table IV-3. Temperature dependence of reaction of PMe_3 with **1**.

Reaction path	T, °C	*k*	Activation parameters[b]
		10^{-3} k_2, $M^{-1}s^{-1}$	
1 ⟶ 1-PMe_3[a] (A Path)	20	4.90	E_a = 17 kJ/mol
	25	5.56	$\Delta H^{\ddagger}$ = 15 (±1) kJ/mol
	30	6.42	$\Delta S^{\ddagger}$ = -237 (±5) J/mol.K
	35	6.91	
		10^{-4} k_1, s^{-1}	
1 ⟶ 1-PMe_3[a] (D Path)	20	0.23	Ea = 101 kJ/mol
	25	0.51	$\Delta H^{\ddagger}$ = 98 (±5) kJ/mol
	30	1.01	$\Delta S^{\ddagger}$ = 3 (±17) J/mol.K
	35	1.70	

[a][a] = 3.1 x 10^{-4} M; [PMe_3] = 0.0627 - 0.1254 M. [b]Errors in activation parameters reported at 95% confidence level.

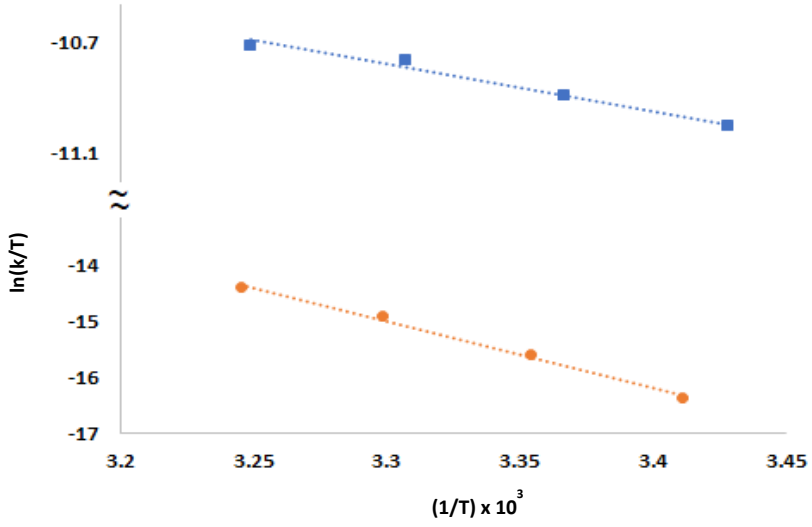

Figure IV-10. Eyring plots for the formation of complex 1-PMe_3 from associative (■) and dissociative (•) path.

Conclusions

Calculated values for the enthalpy and entropy of activation are listed in Table IV-3. The small values of $\Delta H^{\ddagger}$ (15 ($\pm$1) kJ/mol) and large negative values for $\Delta S^{\ddagger}$ (-237 ($\pm$5) J/mol•K) are consistent with the associative pathway. **Eqn. IV-10** describes the PMe_3/CO substitution reaction of a monosubstituted phosphine complex affording a disubstituted phosphine complex.

$$(\mu\text{-pdt})[Fe^{I}(CO)_3][Fe^{I}(CO)_2PMe_3] + PMe_3 \xrightarrow{E_{act}} (\mu\text{-pdt})[Fe(CO)_2(PMe_3)]_2 \quad (10)$$

This reaction was previously reported to follow a similar associative pathway; however, the reported activation energy barrier for the CO displacement reaction is higher compared to the PMe_3 substitution reaction of NiN_2S_2 in **1**. This is possibly due to the fact that the NiN_2S_2 ligand, according to the *ν*(CO) IR data, is a better electron donor compared to PMe_3. The proposed mechanism for such reactions (**Scheme 2**) specifies that E_{act}(overall) is composed of two contributory factors: E_{act}(attack) and E_{act}(rot'n). Accepting this analysis, we conclude that during the associative pathway, PMe_3 attacks the more electrophilic $[Fe(CO)_3]$ center leading to shift one of its CO's underneath the Fe-Fe vector (rotation of the $Fe(CO)_3$ unit) where it is stabilized by the electron-rich side to create the transition state (**Scheme 2**). Due to the assist from the $[Fe(CO)_2\bullet NiN_2S_2]$ center to stabilize the rotated transition state, the contribution from E_{act}(rot'n) becomes significantly smaller thereby lowering the E_{act}(overall) compared to the reaction described by **Eqn. 6**.

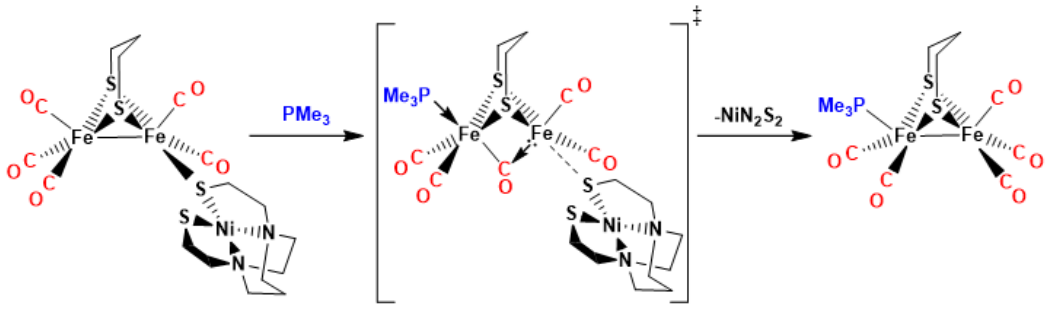

Scheme 2. Proposed mechanism for the associative path.

Large values of $\Delta H^{\ddagger}$ and positive values for $\Delta S^{\ddagger}$ are hallmarks for dissociative pathways. The dissociative path for the reaction between **1** and PMe_3 yields a $\Delta H^{\ddagger}$ value of 98 kJ/mol, possibly due to the detachment of NiN_2S_2 ligand from diiron core which is preparatory to the transition state which permits the attachment of the incoming PMe_3 ligand (**Scheme 3**). Thus, we conclude that for complex **1** the Fe-S bond energy is ca. 98 kJ/mol.

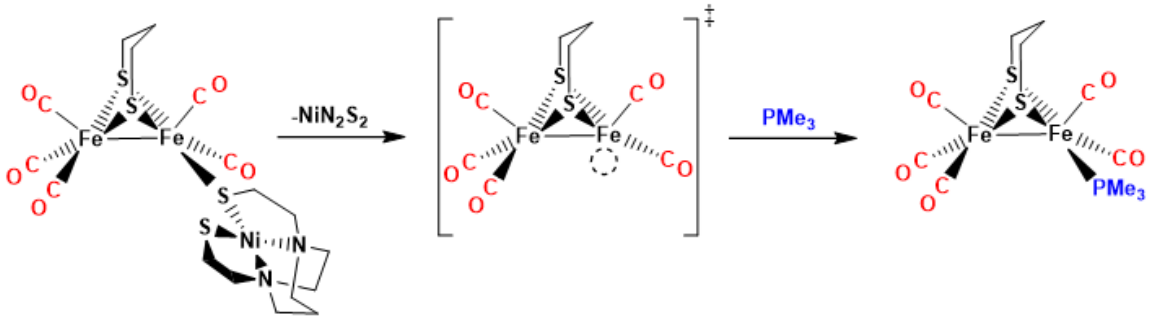

Scheme 3. The dissociative path for PMe_3/NiN_2S_2 exchange.

CHAPTER V

INTER/INTRA – MOLECULAR NITROSYL LIGAND EXCHANGE IN DIIRON TRINITROSYL COMPLEXES

Introduction

Over the past two decades, hundreds of diiron carbonyl complexes capable of electrocatalytic hydrogen production have been synthesized that mimics the 2Fe subunit within the 6Fe cluster in [FeFe]-H_2ase. Most of these complexes feature diatomic CO/CN^- ligands and a butterfly-shaped 2Fe2S core with a metal-metal bond distance of *ca.* 2.5 Å, maintained by a bridging dithiolate.[123] Such geometric arrangement allows these complexes to perform two-electron catalytic functions by sharing required redox changes. In the active site of [FeFe]-H_2ase, the redox active 4Fe4S cluster that connects to the 2Fe2S subunit via a cysteinyl sulfur acts as an electron shuttle, injecting needed electrons for proton reduction which leads to an extraordinary hydrogen producing capability. However, efforts to create similar systems with exogeneous redox active sites have not been very successful due to their low stability and low activity.

The challenging task of designing proton reduction catalysts with a redox flexibility in terms of delocalization in storage, speciation on demand by a proton and charge capacity has been addressed by Darensbourg *et al.* by combining metallodithiolato ligands with a second iron unit containing nitrosyl ligands, creating a novel diiron trinitrosyl complex, $[(NO)Fe(N_2S_2)Fe(NO)_2]^{+/0}$ (**1**$^+$ and **1**^{0}).[123-124] These diiron trinitrosyl complexes have demonstrated to be stable in both oxidized and reduced states with a significant activity towards proton reduction in electrocatalytic environments. Nitric oxide is well known for

exhibiting strong covalent properties when bound to transition metals similar to CO/CN^- and PR_3 ligands. Recent studies by Darensbourg *et al*. have demonstrated a significant impact on the oxidation state of the iron center due to this covalency of the bound nitrosyl ligands. Molecular structures of the oxidized $[(NO)Fe(N_2S_2)Fe(NO)_2]^+$ (**1**$^+$) and reduced $[(NO)Fe(N_2S_2)Fe(NO)_2]^0$ (**1**^{0}) have demonstrated that the accommodation of redox level changes in these systems involves both irons and the electron buffering, redox non-innocent NO ligands (Figure V-1).[124] Due to their remarkable ability to regulate electronic density and added protons within a stable diiron unit, these diiron trinitrosyl complexes offer a novel pathway to design efficient biomimetic hydrogenase active site models.

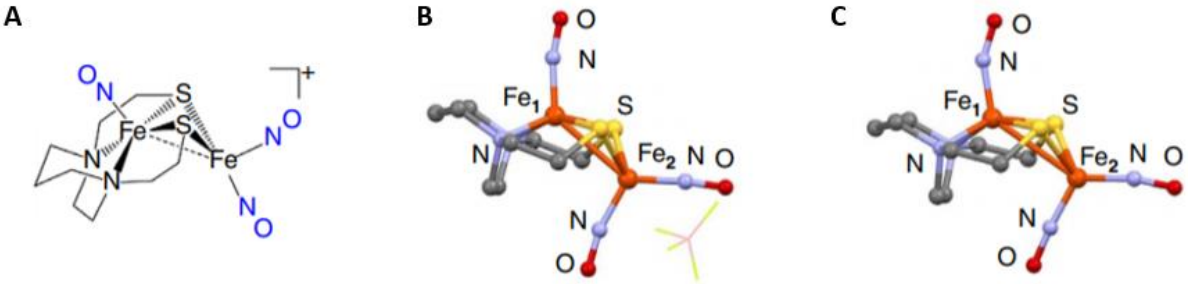

Figure V-1. A. Redox active diiron trinitrosyl complex $[(NO)Fe(N_2S_2)Fe(NO)_2]^+$ (**1**$^+$) B. Crystal structure of the oxidized $[(NO)Fe(N_2S_2)Fe(NO)_2]^+$ (**1**$^+$) C. Crystal structure of reduced $[(NO)Fe(N_2S_2)Fe(NO)_2]^0$ (**1**^{0})[123] (Reprinted with permission from (Hsieh, C-H.; Ding, S.; Erdem, Ö. F.; Crouthers, D. J.; Liu, T.; McCrory, C. C. L.; Lubitz, W.; Popescu, C. V.; Reibenspies, J. H.; Hall, M. B.; Darensbourg, M. Y., *Nat. Commun*. **2014**, 5, 3684). Copyright **2014** Nature Publishing Group, a division of Macmillan Publishers Limited)

Complex $[(NO)Fe(N_2S_2)Fe(NO)_2]^+$ displays a remarkable ability to accommodate an added electron with a subtle changes in its geometry that emphasize the interdependence of the electronic/structural changes between oxidized and reduced forms. EPR and DFT studies are interpreted by electronic assignment of the oxidized form to be antiferromagnetically coupled $\{Fe(NO)\}^7 \cdot \{Fe(NO)_2\}^9$, and $\{Fe(NO)\}^7 \cdot \{Fe(NO)_2\}^{10}$ for the reduced form. Upon reduction of $[(NO)Fe(N_2S_2)Fe(NO)_2]^+$, the added electron locates itself on the dinitrosyl iron

unit. However, due to the electron buffering capability of nitrosyl ligands, both sides adjust to the additional negative charge, further evidenced by the minor geometrical rearrangements. Studies have found that the reduced complex $[(NO)Fe(N_2S_2)Fe(NO)_2]^0$ reacts with stronger acids to generate H_2 (Figure V-2).[123]

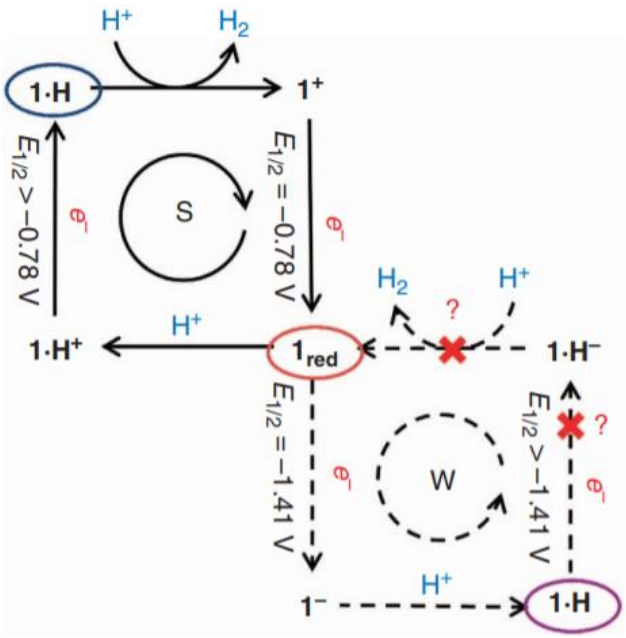

Figure V-2. The catalytic cycle of **1** (solid line and symbol 'S') in the strong acid is complete. The catalytic cycle in the weak acid (dashed line and symbol 'W') is incomplete, presumably due to cyclic reactivity that leads to decomposition. (Reprinted with permission from (Hsieh, C-H.; Ding, S.; Erdem, Ö. F.; Crouthers, D. J.; Liu, T.; McCrory, C. C. L.; Lubitz, W.; Popescu, C. V.; Reibenspies, J. H.; Hall, M. B.; Darensbourg, M. Y., *Nat. Commun*. **2014**, 5, 3684). Copyright **2014** Nature Publishing Group, a division of Macmillan Publishers Limited)

The isolated reduced complex shows a redox event at -0.78 V whose current response increases linearly with the addition of a strong acid HBF_4.[123] It has been postulated that this event corresponds to the addition of an electron to the **1-H** complex which can react with protons in the solution to generate hydrogen. Overall, studies have confirmed the potential

of $[(NO)Fe(N_2S_2)Fe(NO)_2]^{+/0}$ system to act as an electrocatalyst with a turnover number of a 1.5 and a turnover frequency of a 0.38 h^{-1}.[123]

The works of prominent chemists like Darensbourg, Lehnert and Layfield have significantly contributed to understand structural and electronic properties of diiron trinitrosyl systems.[123-124] However, more experimentation is still required to fully understand these complexes in order to employ them as efficient electrocatalysts for hydrogen production or as NO releasing agents. An unexplored possibility of such systems is their potential for inter/intra nitrosyl scrambling. Even though the evidence on inter/intra NO scrambling is rare on literature, several studies have shown the possibility for bridging NO units to exist in diiron systems, providing evidence for potential intermediate states in NO-scrambling processes.

Flavodiiron nitric oxide reductase (FNORs) is a unique enzyme that helps some pathogens in the environment to mitigate nitrosative stress. These FNORs are capable of reducing NO to generate N_2O leading to pathogenic proliferation.[125-131] Since these enzymes have a significant impact in bacterial pathogenesis, microbiologists are increasingly interested in understanding the FNOR mechanisms in order to find new ways to combat bacterial infections. FNORs can be found in nature in a wide array of microorganisms. In 2002, Gardner *et. al.* discovered a type of FNOR expressed in *E. coli* as a defense mechanism for NO exposure.[132] More recent studies by Kurtz *et. al*. and Rodrigues-Pousada *et. al.* have discovered some members of FprA family of FNORs in *Desulfovibrio vulgaris* and *Desulfivibrio gigas*.[133] Crystallographic studies have suggested that the active site FNORs contains a non-heme diiron core with two central iron atoms with coordinated histidine and carboxylate ligands. Furthermore, in most cases two irons are bridged by a water/hydroxide

and a carboxylate ligand (Figure V-3) providing a five-coordinate iron with an open sixth coordination site for NO binding.

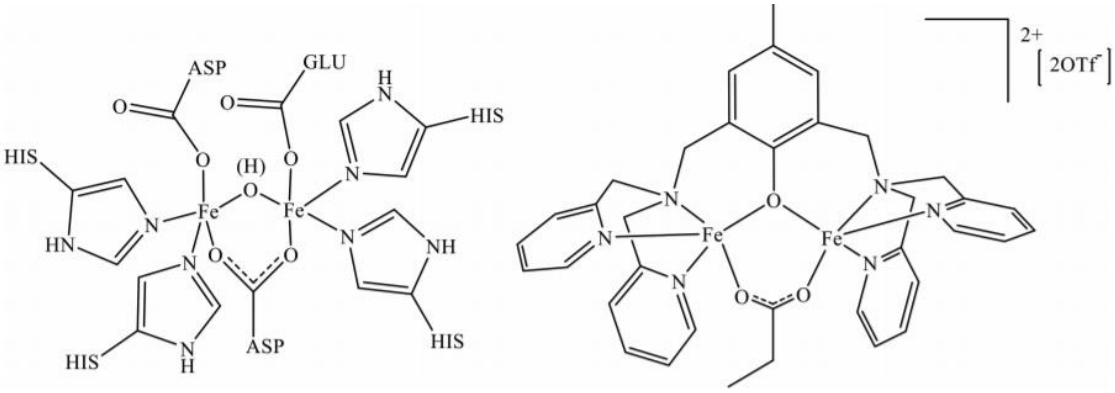

Figure V-3. ChemDraw representation of the FNOR *M. Thermoacetica* active site (left) and a model complex of the active site (right) by Lehnert *et. al.*[127] (Reprinted with permission from (Dong, H. T.; White, C. J.; Zhang, B.; Krebs, C.; Lehnert, N., *J. Am. Chem. Soc.* **2018**, 140 (41), 13429-13440). Copyright **2018** American Chemical Society)

Over the years, several pathways have been proposed for N-N coupling and subsequent NO activation in FNOR active sites. Studies by Kurtz *et. al.* on the FNOR active sites of *T. maritima* have demonstrated that a diiron dinitrosyl unit plays an important role in N-N coupling and N_2O generation.[134] According to their studies, NO ligands bind to adjacent iron centers creating a $[\{FeNO\}^7]_2$ complex. The monoiron $\{FeNO\}^7$ unit has a total spin of S = 3/2 due to the antiferromagnetic coupling of high spin Fe(III) and triplet NO^- and the two high spin $\{FeNO\}^7$ centers are antiferromagnetically coupled to generate the $[\{FeNO\}^7]_2$ complex with a total spin of S = 0. Three main pathways have been proposed for the N-N coupling in $[\{FeNO\}^7]_2$ FNOR active sites, a direct coupling path, a superreduced path and a semireduced path as shown in Figure V-4.

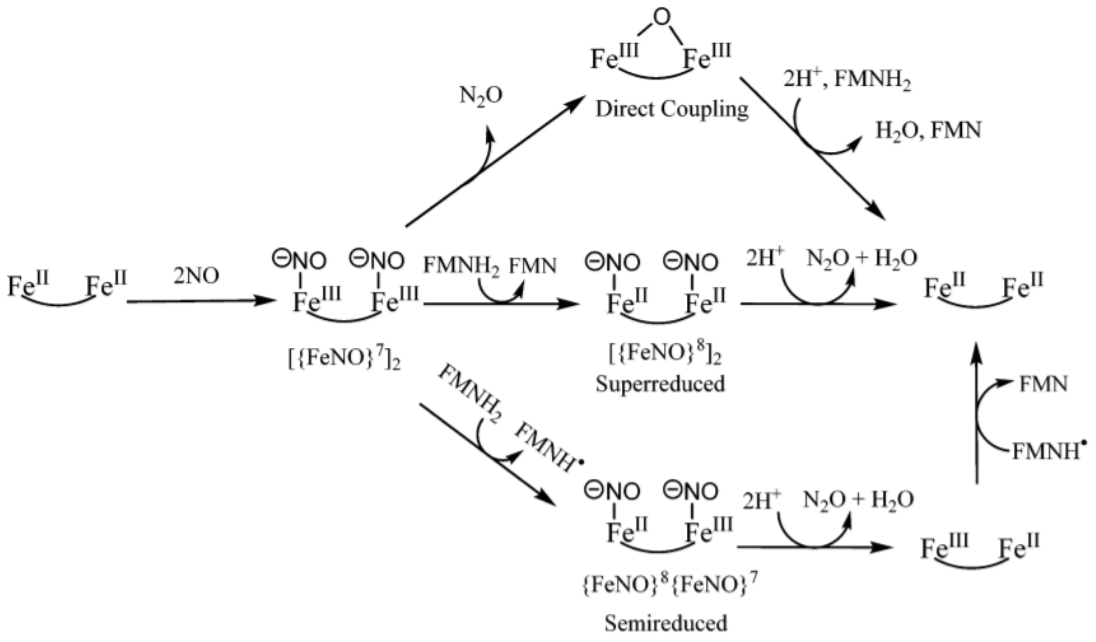

Figure V-4. Proposed mechanisms for the N-N coupling in $[\{FeNO\}^7]_2$ FNOR active sites.[127] (Reprinted with permission from (Dong, H. T.; White, C. J.; Zhang, B.; Krebs, C.; Lehnert, N., *J. Am. Chem. Soc.* **2018**, 140 (41), 13429-13440). Copyright **2018** American Chemical Society)

In the direct coupling pathway two NOs on adjacent irons come together due to their close proximity in order to generate N_2O. In contrast, the superreduced and semireduced pathways involves addition of two or one electrons respectively to the diiron core generating $Fe^{II}Fe^{II}$ or $Fe^{II}Fe^{III}$ intermediate configurations. Studies by Lehnert *et al*. and Lippard *et. al*. have found that $\{FeNO\}^7$ model complexes are stable in solutions due to the covalent nature of the Fe-NO bond. Therefore, it is believed that the assistance from an external reductant like $FMNH_2$ can lead to the weakening of Fe-NO bond to efficiently generate N_2O.[126-127] Such mechanistic studies have provided evidence to rationalize the interaction of adjacent NO ligands in diiron units to either release N_2O or to potential inter/intra molecular NO exchange processes.

The coordination chemistry of non-heme iron with NO ligands is still an elusive subject to chemists. A recent effort by Lehnert *et. al*. to isolate a unique $Fe_2(NO)_2$ diamond core structural motif has provided further evidence to demonstrate the ability of adjacent NO ligands in a diiron core to interact with both irons.[99] Even though the high-spin diiron dinitrosyl model complexes of FNORs have demonstrated the ability to undergo N-N coupling and subsequent N_2O release via reduction or direct coupling, only a few mononuclear non-heme iron nitrosyl complexes have shown the ability to generate N_2O upon reduction. However, in most cases the reduction of mononuclear non-heme iron nitrosyls results in disproportionation leading to the formation of dinitrosyl iron complexes (DNIC) (**Eq. V-1**)

$$2\ \{FeNO\}^7 + 2\ e^- \longrightarrow 2\ \{FeNO\}^8 \longrightarrow \{Fe(NO)_2\}^{10} + Fe^{II} \quad \textbf{(Eq. V-1)}$$

The mechanism of generating DNICs via the reduction of simple non-heme mononuclear iron systems is not well understood and remains an interesting area of study due to the importance of $\{Fe(NO)_2\}^{9/10}$ DNICs in mammalian physiology as an important source of NO. Furthermore, DNICs with histidine ligands have the potential to make the important diiron core during in ferric uptake regulation proteins in ferritin and serum albumin.[99] Clearly the understanding the reactivity of such DNICs can have a significant biological importance. However, some DNICs ($\{FeNO\}^8$) are highly unstable and harder to isolate, making it difficult for further analysis. However, in a recent study Lehnert *et. al.* were able to study a $\{FeNO\}^8$ unit within a TPA (tris(2-pyridylmethyl)amine) ligand and subsequently isolate a $Fe_2(NO)_2$ diamond core structure, which is unprecedented in non-heme iron nitrosyl chemistry.

Upon reduction of the compound [Fe(TPA)(NO)(OTf)](OTf) (Figure V-5A) with one equivalent of $CoCP_2$ in CH_2Cl, Lehnert et. al. were able to observe quick color change of the complex to orange from its original color black.[99] UV-Vis and IR data suggested a complete conversion of the initial complex and surprisingly no new bands were observed at approximately 2200 cm^{-1} which can be an evidence for the forming of N_2O and the mass spectrometry suggested a still intact NO ligand in the reduced product. To determine the exact nature of the reduced product Lehnert *et. al.* were able to isolate it in crystal form and according to X-ray crystal evidence, the reduced complex is in a dimeric form with a two $\{FeNO\}^8$ units bridged by two NO molecules with a molecular formula of $[Fe_2(TPA)_2(NO)_2](OTf)_2$ (Figure V-5B).

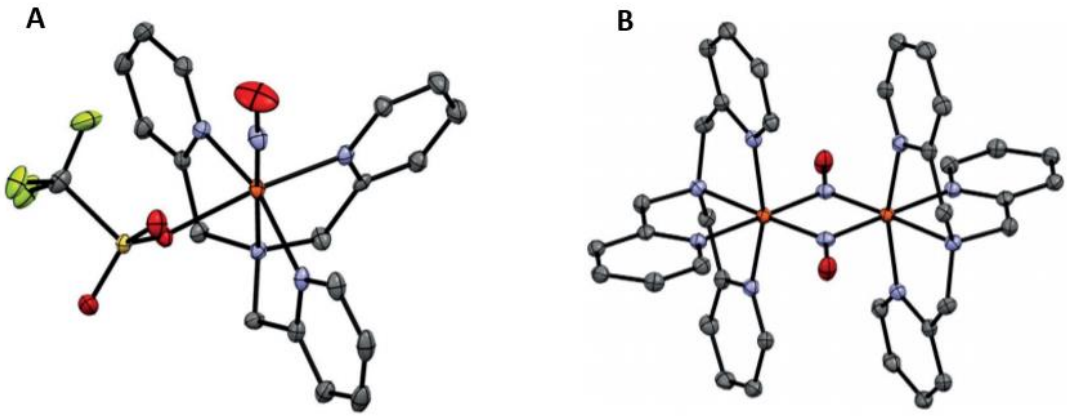

Figure V-5. Crystal structure of the complexes (**A**) [Fe(TPA)(NO)(OTf)](OTf) and **(B)** $[Fe_2(TPA)_2(NO)_2](OTf)_2$[99] (Reprinted with permission from (Dong, H. T.; Speelman, A. L.; Kozemchak, C. E.; Sil, D.; Lehnert, N., *Angew. Chem. Int. Ed.* **2019**, 58 (49), 17695-17699). Copyright **2019** John Wiley and Sons)

These studies demonstrate the possibility of adjoining NO ligands in a diiron core to interact with both irons without emitting N_2O as was the case of FNORs. Hence, it seems reasonable to raise the question about the possibility of intramolecular site exchange of NO ligands in similar environments.

The complex $[(NO)(FeN_2S_2)]Fe(NO)_2]$ contains two irons with bound NO ligands in both and the preliminary mass spectrometry data using a labeled ^{15}NO in the mono nitrosyl unit suggests that in a solution, potential NO scrambling can occur within the molecule as well as between the molecules resulting complexes that contains more than one labeled ^{15}NO ligands. Hence, this chapter will mainly focus on studying the inter/intra NO scrambling process in diiron trinitrosyl complexes.

Spectroscopic evidence of ^{15}NO in $[Fe(NO)(N_2S_2)][Fe(NO)_2]$ complexes

Infrared spectroscopy measures the energy of vibrational absorptions when the sample is irradiated with infrared radiation. It is an important tool that can be used to investigate isotopic effects in organometallic complexes. Using the simple harmonic oscillator approximation, a bond between two atoms can be approximated as a spring connecting two masses. The energy of oscillation is directly proportional to $\sqrt{k/m}$ where k is the force constant (the stiffness of the spring) and m is the reduced mass. Therefore, inserting a heavier isotope to components of a bond can increase the reduced mass of the vibrating unit and decrease the energy required, shifting the bands in an IR spectrum to a lower wavenumber. When the frequency of IR radiation matches the vibrational frequency of a bond, it can be absorbed and, according to the selection rules of IR spectroscopy, any vibration that registers a change in molecular dipole moment will be detected as a unique event.

The unlabeled diiron trinitrosyl complex $[(^{14}NO)(FeN_2S_2)][Fe(^{14}NO)_2]$ shows three absorptions in the IR spectrum at 1809 cm^{-1}, 1770 cm^{-1} and 1745 cm^{-1}. Upon substituting all the ^{14}NO units with heavier ^{15}NO, all three bands in the spectrum shift ~34 cm^{-1} towards the lower wavenumbers resulting in three bands at 1772 cm^{-1}, 1735 cm^{-1} and 1710 cm^{-1} (Figure V-6). These values match the calculated values for the all ^{15}NO complex.

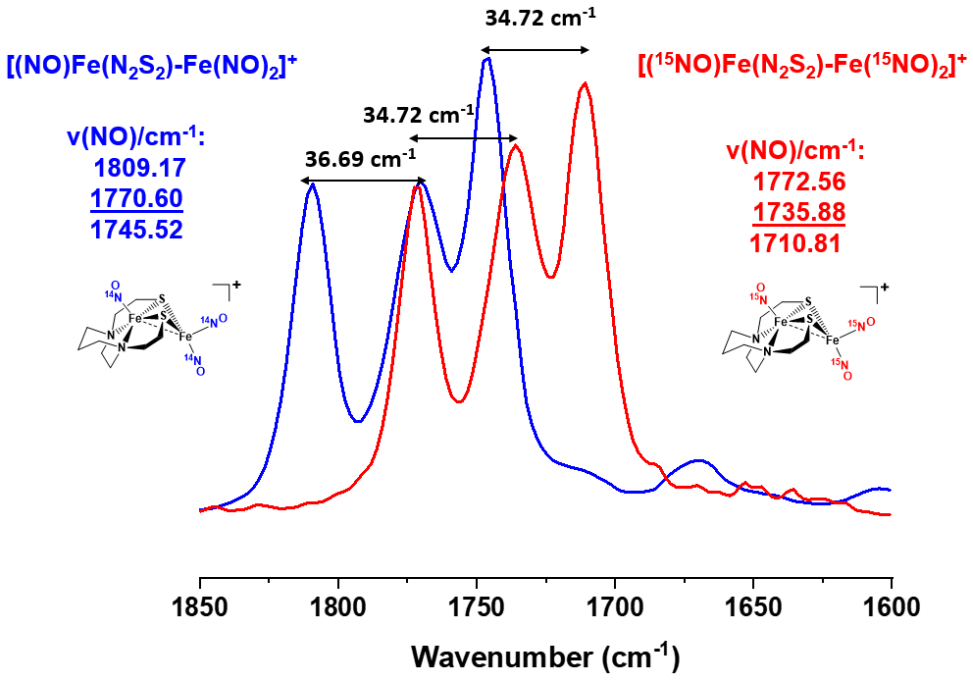

Figure V-6. FTIR spectrum of $[(^{14}NO)(FeN_2S_2)][Fe(^{14}NO)_2]$ (blue) and $[(^{15}NO)(FeN_2S_2)][Fe(^{15}NO)_2]$ in DCM at room temperature.

To understand the effects of NO vibrations on the IR spectrum, Hall *et al.* conducted a computational study to calculate the contribution of different NO vibrational modes on the bands of the IR spectrum. According to the calculations, the symmetric stretch of the NO ligands on both mononitrosyl and dinitrosyl units give rise to the band at 1809 cm^{-1} where the majority intensity contribution is from the dinitrosyl unit. The band at 1770 cm^{-1} is due

to the asymmetric stretch of a single NO ligand in the dinitrosyl unit and a NO ligand in the mononitrosyl unit; the band at 1745 cm^{-1} is mainly due to the asymmetric stretch of NO ligands in the dinitrosyl unit. Upon replacing the ^{14}NO in the mononitrosyl unit with a ^{15}NO, the IR spectrum changes its shape from a three-band pattern to a two-band pattern where two bands appear at 1806 cm^{-1} and 1738 cm^{-1} (Figure V-7) and the change in band pattern can be explained using the calculations by Hall *et al.*

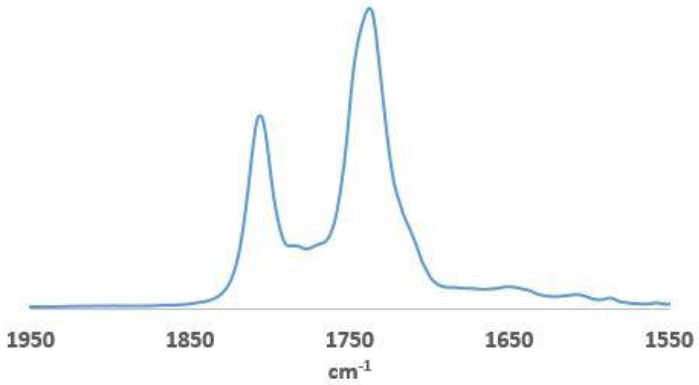

Figure V-7. FTIR spectrum of $[(^{15}NO)(FeN_2S_2)][Fe(^{14}NO)_2]$ in DCM at -10 ℃

The only contribution to the 1745 cm^{-1} band of $[(^{14}NO)(FeN_2S_2)][Fe(^{14}NO)_2]$ is from the two NO ligands on the dinitrosyl iron unit, hence replacement of ^{14}NO with ^{15}NO in the mononitrosyl side tends to have a minimal effect on the position of this absorption. However, the 1770 cm^{-1} band of $[(^{14}NO)(FeN_2S_2)][Fe(^{14}NO)_2]$ has contributions from NO ligands in both mononitrosyl and dinitrosyl units and replacing the ^{14}NO in the mononitrosyl unit with a ^{15}NO is expected to shift this band to lower wavenumbers by ~34 cm^{-1} giving a new absorption that overlaps with the band at 1745 cm^{-1}. Therefore, the broader band at 1738 cm^{-1} in complex $[(^{15}NO)(FeN_2S_2)][Fe(^{14}NO)_2]$ is a result of two overlapping absorptionss, the band at 1745 cm^{-1} which does not have any isotopic effect and the band at 1770 cm^{-1} which is shifted to lower wavenumbers as a result of the ^{15}NO isotope labeling. The 1806 cm^{-1}

absorption of $[(^{14}NO)(FeN_2S_2)][Fe(^{14}NO)_2]$ shows no change upon the substituting the mononitrosyl unit with ^{15}NO to generate $[(^{15}NO)(FeN_2S_2)][Fe(^{14}NO)_2]$. This is because the major contribution to 1806 cm^{-1} band arises from the symmetric stretch of the two ^{14}NO ligands in the dinitrosyl iron unit.

Substituting the ^{14}NO in the mononitrosyl iron unit to generate $[(^{15}NO)(FeN_2S_2)][Fe(^{14}NO)_2]$ with a unique IR spectrum provides an opportunity to study the inter/intra NO scrambling processes. Since the 1806 cm^{-1} band of $[(^{15}NO)(FeN_2S_2)][Fe(^{14}NO)_2]$ is mainly due to the symmetric stretch of the ^{14}NO ligands in dinitrosyl iron unit, any ^{15}NO substitution at this dinitrosyl iron center is expected to create a novel band that is shifted ~34cm^{-1} towards lower wavenumbers while lowering the height of band at1806 cm^{-1}.

During a strict intramolecular process, the labeled ^{15}NO ligand in the mononitrosyl iron unit can reside in three different positions (Figure V-8). Assuming all these arrangements are equally probable, there is $^2/_3$ of a statistical probability for the ^{15}NO to exist on the dinitrosyl iron unit and $^1/_3$ of a statistical probability for the ^{15}NO to exist on the mononitrosyl iron unit. Based on this argument, a couple of hypotheses can be constructed,

i. The band at 1806 cm^{-1} will not completely disappear during an intramolecular NO exchange event since there is a ~ $^1/_3$ chance for the ^{15}NO to exist on the mononitrosyl iron unit.

ii. During an intramolecular NO scrambling event, the 1806 cm^{-1} band height will go down ~ $^2/_3$ since the occupation of ^{15}NO at any position of the dinitrosyl iron unit will generate a new band at lower wavenumbers.

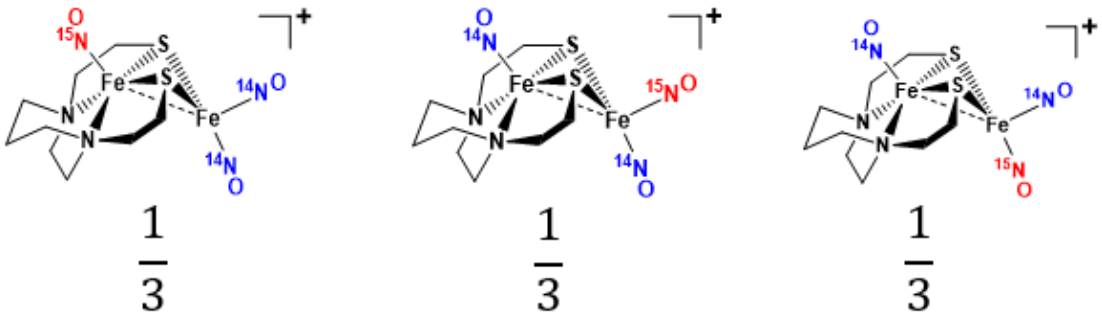

Figure V-8. Statistically probable ^{15}NO orientations in $[(^{15}NO)(FeN_2S_2)][Fe(^{14}NO)_2]$ complex.

The preliminary data obtained by mass spectrometry on $[(^{15}NO)(FeN_2S_2)][Fe(^{14}NO)_2]$ complex suggest that both inter- and intra-molecular scrambling occur in DCM at room temperature. The experimental mass spectrum of the complex $[(^{15}NO)(FeN_2S_2)][Fe(^{14}NO)_2]^+$ is shown in Figure V-9A, and it shows a significant deviation from the calculated mass spectrum with unexpected signals at 419.95, 421.94 and 422.94 m/z values.

These absorptions are posited to be generated from diiron trinitrosyl units that does not contain ^{15}NO or more than a single ^{15}NO within the system and the expected mass spectra for such complexes are shown in Figure V-9 B,C,D,E. Based on the mass spectroscopic evidence, we postulate that at room temperature, NO ligand exchange within and between diiron trinitrosyl molecules. This conclusion has inspired our investigation into inter/intra-molecular NO exchange. Such inter/intra-molecular NO exchange within/between the dinitrosyl iron units can lead to several products with labeled/unlabeled NOs as shown in Figure V-10.

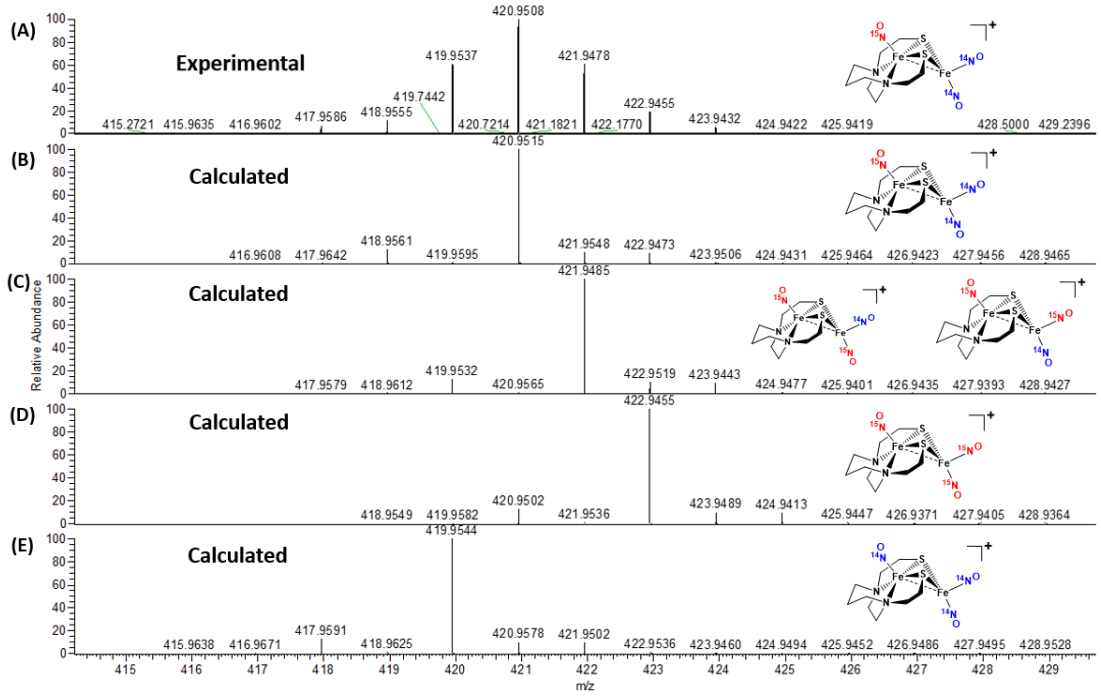

Figure V-9A. Experimental mass spectrum for complex $[(^{15}NO)(FeN_2S_2)][Fe(^{14}NO)_2]$ dissolved in DCM at room temperature for 1 hr. (**B**). Calculated mass spectrum for complex $[(^{15}NO)(FeN_2S_2)][Fe(^{14}NO)_2]$. (**C**) Calculated mass spectrum for complex $[(^{15}NO)(FeN_2S_2)][Fe(^{14}NO)(^{15}NO)]$. (**D**) Calculated mass spectrum for complex $[(^{15}NO)(FeN_2S_2)][Fe(^{15}NO)_2]$. (**E**) Calculated mass spectrum for complex $[(^{15}NO)(FeN_2S_2)][Fe(^{15}NO)_2]$.

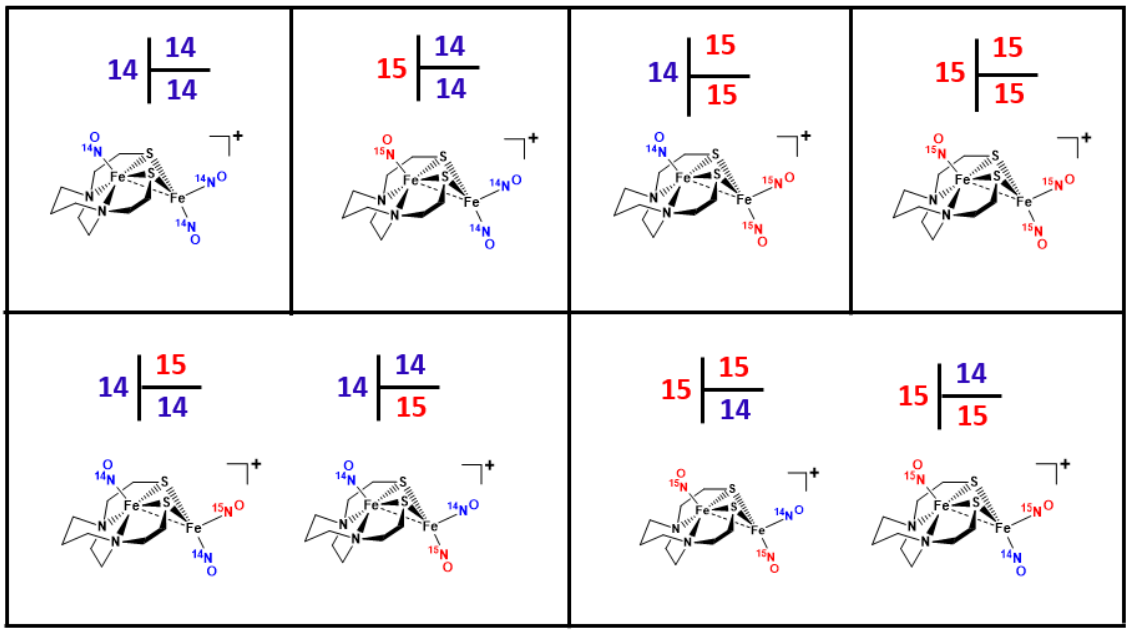

Figure 10-V. Possible arrangements of NO in diiron trinitrosyl complex mixtures due to inter/intra-molecular NO exchange

In-situ IR observations of complex [(^{15}NO)(FeN$_2$S$_2$)][Fe(^{14}NO)$_2$]

In-situ IR was used to study the variations of the IR absorptions of [(^{15}NO)(FeN$_2$S$_2$)][Fe(^{14}NO)$_2$] complex over time. At -10℃ in DCM, [(^{15}NO)(FeN$_2$S$_2$)][Fe(^{14}NO)$_2$] shows two bands at 1806 cm^{-1} and 1738 cm^{-1}. When increasing the temperature from -10℃ to -5℃, the bands at 1806 cm^{-1} and 1738 cm^{-1} start to decrease in intensity while developing a new broad shoulder band at 1730 cm^{-1} as well as several new absorptions within the 1806 cm^{-1} and 1738 cm^{-1} region (Figure V-11).

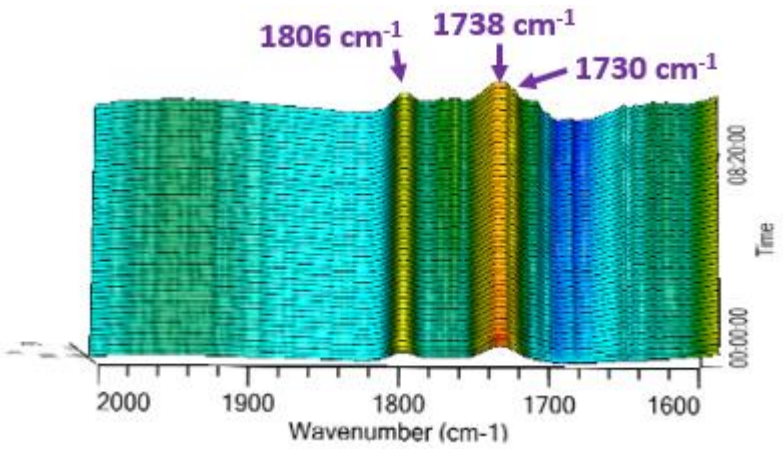

Figure V-11. in-situ IR profile of complex $[(^{15}NO)(FeN_2S_2)][Fe(^{14}NO)_2]$ in DCM depicting the absorptions at 1806 cm^{-1}, 1738 cm^{-1} and 1730 cm^{-1}.

The in-situ IR observations were confirmed using the FTIR where IR spectra were obtained in DCM at -10℃ and at room temperature. At -10℃ the IR spectrum shows two bands at 1806 cm^{-1} and 1738 cm^{-1}, upon warming up to room temperature the bands at 1806cm^{-1} and 1738 cm^{-1} lowers their band height while generating new band at 1732 cm^{-1} and within the 1806-1738 cm^{-1} region. (Figure V-12).

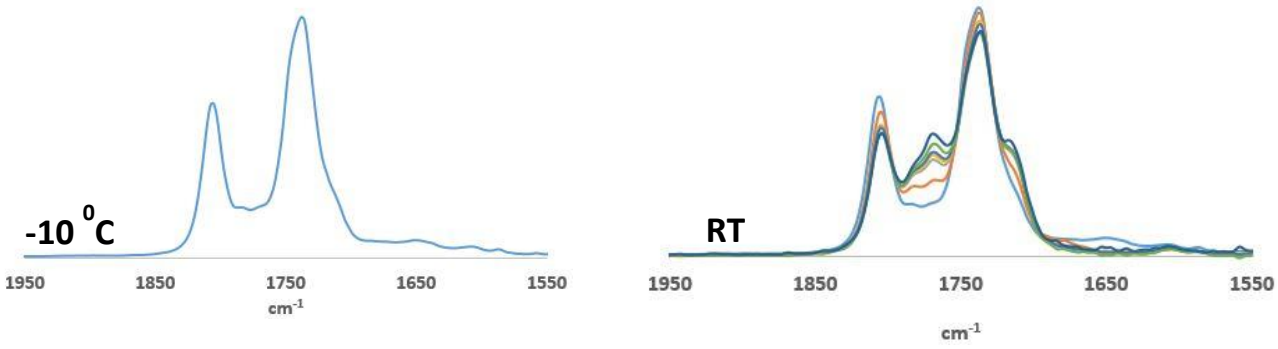

Figure V-12. FTIR spectrum of complex $[(^{15}NO)(FeN_2S_2)][Fe(^{14}NO)_2]$ in DCM at -10℃ (left) and the FTIR spectra of complex $[(^{15}NO)(FeN_2S_2)][Fe(^{14}NO)_2]$ in DCM at room temperature over 24 hrs.

To study the kinetics of inter/intra-molecular NO scrambling reactions, the change in band height vs time for band at 1806 cm^{-1} was observed using in-situ IR. It was hypothesized that during an intramolecular process, the band at 1806 cm^{-1} should go down $^2/_3$ of its original height. Since the band at 1806 cm^{-1} will not disappear completely, it is important to observe the in-situ IR plot for a prolonged time until it reaches an equilibrium distribution of labeled nitrosyls. In order to minimize the effects of evaporation during longer experiments, acetonitrile was used as a solvent since it has a higher boiling point compared to DCM.

An intramolecular NO exchange process will involve shifting of a NO ligand within the $[(^{15}NO)(FeN_2S_2)][Fe(^{14}NO)_2]$ molecule with a low activation energy barrier while an intermolecular process requires two $[(^{15}NO)(FeN_2S_2)][Fe(^{14}NO)_2]$ molecules to come together to initiate a transfer of NO ligands between molecules which will likely require a higher activation energy. Therefore, we hypothesized that low temperatures will favor intramolecular processes with first order kinetics and higher temperatures will favor both inter/intra-molecular processes.

Investigating intramolecular NO exchange in $[(^{15}NO)(FeN_2S_2)][Fe(^{14}NO)_2]$ complex at 5 ℃.

The intramolecular process was studied by monitoring the change of band height vs time for band at 1806 cm^{-1} in acetonitrile at 5 ℃ for 8 hours. During this time, the 1806 cm^{-1} band demonstrated a steady decrease in its band height with time as can be seen in Figure V-13 (A). The change of band height vs time is shown in Figure V-13 (B) and the plots of $\ln(A_0-A_t)$ vs time and $1/(A_0-A_t)$ vs time are shown in Figures V-13 (C) and (D). The plots of

$\ln(A_0-A_t)$ versus time showed good linearity with R^2 values of 0.9459. The derived value of k at 5 ℃ is 7.2×10^{-6} s^{-1}. This value was obtained from a single kinetic run, with at least ~100 spectral accumulations per run. The plot of $1/(A_0-A_t)$ vs time for a second order process failed to produce a linear correlation. This result indicates that at lower temperatures, an intramolecular NO exchange event that involves a single $[(^{15}NO)(FeN_2S_2)][Fe(^{14}NO)_2]$ molecule is more prominent compared to an intermolecular process that requires two $[(^{15}NO)(FeN_2S_2)][Fe(^{14}NO)_2]$ molecules. Therefore, at lower temperatures, a simple rate expression can be constructed where the complex $[(^{15}NO)(FeN_2S_2)][Fe(^{14}NO)_2]$ has a first order dependence with the overall rate (**Eqn. V-2**).

$$\text{Rate} = k_{avg}\,[(N_2S_2)Fe(^{15}NO)Fe(^{14}NO)_2]^1 \qquad \textbf{(2)}$$

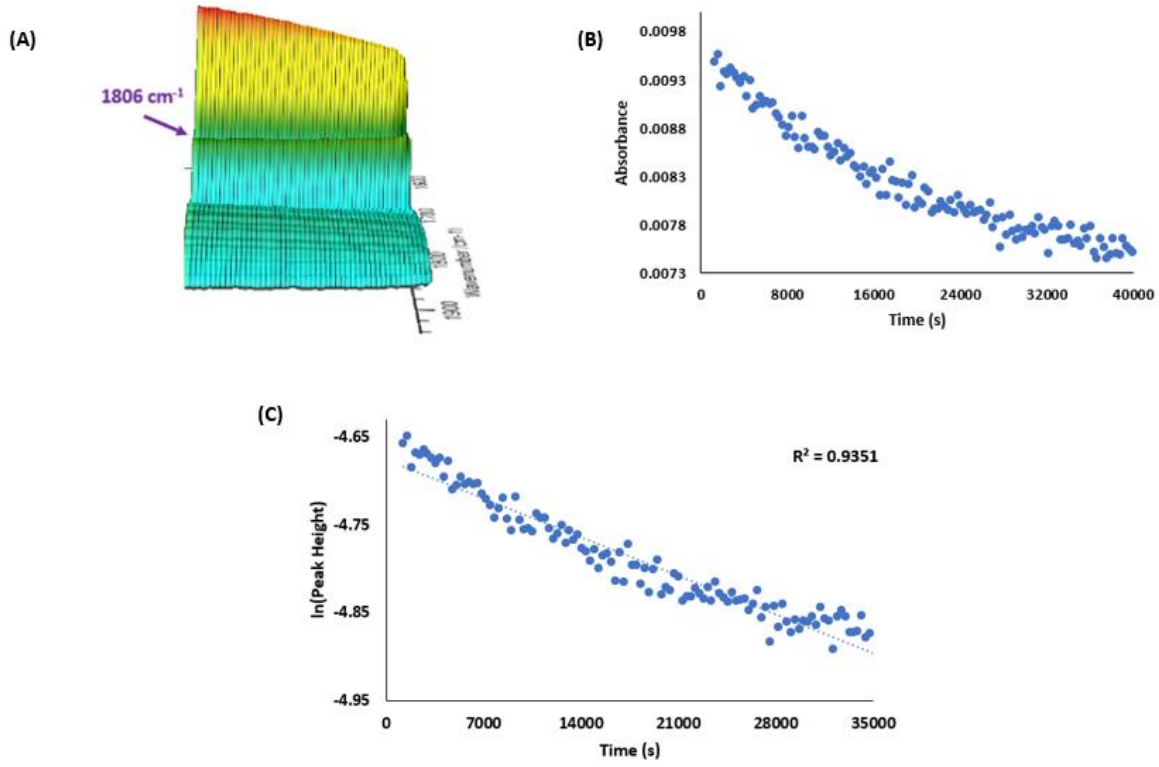

Figure V-13. (A) in-situ IR plot of complex $[(^{15}NO)(FeN_2S_2)][Fe(^{14}NO)_2]$ at 5 ℃ in MeCN **(B)** plot of band height change vs time for 1806 cm^{-1} band of complex $[(^{15}NO)(FeN_2S_2)][Fe(^{14}NO)_2]$ **(C)** plot of $\ln(A_0-A_t)$ vs time for band at 1806 cm^{-1}

Investigating intramolecular NO exchange in $[(^{15}NO)(FeN_2S_2)][Fe(^{14}NO)_2]$ complex at 15 ℃

The NO scrambling process at 15 ℃ was studied by monitoring the change of band height vs time for band at 1806 cm^{-1} in acetonitrile for 8 hours. During this time, the 1806 cm^{-1} band demonstrated a steady decrease in its band height with time as can be seen in Figure V-14 (A). The change of band height vs time is shown in Figure V-14 (B) and the plots of $\ln(A_0-A_t)$ vs time and $1/(A_0-A_t)$ vs time are shown in Figure V-14 (C) and (D). The

plot of ln(A_0-A_t) versus time and the plot of 1/(A_0-A_t) vs time showed some linearity with R^2 values of 0.7832 and 0.7576.

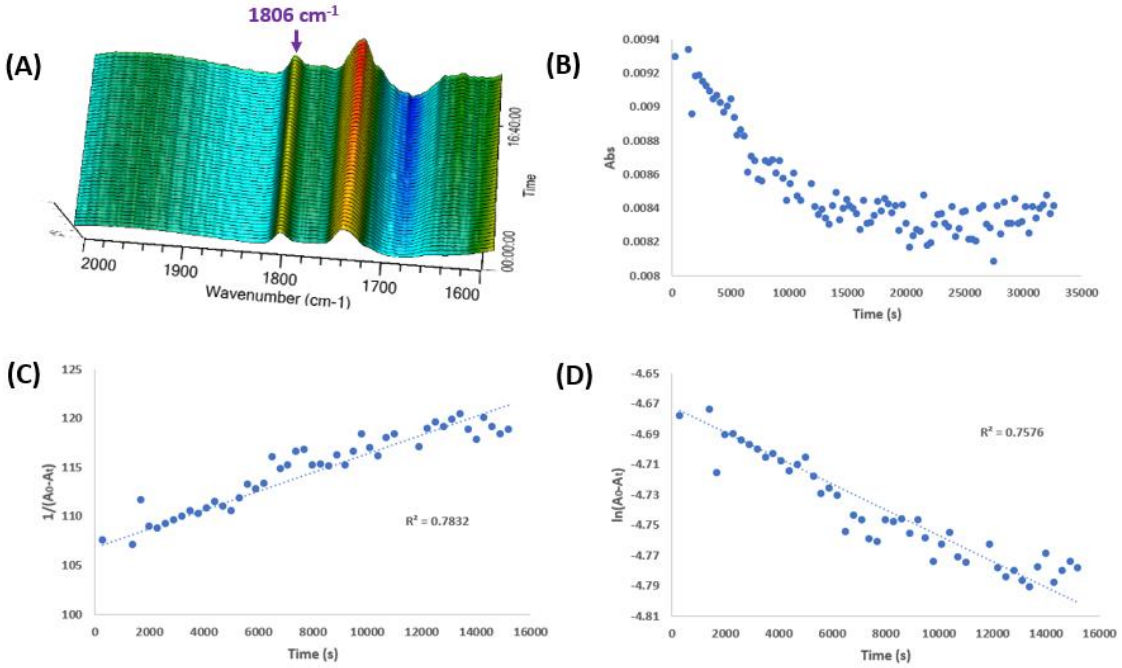

Figure V-14. (A) in-situ IR plot of complex [(^{15}NO)(FeN_2S_2)][Fe(^{14}NO)$_2$] at 15 ℃ in MeCN **(B)** plot of band height change vs time for 1806 cm^{-1} band of complex [(^{15}NO)(FeN_2S_2)][Fe(^{14}NO)$_2$] **(C)** plot of ln(A_0-A_t) vs time for band at 1806 cm^{-1} **(D)** plot of 1/(A_0-A_t) vs time for band at 1806 cm^{-1}

Investigating intramolecular NO exchange in [(^{15}NO)(FeN$_2$S$_2$)][Fe(^{14}NO)$_2$] complex at 25 ℃

The same process was studied by monitoring the change of band height vs time for the absorption at 1806 cm^{-1} in acetonitrile at 25 ℃ for 4 hours. During this time, the 1806 cm^{-1} band demonstrate a steady decrease in its band height with time and can be seen in Figure V-15 (A). The change of band height vs time is shown in Figure V-15 (B) and the plots of ln(A_0-A_t) vs time and 1/(A_0-A_t) vs time are shown in Figure V-15 (C) and (D). Both ln(A_0-A_t) vs time and 1/(A_0-A_t) vs time plots fail to produce a linear correlation which indicates that at higher temperatures, neither a clear first order nor a second order process can be verified in the reaction medium.

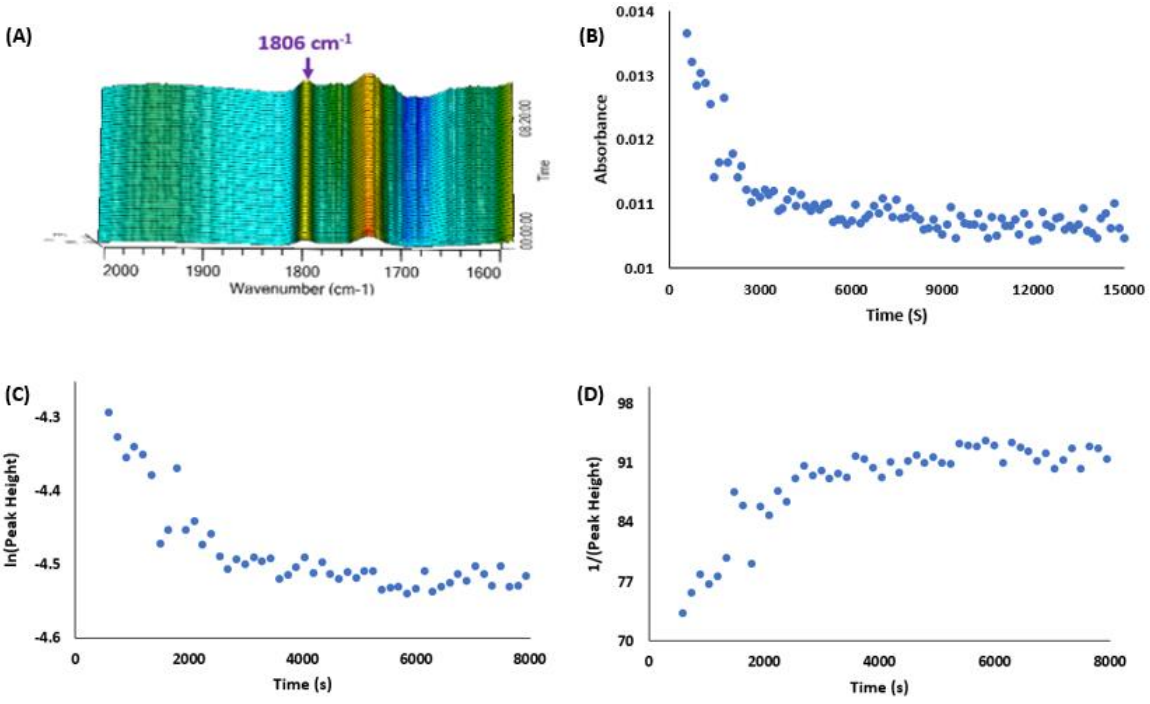

Figure V-15. (A) in-situ IR plot of complex [(^{15}NO)(FeN$_2$S$_2$)][Fe(^{14}NO)$_2$] at 25 ℃ **(B)** plot of band height change vs time for 1806 cm^{-1} band of complex [(^{15}NO)(FeN$_2$S$_2$)][Fe(^{14}NO)$_2$] **(C)** plot of ln(A_0-A_t) vs time for band at 1806 cm^{-1} **(D)** plot of 1/(A_0-A_t) vs time for band at 1806 cm^{-1}

Conclusions and Analysis of change in band heights in in-situ IR

Band height analysis at 5 ℃, 15 ℃ and 25 ℃ indicates that the band at 1806 cm^{-1} does not follow the expected trend of decreasing its intensity by $^{2}/_{3}$. Rather than losing the band height by $^{2}/_{3}$ of its original value, in all temperatures the band height lowers by approximately 25% of its original value (Figure V-16)

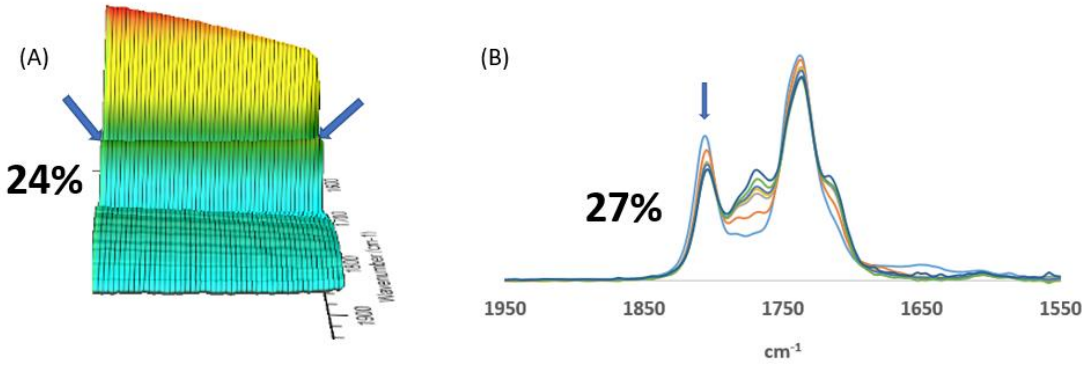

Figure V-16. Band height analysis of complex $[(^{15}NO)(FeN_2S_2)][Fe(^{14}NO)_2]$. (A) Height analysis of 1806 cm^{-1} band in MeCN at 5 ℃ after 12 hours. (B) Height analysis of 1806 cm^{-1} band in MeCN at 25 ℃ after 24 hours.

In order to make the postulate that the height of the 1806 cm^{-1} band will go down $^{2}/_{3}$ of its original value, we assumed a strict intramolecular process at low temperatures. However, based on the experimental evidence it is reasonable to assume that the complex $[(^{15}NO)(FeN_2S_2)][Fe(^{14}NO)_2]$ shows both inter and intramolecular ^{15}NO exchange at all temperatures. The IR spectrum of the complex $[(^{15}NO)(FeN_2S_2)][Fe(^{14}NO)_2]$ with time shows a growth of a broader shoulder band around 1730 cm^{-1} at all temperatures. The all ^{15}NO labeled complex $[(^{15}NO)(FeN_2S_2)][Fe(^{15}NO)_2]$ contains two bands at 1735 cm^{-1} and 1710 cm^{-1} and it is reasonable to assume that the growth of a broad shoulder in 1730 cm^{-1}

region is a result of overlapping 1735 cm^{-1} and 1710 cm^{-1} bands. The clearly observable shoulder band in 1730 cm^{-1} region even at lower temperatures is an indication of generating the all-labeled $[(^{15}NO)(FeN_2S_2)][Fe(^{15}NO)_2]$ complex as a result of intermolecular ^{15}NO exchange process. Careful examination of the in-situ IR plots indicates that the growth of 1730 cm^{-1} broader shoulder band is more prominent at higher temperatures indicating a higher concentration of $[(^{15}NO)(FeN_2S_2)][Fe(^{15}NO)_2]$ complex possibly due to the intermolecular NO exchange process. Furthermore, at 5 ℃ the plot of $\ln(A_0-A_t)$ versus time for a first order process showed a good linearity with R^2 values of 0.9459 which indicates a NO scrambling event with first order kinetics. Hence, at lower temperatures it is reasonable to assume that a first order intramolecular event is more favored compared to a second order intermolecular process. At 15 ℃ both $\ln(A_0-A_t)$ versus time and the $1/(A_0-A_t)$ vs time plots showed poor linearity with R^2 values of 0.7832 and 0.7576 making it difficult to differentiate between a first order and a second order process. However, at 25 ℃ both $\ln(A_0-A_t)$ versus time and the $1/(A_0-A_t)$ vs time plots show a significant deviation from linearity which indicates a complex reaction scheme probably due to a mixture of inter/intra-molecular NO scrambling process.

The mass spectroscopic data at room temperature gives clear evidence about the existence of mono, di and tri ^{15}NO substituted diiron trinitrosyl complexes in the solution of $[(^{15}NO)(FeN_2S_2)][Fe(^{14}NO)_2]$ at 25 ℃. It is reasonable to suspect the existence of a equilibrium between the different mono, di and tri substituted diiron complexes based on the activation energy barriers required for the nitrosyl exchange process. We postulate that such factors may cause unexpected variations in band heights which prompts further studies to fully understand the $[(^{15}NO)(FeN_2S_2)][Fe(^{14}NO)_2]$ system.

CHAPTER VI

CONCLUSIONS AND FUTURE PROSPECTS[#]

The timeline for development and understanding of hydrogenase enzymes covers remarkable progress in the areas of microbiology, molecular biology and synthetic chemistry. Nearly a century ago, before isolation of single cells was common, as well as isolation of enzyme active sites from them, the chemistry of hydrogenases has advanced to the current point where structures of the crystallized giant biomolecules can be interrogated atom by atom in order to guide understanding of structure and function.

The 90 years-old quest for hydrogenase began when Marjory Stephenson and L. H. Stickland discovered Hydrogenase from polluted river Ouse in England. Since their discovery, biochemists have put a significant effort to further understand their mechanism of action. In 1995, Fontecilla -Camps uncovered the crystal structure of [NiFe]-H_2ase and in 1999 Peters *et al.* reported the crystal structure of [FeFe]-H_2ase.[20,22] These findings gave birth to the era of synthetic biomimetics of hydrogenase where prominent chemists like Darensbourg, Rauchfuss, Pickett, Amstrong with the help of others have developed more than 1800 different synthetic mimics of the active sites. Today, researchers like Lubitz, Berggren and many others are continuing the quest to uncover the mysteries of hydrogenase

---

[#]Parts of this chapter were reproduced with permission from (Darensbourg, M. Y.; Oduaran, E. L.; Ding, S.; Lunsford, A. M.; Kariyawasam Pathirana, K. D.; Ghosh, P.; Yang, X., Organometallic Chemistry Control of Hydrogenases. In *Enzymes for Solving Humankind's Problems: Natural and Artificial Systems in Health, Agriculture, Environment and Energy*, Moura, J. J. G.; Moura, I.; Maia, L. B., Eds. Springer International Publishing: Cham, 2021; pp 275-300.)

catalytic mechanisms using advanced biochemical techniques, spectroscopic measurements and computational models of the real systems. During my graduate research years (2016-2021) significant advances were made in understanding the active sites of [FeFe]-H_2ase and [NiFe]-H_2ase via the development of small molecular models from research groups across the world.

Synthetic small molecule models, with a thiolate-bridged homobimetallic core that emulates the features of [FeFe]-H_2ase active site has been a point of interest in Darensbourg group over the last decade. Although, several [FeFe]-H_2ase biomimetics that display certain features have been developed and studied, only a few contained an active pendant base that is capable of shuttling protons to the Fe site. The Rauchfuss group designed a [FeFe]-H_2ase mimic that had installed an azadithiol bridgehead which demonstrated some success acting as a proton shuttle.[26] It has been observed that the synthetic biomimetics of [FeFe]-H_2ase demonstrate significantly lower turnover numbers and turnover frequencies compared to nature's active sites. Part of the problem is the lack of protein scaffolds in synthetic mimics to efficiently transfer protons and electrons to the active site. Although it might not be possible to achieve the remarkable efficiency of nature's enzymes in the absence of such sophisticated evolved scaffold. An open question is "can we develop new methodologies to enhance the catalytic properties of existing [FeFe]-H_2ase biomimetics, such as synthetically installing a much-needed pendant base feature".

The importance of the pendant base feature in active sites was demonstrated by the seminal work done by Lambertz *et al*. and Klein *et al.* where they demonstrated the ability of apo-HydF from *Thermotoga maritima* (*Tm*) to bind three inorganic mimics of the binuclear subsite to its [4Fe-4S] cluster.[34] These studies used different synthetic mimics that

contained a different central atom in the dithiol ligand (carbon (pdt), nitrogen (adt), or oxygen (odt)) (Figure 1). HYSCORE experiments and DFT calculations have indicated that the binuclear mimic is bound through a CN ligand which isomerizes such that its carbon is bound to the [4Fe-4S] cluster instead to the "proximal" iron of the binuclear subsite. However, it was observed that only the synthetic mimics that containing the aza-dithiolate bridgehead is capable of activating to the full potential to conduct HER highlighting the importance of the pendant base feature in [FeFe]-H_2ase.[34]

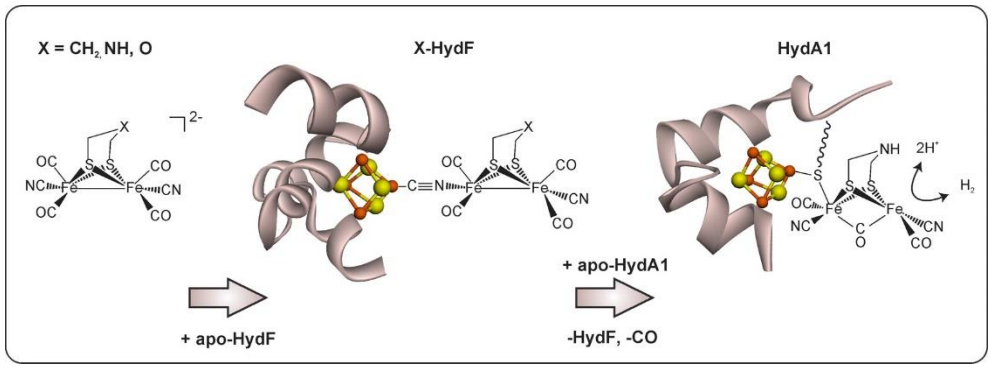

Figure VI-1. Artificial maturation of the H-cluster of the [FeFe]-H_2ase in *Thermotoga maritima* (*Tm*) (Reprinted with permission from (Lubitz, W.; Ogata, H.; Rüdiger, O.; Reijerse, E., *Chem. Rev.* **2014**, 114 (8), 4081-4148). Copyright **2014** American Chemical Society)

The value of "hidden" pendant base was uncovered in a class of complexes that demonstrates hemi-labile features. Here it was convincingly established in a series that the complexes are capable of generating a necessary but temporary pendant base feature followed by a combination of E/C steps depending on their electron buffering capabilities.[135] The mechanisms differ in the position of those electrochemical responses and to the strength of the added acid, according to the availability of the electron buffering NO, the presence of a redox active ligand. As shown in Figure. VI-2, the NiFe and FeFe complexes are characterized as Hard and Soft, an analogy to acid/base designations, however here

Hard/Soft refers to the absence or presence of electron-delocalizing NO ligands either on the metallodithiolate donor ligand or the iron acceptor.[135] For example, the $[Fe(NO)]N_2S_2$ metallodithiolate ligand is classified as a "soft" donor relative to NiN_2S_2, a hard donor reflecting the electron densities on the donor thiolate sulfurs. Similarly the $Fe(NO)_2$ unit is a "soft" acceptor, while the $(\eta^5\text{-}C_5H_5)Fe$ unit is "hard". For the metallodithiolate donors, the reversible one-electron reduction potentials are a numerical approach to quantifying the difference in donors: ca. -2.7 V for the NiN_2S_2 and -1.7 V for the $[Fe(NO)]N_2S_2$ relative to $Fc/Fc^+ = 0.00$ V.[135]

These differences control the position of the first-added electron in the cyclic voltammograms of the NiFe complexes containing the "hard" acceptor as well as the proton/electron level that defines the ultimate coupling process Eventually, the cleavage of the iron-sulfur donor provides landing sites for proton uptake both at sulfur and at iron.[135] The take-home message of Figure. VI-2 is that although there is no obvious pendant base in any of these complexes, the computational analysis that addressed addition of protons and electrons, found reaction pathways that recognized the cleavage of bridging thiolate, exposing an active thiolate's lone pair and increased basicity to offer a reasonable path for H^+/H^- coupling.[135]

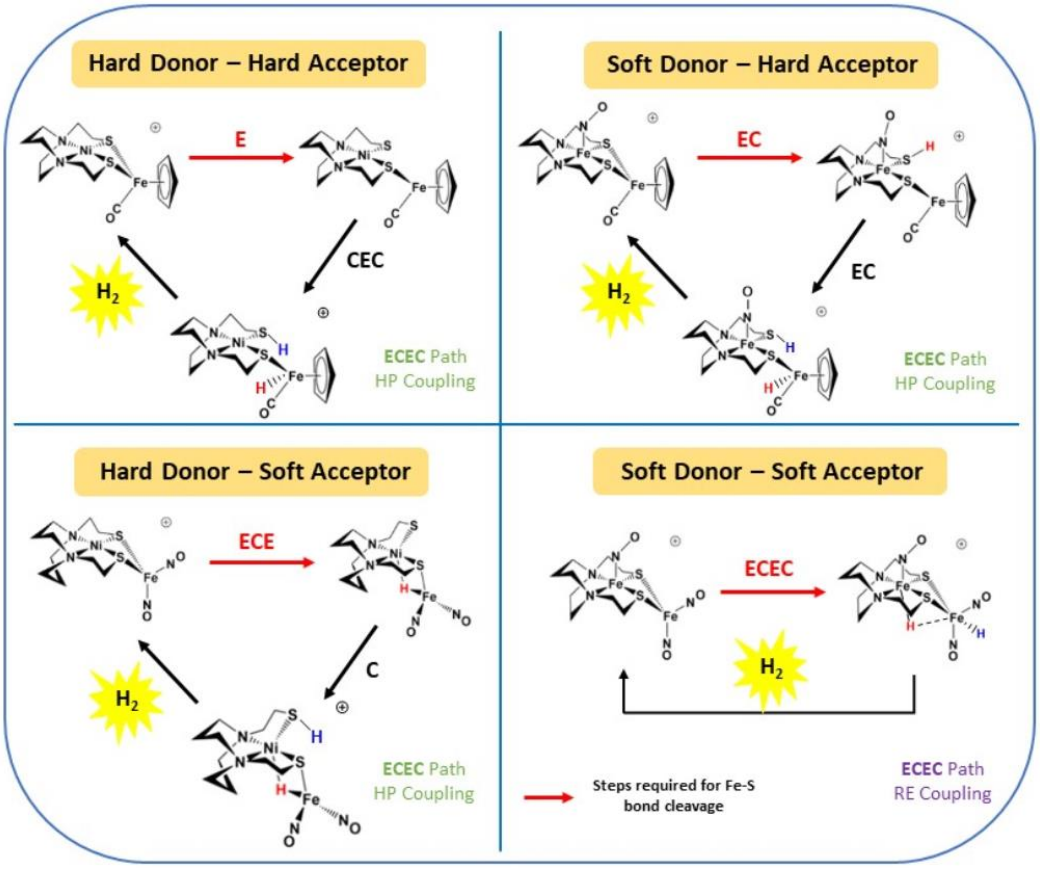

Figure IV-2. Electrocatalytic H_2 evolution from M-MN_2S_2 heterobimetallic complexes that contain hard donor-hard acceptor (top left), soft donor-hard acceptor (top right), hard donor-soft acceptor (bottom left), soft donor-soft acceptor (bottom right) units. †In the case of soft donor-soft acceptor, calculations have shown the possibility of converting the starting material to final intermediate after ECEC steps without cleaving the Fe–S bond. (Reprinted with permission from (Darensbourg, M. Y.; Oduaran, E. L.; Ding, S.; Lunsford, A. M.; Kariyawasam Pathirana, K. D.; Ghosh, P.; Yang, X., Organometallic Chemistry Control of Hydrogenases. In *Enzymes for Solving Humankind's Problems: Natural and Artificial Systems in Health, Agriculture, Environment and Energy*, Moura, J. J. G.; Moura, I.; Maia, L. B., Eds. Springer International Publishing: Cham, 2021; pp 275-300.). Copyright **2021** Springer Nature Switzerland AG)

In chapter III, we discussed the possibility of moving away from the concept of hemilability to temporarily generate a pendant base feature to synthetically insert a NiN_2S_2 metallodithioalto ligand that is capable of binding to a variety of diiron scaffolds in different oxidation states ([Fe^IFe^I], [Fe^IFe^{II}(NO)] and [$Fe^{II}Fe^{II}$]) in a monodentate fashion (Figure VI-

3), leaving the unbound/dangling thiolate to act as a permanent potential pendant basic site to capture protons during hydrogen production.

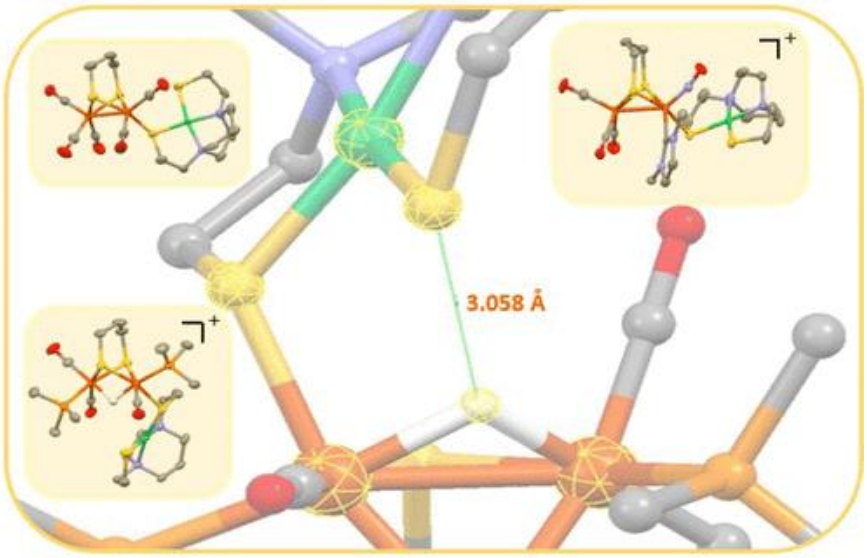

Figure VI-3. [$Fe^{I}Fe^{I}$], [$Fe^{I}Fe(NO)^{II}$] and [$Fe^{II}Fe^{II}$] model complexes that demonstrate monodentate binding of the NiN_2S_2 metallodithiolato ligand. (Reprinted with permission from (Kariyawasam Pathirana, K. D.; Ghosh, P.; Hsieh, C-H.; Elrod, L. C.; Bhuvanesh, N.; Darensbourg, D. J.; Darensbourg, M. Y., *Inorg. Chem*, **2020**, 59 (6), 3753-3763). Copyright **2020** American Chemical Society)

Our studies indicated that model complexes that contain the potential basic pendant site are capable of generating a higher catalytic current with respect to the added acid compared to its counterpart that does not contain the pendant base feature. For complex $Fe^{I}Fe^{I}\cdot NiN_2S_2$ the attribution of the reduction-induced cathodic current enhancement upon addition of TFA to electrocatalytic H_2 production was verified by gas chromatography and quantified by bulk electrolysis experiments performed at −1.61 V for 30 min, in a CH_3CN solution containing 2 mM of catalyst and 50 equiv. of TFA (TOF, 17.5 s^{-1}; TON, 0.22; FE, 78.4%).[90] Essentially, the ability of NiN_2S_2 ligand to act as a stable pendant base feature in a variety of diiron complexes with different oxidation states and ligand environments

indicates an opportunity to modify a variety of existing synthetic biomimetics to further enhance their activity.

When it comes to synthetic mimics of hydrogenases, the research took a new direction when Lichtenberger *et al.* introduced a simple diiron hexacarbonyl mimic into a metallopolymer using a technique called atom transfer radical polymerization, developed by Krzysztof Matyjasezewski (Figure IV-4).[81] These models even with the absence of a dedicated pendant feature to shuttle protons to the active site showed a remarkable efficiency with a turnover frequency of 250000 s^{-1} and turnover numbers on the order of 40000 under both aerobic and anaerobic conditions.[81] Due to the functionalization ability of the polymer, Lichtenberger *et al.* were able to conduct catalysis in an aqueous medium mimicking the activity of hydrogenase in nature to a higher degree.[81] As discussed above, Chapter III of this manuscript demonstrates the potential of a metallodithiolato ligands to bind to a certain metal center using a single thiolate while leaving the other thiolate hanging in order to serve as a dedicated pendant base site to assist in proton hydride coupling. We posit by employing techniques discussed in Chapter III to introduce such missing features to existing systems such as metallopolymers developed by Lichtenberger *et al.*, will further enhance their catalytic capabilities and pave the way to develop more robust and efficient hydrogenase mimics for real life applications.

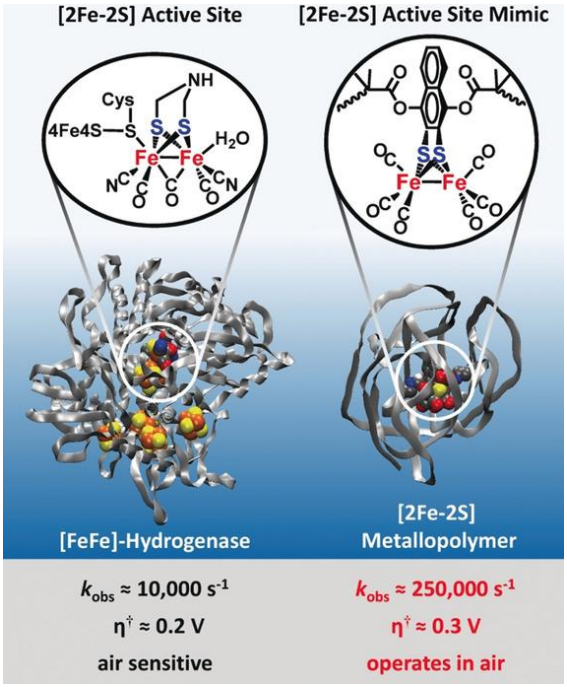

Figure IV-4. Synthetic metallopolymers for HER in aqueous mediums using ATRP technique. (Reprinted with permission from (Brezinski, W. P.; Karayilan, M.; Kayla, C. E.; Pavlopoulos, N.G.; Li, S.; Fu, S.; Matyjaszewski, K.; Evans, D. H.; Glass, R. S.; Lichtenberger, D. L., *Angew. Chem. Int. Ed.* **2018**, 57 (37), 11898-11902). Copyright **2018** John Wiley and Sons)

The kinetics studies in Chapter IV summarize our efforts to estimate the Fe–S bond strength and to investigate different ligand substitution pathways in [FeFe]-H_2ase biomimetics. Based on our studies a simplistic relationship of the qualitative results of NiN_2S_2 ligand displacement is with the expected electrostatic contribution to the Fe–S bonds in the metallodithiolato ligand: $Fe^{I}Fe^{I}$–S_2N_2Ni < $Fe^{I}Fe^{II}$–S_2N_2Ni < < $Fe^{II}Fe^{II}$–S_2N_2Ni. This correlation is assuming positive character of the NO-substituted Fe in $Fe^{I}Fe^{II}$ complex following the addition of NO^+, thus generating the Enemark–Feltham $\{Fe(NO)\}^7$ unit as the NO^+ withdraws sufficient electron density from Fe^{I}, effectively generating $Fe^{II}(NO)^{\bullet}$. In the $Fe^{II}Fe^{II}$ complex a fully oxidized Fe^{II} center is present due to the bridging hydride, thus generating the strongest Fe–S bond. However, the steric encumbrance from the NHC ligand

in complex $Fe^{I}Fe^{II}$ is also a factor as expressed in the longest Fe–S bond distance found, while the all-CO derivative, complex $Fe^{I}Fe^{I}$, generates the shortest distance. The conundrum of steric vs electronic control thus encouraged further study. To the best of our knowledge the Fe–S bond strength of a [FeFe]-H_2ase biomimetic that contains a diiron core and a dangling thiolate has not been reported to this date. Hence, the kinetics studies presented in Chapter IV are a valuable reference point for future chemists who are interested in developing similar systems with pendant base features. One of the most important properties of a catalyst is to be stable in order to be recovered at the end of its catalytic cycle and the stability of a dangling thiolate as a pendant base will entirely depend on the type of the thiolate as well the electronic and geometric features of acceptor unit. Based on the values reported in Chapter IV, chemists will have a preliminary understanding and gauge the Fe–S bond strengths in similar systems which will help to develop of more stable, robust catalysts towards hydrogen production.

The behavior of iron-nitrosyl complexes is still not very well understood. Over the past decade significant research has been published by prominent chemists in academia in attempts to decipher their properties and functions. While there are many reports on the direct or reductive coupling of NO's in adjacent Fe units to generate N_2O, there are not many reports on potential NO scrambling between adjacent Fe centers. Our preliminary studies using FTIR and mass spectrometry indicated the possibility of a duel inter/intra NO scrambling processes in diiron trinitrosyl complexes at room temperature. The kinetic studies at lower and higher temperatures using diiron trinitrosyl complexes with labeled ^{15}NO have provided further evidence that intramolecular NO scrambling within the molecule is more prominent at lower temperatures, while a complex mixture of intermolecular and

intramolecular processes is present at higher temperatures giving rise to a variety of diiron trinitrosyl complexes with different ^{15}NO substituted isotopomers. However, further computational studies are still required to fully understand this process and the mechanism of NO exchange.

The ubiquitous nature of iron nitrosyls in biology has inspired many chemists to further study such systems to understand their specific roles. We believe that the understanding of the intrinsic features of iron nitrosyl systems such as inter/intra-molecular NO scrambling will greatly influence our understanding about the reactivity of such complexes. One great example is the prominent work by Darensbourg *et al.* to uncover the intramolecular apical/basal site exchange of CO ligands in diiron hexacarbonyl molecules. These studies have helped synthetic chemists to understand the transition state structures of such complexes during an associative type ligand substitution reaction. Similarly, we believe that our studies of diiron trinitrosyl complexes will further the understanding of the reactivity of such complexes.

REFERENCES

1. Beinert, H.; Kennedy, M. C.; Stout, C. D., *Chemical Reviews* **1996,** *96* (7), 2335-2374.
2. Stephenson, M.; Stickland, L. H., *Biochem J* **1931,** *25* (1), 205-214.
3. Green, D. E.; Stickland, L. H., *Biochem J* **1934,** *28* (3), 898-900.
4. Stephenson, M.; Stickland, L. H., *Biochem J* **1933,** *27* (5), 1517-1527.
5. Lubitz, W.; Ogata, H.; Rüdiger, O.; Reijerse, E., *Chemical Reviews* **2014,** *114* (8), 4081-4148.
6. Krasna, A. I.; Rittenberg, D., *Journal of the American Chemical Society* **1954,** *76* (11), 3015-3020.
7. Krasna, A. I.; Riklis, E.; Rittenberg, D., *Journal of Biological Chemistry* **1960,** *235* (9), 2717-2720.
8. Haschke, R. H.; Campbell, L. L., *Journal of bacteriology* **1971,** *105* (1), 249-58.
9. Darensbourg, D. J.; Reibenspies, J. H.; Lai, C.-H.; Lee, W.-Z.; Darensbourg, M. Y., *Journal of the American Chemical Society* **1997,** *119* (33), 7903-7904.
10. Lai, C.-H.; Lee, W.-Z.; Miller, M. L.; Reibenspies, J. H.; Darensbourg, D. J.; Darensbourg, M. Y., *Journal of the American Chemical Society* **1998,** *120* (39), 10103-10114.
11. Lyon, E. J.; Georgakaki, I. P.; Reibenspies, J. H.; Darensbourg, M. Y., *Angewandte Chemie International Edition* **1999,** *38* (21), 3178-3180.
12. Smee, J. J.; Goodman, D. C.; Reibenspies, J. H.; Darensbourg, M. Y., *European Journal of Inorganic Chemistry* **1999,** *1999* (3), 539-546.

13. Beinert, H.; Holm, R. H.; Münck, E., Iron-Sulfur Clusters: Nature's Modular, Multipurpose Structures. *Science* **1997,** *277* (5326), 653-659.

14. Yoo, S. J.; Hu, Z.; Goh, C.; Bominaar, E. L.; Holm, R. H.; Münck, E., *Journal of the American Chemical Society* **1997,** *119* (37), 8732-8733.

15. Holm, R. H.; Lo, W., Structural Conversions of Synthetic and Protein-Bound Iron–Sulfur Clusters. *Chemical Reviews* **2016,** *116* (22), 13685-13713.

16. Albracht, S. P. J.; Graf, E.-G.; Thauer, R. K., The EPR properties of nickel in hydrogenase from Methanobacterium thermoautotrophicum. *FEBS Letters* **1982,** *140* (2), 311-313.

17. Graf, E.-G.; Thauer, R. K., *FEBS Letters* **1981,** *136* (1), 165-169.

18. LeGall, J.; Ljungdahl, P. O.; Moura, I.; Peck, H. D., Jr.; Xavier, A. V.; Moura, J. J.; Teixera, M.; Huynh, B. H.; DerVartanian, D. V., *Biochemical and biophysical research communications* **1982,** *106* (2), 610-6.

19. Fontecilla-Camps, J. C.; Volbeda, A.; Cavazza, C.; Nicolet, Y., *Chem Rev* **2007,** *107* (10), 4273-303.

20. Nicolet, Y.; Piras, C.; Legrand, P.; Hatchikian, C. E.; Fontecilla-Camps, J. C., *Structure (London, England : 1993)* **1999,** *7* (1), 13-23.

21. Bagley, K. A.; Duin, E. C.; Roseboom, W.; Albracht, S. P.; Woodruff, W. H., *Biochemistry* **1995,** *34* (16), 5527-35.

22. Peters, J. W.; Lanzilotta, W. N.; Lemon, B. J.; Seefeldt, L. C., *Science* **1998,** *282* (5395), 1853-8.

23. Teske, A., In *Algae and Cyanobacteria in Extreme Environments*, Seckbach, J., Ed. Springer Netherlands: Dordrecht, 2007; pp 519-533.

24. Ma, K.; Schicho, R. N.; Kelly, R. M.; Adams, M. W., *Proceedings of the National Academy of Sciences* **1993,** *90* (11), 5341-5344.

25. Suarez, P. A. Z.; Dullius, J. E. L.; Einloft, S.; De Souza, R. F.; Dupont, J., *Polyhedron* **1996,** *15* (7), 1217-1219.

26. Happe, R. P.; Roseboom, W.; Pierik, A. J.; Albracht, S. P. J.; Bagley, K. A., *Nature* **1997,** *385* (6612), 126-126.

27. Pierik, A. J.; Hulstein, M.; Hagen, W. R.; Albracht, S. P. J., *European Journal of Biochemistry* **1998,** *258* (2), 572-578.

28. Volbeda, A.; Garcin, E.; Piras, C.; de Lacey, A. L.; Fernandez, V. M.; Hatchikian, E. C.; Frey, M.; Fontecilla-Camps, J. C., *Journal of the American Chemical Society* **1996,** *118* (51), 12989-12996.

29. Nicolet, Y.; Lemon, B. J.; Fontecilla-Camps, J. C.; Peters, J. W., *Trends in biochemical sciences* **2000,** *25* (3), 138-43.

30. Darensbourg, M. Y.; Lyon, E. J.; Zhao, X.; Georgakaki, I. P., *Proceedings of the National Academy of Sciences* **2003,** *100* (7), 3683-3688.

31. Dole, F.; Fournel, A.; Magro, V.; Hatchikian, E. C.; Bertrand, P.; Guigliarelli, B., *Biochemistry* **1997,** *36* (25), 7847-7854.

32. Carroll, M. E.; Barton, B. E.; Rauchfuss, T. B.; Carroll, P. J., *Journal of the American Chemical Society* **2012,** *134* (45), 18843-18852.

33. Adamska, A.; Silakov, A.; Lambertz, C.; Rüdiger, O.; Happe, T.; Reijerse, E.; Lubitz, W., *Angewandte Chemie International Edition* **2012,** *51* (46), 11458-11462.

34. Lubitz, W.; Reijerse, E.; van Gastel, M., *Chemical Reviews* **2007,** *107* (10), 4331-4365.

35. Czech, I.; Silakov, A.; Lubitz, W.; Happe, T., *FEBS Letters* **2010,** *584* (3), 638-642.

36. Silakov, A.; Olsen, M. T.; Sproules, S.; Reijerse, E. J.; Rauchfuss, T. B.; Lubitz, W., *Inorganic Chemistry* **2012,** *51* (15), 8617-8628.

37. Hsieh, C.-H.; Erdem, Ö. F.; Harman, S. D.; Singleton, M. L.; Reijerse, E.; Lubitz, W.; Popescu, C. V.; Reibenspies, J. H.; Brothers, S. M.; Hall, M. B.; Darensbourg, M. Y., *Journal of the American Chemical Society* **2012,** *134* (31), 13089-13102.

38. Yahata, N.; Saitoh, T.; Takayama, Y.; Ozawa, K.; Ogata, H.; Higuchi, Y.; Akutsu, H., *Biochemistry* **2006,** *45* (6), 1653-1662.

39. Matias, P. M.; Soares, C. M.; Saraiva, L. M.; Coelho, R.; Morais, J.; Le Gall, J.; Carrondo, M. A., *JBIC Journal of Biological Inorganic Chemistry* **2001,** *6* (1), 63-81.

40. Fritsch, J.; Scheerer, P.; Frielingsdorf, S.; Kroschinsky, S.; Friedrich, B.; Lenz, O.; Spahn, C. M. T., *Nature* **2011,** *479* (7372), 249-252.

41. Shomura, Y.; Yoon, K.-S.; Nishihara, H.; Higuchi, Y., *Nature* **2011,** *479* (7372), 253-256.

42. Fontecilla-Camps, J. C.; Amara, P.; Cavazza, C.; Nicolet, Y.; Volbeda, A., *Nature* **2009,** *460* (7257), 814-822.

43. Silakov, A.; Wenk, B.; Reijerse, E.; Lubitz, W., *Physical Chemistry Chemical Physics* **2009,** *11* (31), 6592-6599.

44. Das, P.; Capon, J.-F.; Gloaguen, F.; Pétillon, F. Y.; Schollhammer, P.; Talarmin, J.; Muir, K. W., *Inorganic Chemistry* **2004,** *43* (26), 8203-8205.

45. Sommer, C.; Adamska-Venkatesh, A.; Pawlak, K.; Birrell, J. A.; Rüdiger, O.; Reijerse, E. J.; Lubitz, W., *Journal of the American Chemical Society* **2017,** *139* (4), 1440-1443.

46. del Barrio, M.; Sensi, M.; Fradale, L.; Bruschi, M.; Greco, C.; de Gioia, L.; Bertini, L.; Fourmond, V.; Léger, C., *Journal of the American Chemical Society* **2018,** *140* (16), 5485-5492.

47. Reijerse, E.; Birrell, J. A.; Lubitz, W., *The Journal of Physical Chemistry Letters* **2020,** *11* (12), 4597-4602.

48. Curtis, C. J.; Miedaner, A.; Ciancanelli, R.; Ellis, W. W.; Noll, B. C.; Rakowski DuBois, M.; DuBois, D. L., *Inorganic Chemistry* **2003,** *42* (1), 216-227.

49. Henry, R. M.; Shoemaker, R. K.; DuBois, D. L.; DuBois, M. R., *Journal of the American Chemical Society* **2006,** *128* (9), 3002-3010.

50. Henry, R. M.; Shoemaker, R. K.; Newell, R. H.; Jacobsen, G. M.; DuBois, D. L.; Rakowski DuBois, M., *Organometallics* **2005,** *24* (10), 2481-2491.

51. Wilson, A. D.; Newell, R. H.; McNevin, M. J.; Muckerman, J. T.; Rakowski DuBois, M.; DuBois, D. L., *Journal of the American Chemical Society* **2006,** *128* (1), 358-366.

52. Nicolet, Y.; de Lacey, A. L.; Vernède, X.; Fernandez, V. M.; Hatchikian, E. C.; Fontecilla-Camps, J. C., *Journal of the American Chemical Society* **2001,** *123* (8), 1596-1601.

53. Roseboom, W.; De Lacey, A. L.; Fernandez, V. M.; Hatchikian, E. C.; Albracht, S. P. J., *JBIC Journal of Biological Inorganic Chemistry* **2006,** *11* (1), 102-118.

54. Silakov, A.; Kamp, C.; Reijerse, E.; Happe, T.; Lubitz, W., *Biochemistry* **2009,** *48* (33), 7780-7786.

55. Wright, J. A.; Webster, L.; Jablonskytė, A.; Woi, P. M.; Ibrahim, S. K.; Pickett, C. J., *Faraday Discussions* **2011,** *148* (0), 359-371.

56. Jablonskytė, A.; Wright, J. A.; Pickett, C. J., *Dalton Transactions* **2010,** *39* (12), 3026-3034.

57. Wright, J. A.; Pickett, C. J., *Chemical Communications* **2009,** (38), 5719-5721.

58. Cornish, A. J.; Gärtner, K.; Yang, H.; Peters, J. W.; Hegg, E. L., *Journal of Biological Chemistry* **2011,** *286* (44), 38341-38347.

59. Mulder, David W.; Shepard, Eric M.; Meuser, Jonathan E.; Joshi, N.; King, Paul W.; Posewitz, Matthew C.; Broderick, Joan B.; Peters, John W., *Structure (London, England : 1993)* **2011,** *19* (8), 1038-1052.

60. Mulder, D. W.; Ratzloff, M. W.; Shepard, E. M.; Byer, A. S.; Noone, S. M.; Peters, J. W.; Broderick, J. B.; King, P. W., *Journal of the American Chemical Society* **2013,** *135* (18), 6921-6929.

61. Peters, J. W.; Schut, G. J.; Boyd, E. S.; Mulder, D. W.; Shepard, E. M.; Broderick, J. B.; King, P. W.; Adams, M. W. W., *Biochimica et Biophysica Acta (BBA) - Molecular Cell Research* **2015,** *1853* (6), 1350-1369.

62. Land, H.; Senger, M.; Berggren, G.; Stripp, S. T., *ACS Catalysis* **2020,** *10* (13), 7069-7086.

63. Tard, C.; Pickett, C. J., *Chemical Reviews* **2009,** *109* (6), 2245-2274.

64. Tschierlei, S.; Ott, S.; Lomoth, R., *Energy & Environmental Science* **2011,** *4* (7), 2340-2352.

65. Felton, G. A. N.; Mebi, C. A.; Petro, B. J.; Vannucci, A. K.; Evans, D. H.; Glass, R. S.; Lichtenberger, D. L., *Journal of Organometallic Chemistry* **2009,** *694* (17), 2681-2699.

66. Charreteur, K.; Kdider, M.; Capon, J.-F.; Gloaguen, F.; Pétillon, F. Y.; Schollhammer, P.; Talarmin, J., *Inorganic Chemistry* **2010,** *49* (5), 2496-2501.

67. Eilers, G.; Schwartz, L.; Stein, M.; Zampella, G.; de Gioia, L.; Ott, S.; Lomoth, R., *Chemistry – A European Journal* **2007,** *13* (25), 7075-7084.

68. Reihlen, H.; Gruhl, A.; v. Hessling, G., *Justus Liebigs Annalen der Chemie* **1929,** *472* (1), 268-287.

69. Hagen, W. R.; van Berkel-Arts, A.; Krüse-Wolters, K. M.; Dunham, W. R.; Veeger, C., *FEBS Letters* **1986,** *201* (1), 158-162.

70. Song, L.-C.; Yang, Z.-Y.; Bian, H.-Z.; Liu, Y.; Wang, H.-T.; Liu, X.-F.; Hu, Q.-M., *Organometallics* **2005,** *24* (25), 6126-6135.

71. Song, L.-C.; Yang, Z.-Y.; Hua, Y.-J.; Wang, H.-T.; Liu, Y.; Hu, Q.-M., *Organometallics* **2007,** *26* (8), 2106-2110.

72. Li, H.; Rauchfuss, T. B., *Journal of the American Chemical Society* **2002,** *124* (5), 726-727.

73. Wang, Z.; Liu, J.-H.; He, C.-J.; Jiang, S.; Åkermark, B.; Sun, L.-C., *Journal of Organometallic Chemistry* **2007,** *692* (24), 5501-5507.

74. Windhager, J.; Rudolph, M.; Bräutigam, S.; Görls, H.; Weigand, W., *European Journal of Inorganic Chemistry* **2007,** *2007* (18), 2748-2760.

75. Windhager, J.; Görls, H.; Petzold, H.; Mloston, G.; Linti, G.; Weigand, W., *European Journal of Inorganic Chemistry* **2007,** *2007* (28), 4462-4471.

76. Harb, M. K.; Niksch, T.; Windhager, J.; Görls, H.; Holze, R.; Lockett, L. T.; Okumura, N.; Evans, D. H.; Glass, R. S.; Lichtenberger, D. L.; El-khateeb, M.; Weigand, W., *Organometallics* **2009,** *28* (4), 1039-1048.

77. Hieber, W.; Spacu, P., *Zeitschrift für anorganische und allgemeine Chemie* **1937,** *233* (4), 353-364.

78. Camara, J. M.; Rauchfuss, T. B., *Nature Chemistry* **2012,** *4* (1), 26-30.

79. Li, C.-B.; Li, Z.-J.; Yu, S.; Wang, G.-X.; Wang, F.; Meng, Q.-Y.; Chen, B.; Feng, K.; Tung, C.-H.; Wu, L.-Z., *Energy & Environmental Science* **2013,** *6* (9), 2597-2602.

80. Pullen, S.; Fei, H.; Orthaber, A.; Cohen, S. M.; Ott, S., *Journal of the American Chemical Society* **2013,** *135* (45), 16997-17003.

81. Brezinski, W. P.; Karayilan, M.; Clary, K. E.; Pavlopoulos, N. G.; Li, S.; Fu, L.; Matyjaszewski, K.; Evans, D. H.; Glass, R. S.; Lichtenberger, D. L.; Pyun, J., *Angewandte Chemie International Edition* **2018,** *57* (37), 11898-11902.

82. Brezinski, W. P.; Karayilan, M.; Clary, K. E.; McCleary-Petersen, K. C.; Fu, L.; Matyjaszewski, K.; Evans, D. H.; Lichtenberger, D. L.; Glass, R. S.; Pyun, J., *ACS Macro Letters* **2018,** *7* (11), 1383-1387.

83. Glass, R. S.; Pyun, J.; Lichtenberger, D. L.; Brezinski, W. P.; Karayilan, M.; Clary, K. E.; Pavlopoulos, N. G.; Evans, D. H., *Phosphorus, Sulfur, and Silicon and the Related Elements* **2019,** *194* (7), 701-706.

84. Karayilan, M.; Brezinski, W. P.; Clary, K. E.; Lichtenberger, D. L.; Glass, R. S.; Pyun, J., *Angewandte Chemie International Edition* **2019,** *58* (23), 7537-7550.

85. Karayilan, M.; McCleary-Petersen, K. C.; Hamilton, M. O. B.; Fu, L.; Matyjaszewski, K.; Glass, R. S.; Lichtenberger, D. L.; Pyun, J., *Macromolecular Rapid Communications* **2020,** *41* (1), 1900424.

86. Schilter, D.; Camara, J. M.; Huynh, M. T.; Hammes-Schiffer, S.; Rauchfuss, T. B., *Chemical Reviews* **2016,** *116* (15), 8693-8749.

87. Li, B.; Liu, T.; Singleton, M. L.; Darensbourg, M. Y., *Inorganic Chemistry* **2009,** *48* (17), 8393-8403.

88. Georgakaki, I. P.; Thomson, L. M.; Lyon, E. J.; Hall, M. B.; Darensbourg, M. Y., *Coordination Chemistry Reviews* **2003,** *238-239*, 255-266.

89. Yu, X.; Pang, M.; Zhang, S.; Hu, X.; Tung, C.-H.; Wang, W., *Journal of the American Chemical Society* **2018,** *140* (36), 11454-11463.

90. Kariyawasam Pathirana, K. D.; Ghosh, P.; Hsieh, C.-H.; Elrod, L. C.; Bhuvanesh, N.; Darensbourg, D. J.; Darensbourg, M. Y., *Inorganic Chemistry* **2020,** *59* (6), 3753-3763.

91. Ragsdale, S. W.; Kumar, M., *Chemical Reviews* **1996,** *96* (7), 2515-2540.

92. Denny, J. A.; Darensbourg, M. Y., *Chemical Reviews* **2015,** *115* (11), 5248-5273.

93. Ogo, S.; Ichikawa, K.; Kishima, T.; Matsumoto, T.; Nakai, H.; Kusaka, K.; Ohhara, T., *Science* **2013,** *339* (6120), 682-684.

94. Ghosh, P.; Ding, S.; Chupik, R. B.; Quiroz, M.; Hsieh, C.-H.; Bhuvanesh, N.; Hall, M. B.; Darensbourg, M. Y., *Chemical Science* **2017,** *8* (12), 8291-8300.

95. Ding, S.; Ghosh, P.; Darensbourg, M. Y.; Hall, M. B., *Proceedings of the National Academy of Sciences* **2017,** *114* (46), E9775-E9782.

96. Ding, S.; Ghosh, P.; Lunsford, A. M.; Wang, N.; Bhuvanesh, N.; Hall, M. B.; Darensbourg, M. Y., *Journal of the American Chemical Society* **2016,** *138* (39), 12920-12927.

97. Ghosh, P.; Quiroz, M.; Wang, N.; Bhuvanesh, N.; Darensbourg, M. Y., *Dalton Transactions* **2017,** *46* (17), 5617-5624.

98. Jeffrey, J. C.; Rauchfuss, T. B., *Inorganic Chemistry* **1979,** *18* (10), 2658-2666.

99. Dong, H. T.; Speelman, A. L.; Kozemchak, C. E.; Sil, D.; Krebs, C.; Lehnert, N., *Angewandte Chemie International Edition* **2019,** *58* (49), 17695-17699.

100. Fourmond, V.; Jacques, P.-A.; Fontecave, M.; Artero, V., *Inorganic Chemistry* **2010,** *49* (22), 10338-10347.

101. Felton, G. A. N.; Glass, R. S.; Lichtenberger, D. L.; Evans, D. H., *Inorganic Chemistry* **2006,** *45* (23), 9181-9184.

102. Appel, A. M.; Helm, M. L., *ACS Catalysis* **2014,** *4* (2), 630-633.

103. Wiese, S.; Kilgore, U. J.; Ho, M.-H.; Raugei, S.; DuBois, D. L.; Bullock, R. M.; Helm, M. L., *ACS Catalysis* **2013,** *3* (11), 2527-2535.

104. Darensbourg, M. Y., *Comments on Inorganic Chemistry* **2010,** *31* (3-4), 144-152.

105. Liu, T.; Darensbourg, M. Y., *Journal of the American Chemical Society* **2007,** *129* (22), 7008-7009.

106. Li, Y.; Rauchfuss, T. B., *Chemical Reviews* **2016,** *116* (12), 7043-7077.

107. Volbeda, A.; Charon, M.-H.; Piras, C.; Hatchikian, E. C.; Frey, M.; Fontecilla-Camps, J. C., *Nature* **1995,** *373* (6515), 580-587.

108. Chiang, C.-Y.; Miller, M. L.; Reibenspies, J. H.; Darensbourg, M. Y., *Journal of the American Chemical Society* **2004,** *126* (35), 10867-10874.

109. Rao, P. V.; Bhaduri, S.; Jiang, J.; Holm, R. H., *Inorganic Chemistry* **2004,** *43* (19), 5833-5849.

110. Brazzolotto, D.; Gennari, M.; Queyriaux, N.; Simmons, T. R.; Pécaut, J.; Demeshko, S.; Meyer, F.; Orio, M.; Artero, V.; Duboc, C., *Nature Chemistry* **2016,** *8* (11), 1054-1060.

111. Brazzolotto, D.; Wang, L.; Tang, H.; Gennari, M.; Queyriaux, N.; Philouze, C.; Demeshko, S.; Meyer, F.; Orio, M.; Artero, V.; Hall, M. B.; Duboc, C., *ACS Catalysis* **2018,** *8* (11), 10658-10667.

112. Nguyen, N. T.; Mori, Y.; Matsumoto, T.; Yatabe, T.; Kabe, R.; Nakai, H.; Yoon, K.-S.; Ogo, S., *Chemical Communications* **2014,** *50* (87), 13385-13387.

113. Lyon, E. J.; Georgakaki, I. P.; Reibenspies, J. H.; Darensbourg, M. Y., *Journal of the American Chemical Society* **2001,** *123* (14), 3268-3278.

114. Zhao, X.; Georgakaki, I. P.; Miller, M. L.; Mejia-Rodriguez, R.; Chiang, C.-Y.; Darensbourg, M. Y., *Inorganic Chemistry* **2002,** *41* (15), 3917-3928.

115. Bethel, R. D.; Crouthers, D. J.; Hsieh, C.-H.; Denny, J. A.; Hall, M. B.; Darensbourg, M. Y., *Inorganic Chemistry* **2015,** *54* (7), 3523-3535.

116. Rampersad, M. V.; Jeffery, S. P.; Golden, M. L.; Lee, J.; Reibenspies, J. H.; Darensbourg, D. J.; Darensbourg, M. Y., *Journal of the American Chemical Society* **2005,** *127* (49), 17323-17334.

117. Rampersad, M. V.; Jeffery, S. P.; Reibenspies, J. H.; Ortiz, C. G.; Darensbourg, D. J.; Darensbourg, M. Y., *Angewandte Chemie International Edition* **2005,** *44* (8), 1217-1220.

118. Li, P.; Wang, M.; He, C.; Liu, X.; Jin, K.; Sun, L., *European Journal of Inorganic Chemistry* **2007,** *2007* (23), 3718-3727.

119. Chong, D.; Georgakaki, I. P.; Mejia-Rodriguez, R.; Sanabria-Chinchilla, J.; Soriaga, M. P.; Darensbourg, M. Y., *Dalton Transactions* **2003,** (21), 4158-4163.

120. Zhao, T.; Ghosh, P.; Martinez, Z.; Liu, X.; Meng, X.; Darensbourg, M. Y., *Organometallics* **2017,** *36* (9), 1822-1827.

121. Trautwein, R.; Almazahreh, L. R.; Görls, H.; Weigand, W., *Dalton Transactions* **2015,** *44* (43), 18780-18794.

122. Singleton, M. L.; Jenkins, R. M.; Klemashevich, C. L.; Darensbourg, M. Y., *Comptes Rendus Chimie* **2008,** *11* (8), 861-874.

123. Hsieh, C.-H.; Ding, S.; Erdem, Ö. F.; Crouthers, D. J.; Liu, T.; McCrory, C. C. L.; Lubitz, W.; Popescu, C. V.; Reibenspies, J. H.; Hall, M. B.; Darensbourg, M. Y., *Nature Communications* **2014,** *5* (1), 3684.

124. Ghosh, P.; Ding, S.; Quiroz, M.; Bhuvanesh, N.; Hsieh, C.-H.; Palacios, P. M.; Pierce, B. S.; Darensbourg, M. Y.; Hall, M. B., *Chemistry – A European Journal* **2018,** *24* (60), 16003-16008.

125. Caranto, J. D.; Weitz, A.; Hendrich, M. P.; Kurtz, D. M., *Journal of the American Chemical Society* **2014,** *136* (22), 7981-7992.

126. Jana, M.; White, C. J.; Pal, N.; Demeshko, S.; Cordes, C.; Meyer, F.; Lehnert, N.; Majumdar, A., *Journal of the American Chemical Society* **2020,** *142* (14), 6600-6616.

127. Dong, H. T.; White, C. J.; Zhang, B.; Krebs, C.; Lehnert, N., *Journal of the American Chemical Society* **2018,** *140* (41), 13429-13440.

128. Sarti, P.; Fiori, P. L.; Forte, E.; Rappelli, P.; Teixeira, M.; Mastronicola, D.; Sanciu, G.; Giuffré, A.; Brunori, M., *Cellular and Molecular Life Sciences CMLS* **2004,** *61* (5), 618-623.

129. Missall, T. A.; Lodge, J. K.; McEwen, J. E., *Eukaryotic Cell* **2004,** *3* (4), 835-846.

130. Hayashi, T.; Caranto, J. D.; Matsumura, H.; Kurtz, D. M.; Moënne-Loccoz, P., *Journal of the American Chemical Society* **2012,** *134* (15), 6878-6884.

131. Caranto, J. D.; Weitz, A.; Giri, N.; Hendrich, M. P.; Kurtz, D. M., *Biochemistry* **2014,** *53* (35), 5631-5637.

132. Gardner, A. M.; Gessner, C. R.; Gardner, P. R., *Journal of Biological Chemistry* **2003,** *278* (12), 10081-10086.

133. Rodrigues, R.; Vicente, J. B.; Félix, R.; Oliveira, S.; Teixeira, M.; Rodrigues-Pousada, C., *Journal of bacteriology* **2006,** *188* (8), 2745-2751.

134. Hayashi, T.; Caranto, J. D.; Wampler, D. A.; Kurtz, D. M.; Moënne-Loccoz, P., *Biochemistry* **2010,** *49* (33), 7040-7049.

135. Darensbourg, M. Y.; Oduaran, E. L.; Ding, S.; Lunsford, A. M.; Kariyawasam Pathirana, K. D.; Ghosh, P.; Yang, X.; Moura, J. J. G.; Moura, I.; Maia, L. B., Eds. Springer International Publishing: Cham, 2021; pp 275-300.